MODELING TRANSIENT FLOW IN FRACTURED SHALE RESERVOIRS

A THESIS SUBMITTED TO
THE GRADUATE SCHOOL OF NATURAL AND APPLIED SCIENCES
OF
MIDDLE EAST TECHNICAL UNIVERSITY

BY

UFUK KILIÇASLAN

IN PARTIAL FULFILLMENT OF THE REQUIREMENTS
FOR
THE DEGREE OF DOCTOR OF PHILOSOPHY
IN
PETROLEUM AND NATURAL GAS ENGINEERING

JULY 2021

Approval of the thesis:

MODELING TRANSIENT FLOW IN FRACTURED SHALE RESERVOIRS

submitted by **UFUK KILIÇASLAN** in partial fulfillment of the requirements for the degree of **Doctor of Philosophy in Petroleum and Natural Gas Engineering, Middle East Technical University** by,

Prof. Dr. Halil Kalıpçılar
Dean, Graduate School of **Natural and Applied Sciences** _____

Assoc. Prof. Dr. Çağlar Sınayuç
Head of the Department, **Petroleum and Natural Gas Eng.** _____

Prof. Dr. Serhat Akın
Supervisor, **Petroleum and Natural Gas Eng., METU** _____

Examining Committee Members:

Prof. Dr. İsmail Ömer Yılmaz
Geological Eng., METU _____

Prof. Dr. Serhat Akın
Petroleum and Natural Gas Eng., METU _____

Assist. Prof. Dr. İsmail Durgut
Petroleum and Natural Gas Eng., METU _____

Prof. Dr. Ömer İnanç Türeyen
Petroleum and Natural Gas Eng., ITU _____

Assoc. Prof. Dr. Emre Artun
Petroleum and Natural Gas Eng., ITU _____

Date: 30.07.2021

I hereby declare that all information in this document has been obtained and presented in accordance with academic rules and ethical conduct. I also declare that, as required by these rules and conduct, I have fully cited and referenced all material and results that are not original to this work.

Name Last name : Ufuk Kılıçaslan

Signature :

ABSTRACT

MODELING TRANSIENT FLOW IN FRACTURED SHALE RESERVOIRS

Kılıçaslan, Ufuk
Doctor of Philosophy, Petroleum and Natural Gas Engineering
Supervisor: Prof. Dr. Serhat Akın

July 2021, 137 pages

Oil and gas production from shale reservoirs has been popular in North America for more than two decades. Commercial production from these extremely low permeability reservoirs is only achieved by multi-stage fractured horizontal wells. However, production performance of these wells is quite different than wells drilled in conventional reservoirs. Main distinct behavior seen in these wells is very long period of transient flow due to tightness of such reservoirs.

This thesis questions validity of existing dual-porosity reservoir simulation technique for fractured shale reservoirs. In this respect, analytical solutions of pressure diffusion are presented for constant fracture pressure, constant rate and constant fracture pressure followed by linearly declining fracture pressure boundary conditions. According to these solutions, time-dependent shape factors are derived for 3D rectangular anisotropic matrix. Obtained shape factors and proposed simplifications are verified against fine scale single-porosity numerical models. Key finding from this study is that matrix – fracture transfer function (shape factor) is not constant, but rather decreases with time until reaching to a constant value. Therefore, dual-porosity simulation of fractured shale reservoirs using constant shape factor does not capture actual physics of matrix to fracture flow and yields inaccurate

performance prediction. Also, proposed simplifications either as an empirical function or reduced form are robust in modeling this phenomenon.

In addition to those, common features of decline curve analysis are tested for fractured shale reservoirs. Time dependency of ***b***-parameter used in hyperbolic decline curve analysis is assessed for different reservoir properties by sensitivity analysis. Proposed empirical functions are used to obtain ***b***-parameter for these cases and results are compared with actual ones.

Keywords: Matrix – fracture transfer function, Shape factor, Shale reservoirs, Unsteady-state flow, Dual-porosity reservoir simulation

ÖZ

ÇATLAKLI ŞEYL REZERVUARLARINDA KARARSIZ AKIŞ MODELLEMESİ

Kılıçaslan, Ufuk
Doktora, Petrol ve Doğal gaz Mühendisliği
Tez Yöneticisi: Prof. Dr. Serhat Akın

Temmuz 2021, 137 sayfa

Kuzey Amerika'da yaklaşık 20 yılı aşkın süredir, şeyl rezervuarlarından petrol ve gaz üretimi popüler durumdadır. Düşük geçirgenliğe sahip bu rezervuarlardan ticari üretim yapmak ancak çok kademeli çatlatılmış yatay kuyular ile başarılmaktadır. Fakat, bu kuyuların üretim performansları konvansiyonel rezervuarlarda kazılan kuyulardan oldukça farklıdır. Bu kuyularda görülen en temel farklı davranış kesifliğe bağlı çok uzun süren kararsız akış dönemidir.

Bu tez mevcut çift-gözenekli rezervuar simülasyon tekniğinin çatlaklı şeyl rezervuarları için geçerliliğini sorgulamaktadır. Bu kapsamda, sabit çatlak basıncı, sabit debi ve sabit çatlak basıncı ardından doğrusal olarak çatlak basıncının azalması sınır koşullarında basınç difüzyonunun analitik çözümleri sunulmuştur. Bu çözümlere göre, üç-boyutlu anizotropik matriks için zamana bağlı şekil faktörleri türetilmiştir. Elde edilen şekil faktörleri ve önerilen basitleştirmeler ince ölçek tek-gözenekli nümerik modellerle doğrulanmıştır. Matriks-çatlak transfer fonksiyonunun (şekil faktörünün) sabit olmaktan ziyade sabit bir değere ulaşıncaya kadar zamana bağlı azaldığı bu çalışmadan elde edilen asli bulgudur. Dolayısıyla, çatlaklı şeyl rezervuarlarının sabit şekil faktörü kullanılarak yapılan çift-gözenekli

simülasyonu matriksten çatlağa olan akışın gerçek fiziğini yakalayamaz ve doğru olmayan performans tahmini ortaya çıkarır. Ayrıca, yapay fonksiyon veya indirgenmiş şekil olarak önerilen basitleştirmeler bu davranışın modellenmesinde güçlüdür.

Bunlara ek olarak, düşüm eğrisi analizinin temel özellikleri çatlaklı şeyl rezervuarları için test edilmiştir. Hiperbolik düşüm eğrisinde kullanılan "***b***" parametresinin zamana bağlılığı duyarlılık analizi ile farklı rezervuar özellikleri için belirlenmiştir. Önerilen yapay fonksiyonlar kullanılarak bu senaryolar için "***b***" parametresi elde edilmiştir ve sonuçlar gerçek değerleriyle kıyaslanmıştır.

Anahtar Kelimeler: Matriks-çatlak transfer fonksiyonu, Şekil faktörü, Şeyl rezervuarları, Kararsız akış, Çift-gözenekli rezervuar simülasyonu

To my lovely grandmother who passed away this year

To my son Ozan

ACKNOWLEDGMENTS

First of all, I would sincerely like to thank my supervisor Prof. Dr. Serhat Akın for his endless guidance, advice, criticism, encouragements and insight throughout the research. He shared his expertise at each level of this work and targeted best outcomes from the beginning.

I would also like to thank Assist. Prof. Dr. İsmail Durgut and Prof. Dr. İsmail Ömer Yılmaz, who served as my PhD committee members, for their valuable comments and suggestions. Many thanks to my colleagues at Turkish Petroleum Corporation-Production Department and close friends for their support.

Finally, I would like to express my deepest gratitude to my wife Aylin. She never complained about spent time during this study that I could share with her. Her love and encouragement throughout my life are invaluable. Also, I appreciate to my father Uğur, my mother Ayşe and my sister Dila for their love, trust and support.

TABLE OF CONTENTS

ABSTRACT v

ÖZ vii

ACKNOWLEDGMENTS x

TABLE OF CONTENTS xi

LIST OF TABLES xiv

LIST OF FIGURES xv

LIST OF SYMBOLS xix

CHAPTERS

1 INTRODUCTION 1

2 LITERATURE REVIEW 5

2.1 Fundamentals of Shale Reservoirs 5

2.2 Decline Curve Analysis 10

2.3 Analytical / Semi-Analytical Models 16

2.4 Numerical Reservoir Simulation 24

2.4.1 Dual-Porosity Approach 25

3 STATEMENT OF PROBLEM 31

4 TIME-DEPENDENT SHAPE FACTORS 33

4.1 Methodology 33

4.2 Dual-Porosity Formulation 34

4.3 Constant Fracture Pressure Boundary Condition 37

4.3.1 Slab 44
4.3.2 Bar 46
4.3.3 Cube 48
4.3.4 Cylinder 50
4.3.5 Sphere 52
4.3.6 Validation 54
4.4 Constant Rate (Flux) Boundary Condition 57
4.4.1 Validation 63
4.5 Constant Fracture Pressure Followed by Linearly Declining Fracture Pressure Boundary Condition 65
4.5.1 Validation 73
5 DECLINE CURVE ANALYSIS 75
5.1 Methodology 75
5.2 Mechanistic Model 76
5.3 New Empirical Function 78
5.4 Sensitivity Analysis 79
5.4.1 Matrix Permeability 81
5.4.2 Matrix Porosity 83
5.4.3 Matrix Rock Compressibility 85
5.4.4 Fracture Spacing 87
5.4.5 Fracture Half-Length 89
5.4.6 Fracture Conductivity 89
5.4.7 Fracture Rock Compressibility 90
5.4.8 Empirical Function 91

6 CONCLUSIONS AND RECOMMENDATIONS 93

REFERENCES 97

APPENDICES

A. Constant Fracture Pressure Solution 113

B. Constant Rate (Flux) Solution 118

C. Constant Fracture Pressure Followed by Linearly Declining Fracture Pressure Solution 127

D. Publication and Award 135

CURRICULUM VITAE 137

LIST OF TABLES

TABLES

Table 2.1: Common Decline Models for Hydraulically Fractured Tight Rocks (modified from Tan et al. (2018)) 15
Table 2.2: Shape Factor Comparison 29
Table 4.1: Dimensionless Mean Matrix Pressure and Time-Dependent Shape Factors for Different Matrix Shapes 41
Table 4.2: Mean matrix pressure and shape factor for slab matrix in dual-porosity model 44
Table 4.3: Mean matrix pressure and shape factor for bar matrix in dual-porosity model 46
Table 4.4: Mean matrix pressure and shape factor for cubic matrix in dual-porosity model 48
Table 4.5: Mean matrix pressure and shape factor for cylindrical matrix in dual-porosity model 50
Table 4.6: Mean matrix pressure and shape factor for spherical matrix in dual-porosity model 52
Table 4.7: Input parameters for numerical simulation of single-porosity (SP) and dual-porosity (DP) models 55
Table 5.1: Semi-analytical model parameters 80

LIST OF FIGURES

FIGURES

Figure 1.1: The resource triangle for oil and gas deposits (Martin et al., 2010)..... 1
Figure 1.2: Major tight oil and shale gas plays in United States (EIA (2021a))..... 2
Figure 1.3: Effect of tight oil production in US total oil production (EIA (2021b)) 3
Figure 1.4: Effect of dry shale gas production in US total gas production (EIA (2021c)) 3
Figure 2.1: Ranking system for shale resources based on TOC, depth, thickness and maturity (Gandossi et al. (2017)) 6
Figure 2.2: Comparison of pore-size classification with another one proposed by Rouquerol et al. (1994) (Loucks et al. (2012)). 7
Figure 2.3: Pore space distribution of organic rich shale matrix (Passey et al. (2010))..... 8
Figure 2.4: Logarithmic difference in pore throat size measurements (Nelson (2009))..... 8
Figure 2.5: Permeability ranges associated with reservoir types requiring hydraulic fracturing (King (2012)). 9
Figure 2.6: Multi-scale gas flow with different transport mechanisms (modified from Javadpour et al. (2007))..... 10
Figure 2.7: Variation of *b* exponent with flow regime based on symmetric reservoir model bounded by two no-flow boundaries (Modified from Varma et al. (2018)). 13
Figure 2.8: Conceptual model of slab matrix linear model in hydraulically fractured well (Bello (2009))..... 17
Figure 2.9: Trilinear conceptual model for three contiguous media (Brown et al. (2009))..... 18
Figure 2.10: Top view of Triple-porosity model with sequential flow (Al-Ahmadi (2010))..... 19
Figure 2.11: Simultaneous matrix flow into MF and HF in QFM model (Ezulike and Dehghanpour (2014)) 20

Figure 2.12: Symmetric element of five-region model-one-quarter of a hydraulic fracture (Stalgorova and Mattar (2013)) 20
Figure 2.13: Symmetric element of seven region flow model (Zeng et al. (2016)) 21
Figure 2.14: Simplified model for naturally fractured reservoir (Warren and Root (1963)) 26
Figure 2.15: Pressure definitions for dual-porosity simulation (modified from Warren and Root (1963)) 27
Figure 2.16: Pressure profile for a matrix block 28
Figure 4.1: Workflow for obtaining time-dependent shape factors 34
Figure 4.2: Matrix boundary open to flow. 35
Figure 4.3: 3D anisotropic matrix geometry. 37
Figure 4.4: Mean matrix pressure behavior for slab matrix. 45
Figure 4.5: Time dependent shape factor for slab matrix. 45
Figure 4.6: Mean matrix pressure behavior for bar matrix. 47
Figure 4.7: Time dependent shape factor for bar matrix. 47
Figure 4.8: Mean matrix pressure behavior for cubic matrix 49
Figure 4.9: Time dependent shape factor for cube geometry. 49
Figure 4.10: Mean matrix pressure behavior for cylindrical matrix. 51
Figure 4.11: Time dependent shape factor for cylinder geometry. 51
Figure 4.12: Mean matrix pressure behavior for spherical matrix. 53
Figure 4.13: Time dependent shape factor for sphere geometry. 53
Figure 4.14: Comparison of dual-porosity models with single-porosity solution in average matrix pressure and cumulative water production (dashed lines). 56
Figure 4.15: Superposition principle for non-homogeneous Neumann boundary conditions 59
Figure 4.16: Time-dependent shape factor profile for an isotropic rock matrix under constant flux. 63
Figure 4.17: Comparison of dual-porosity models with single-porosity solution in bottom-hole pressure and cumulative water production. 64

Figure 4.18: Time-dependent shape factor profile for an isotropic rock matrix under constant fracture pressure followed by linearly declining fracture pressure. 70
Figure 4.19: Effect of switching time on time-dependent shape factor behavior... 71
Figure 4.20: Effect of tD/t and dP parameters on time-dependent shape factor behavior..... 71
Figure 4.21: Effect of K and dP parameters on time-dependent shape factor behavior..... 72
Figure 4.22: Comparison of dual-porosity models with single-porosity solution in mean matrix pressure. 74
Figure 5.1: Workflow followed in *b* exponent analysis..... 76
Figure 5.2: Comparison of semi-analytical transient dual-porosity model with fine-scale reservoir simulation. 78
Figure 5.3: Sensitivity analysis for matrix permeability..... 81
Figure 5.4: The q vs. *b* exponent behavior in dimensionless time for matrix permeability. 82
Figure 5.5: The *b* exponent behavior of empirical function for matrix permeability. 83
Figure 5.6: Sensitivity analysis for matrix porosity..... 84
Figure 5.7: The q vs. *b* exponent behavior in dimensionless time for matrix porosity. 84
Figure 5.8: The *b* exponent behavior of empirical function for matrix porosity. ... 85
Figure 5.9: Sensitivity analysis for matrix rock compressibility. 86
Figure 5.10: The q vs. *b* exponent behavior in dimensionless time for matrix rock compressibility..... 86
Figure 5.11: The *b* exponent behavior of empirical function for matrix rock compressibility..... 87
Figure 5.12: Sensitivity analysis for fracture spacing..... 87
Figure 5.13: The q vs. *b* exponent behavior in dimensionless time for matrix fracture spacing..... 88
Figure 5.14: The *b* exponent behavior of empirical function for fracture spacing. 88

Figure 5.15: Sensitivity analysis for fracture half-length. 89
Figure 5.16: Sensitivity to fracture conductivity. 90
Figure 5.17: Sensitivity analysis for fracture rock compressibility. 91
Figure 5.18: Mean matrix pressure and *b* exponent comparison for base case. 92

LIST OF SYMBOLS

SYMBOLS

a = intercept of q/G_p vs. time log-log plot (Duong's Model)

a = matrix dimension, L (Warren-Root Model)

$\hat{a}$ = exponent of t^n (Logistic Growth Model)

A = total flow area of the matrix, L^2

b = Arps hyperbolic decline exponent, dimensionless

b = matrix dimension, L (Warren-Root Model)

CLF = Compound linear flow of matrix perpendicular to $L1$ and $L2$

c = matrix dimension, L (Warren-Root Model)

c = fluid compressibility, $L \times T^2/M$ (psi^{-1} for field unit system)

c_t = total compressibility, $L \times T^2/M$ (psi^{-1} for field unit system)

c_u = unit conversion factor, dimensionless (1 for Darcy and 0.006328 for field unit system)

D = nominal decline rate, 1/T (Arps Exponential Decline Model, b=0)

D_i = initial decline rate, 1/T (Arps Hyperbolic Decline Model)

D_{limit}= instantaneous decline at which hyperbolic decline ends (Modified Hyperbolic Decline Model)

D_∞ = decline constant at infinite time (Power Law Exponential Decline)

$\widehat{D}_i$= Another decline constant equals to D_1/n (Power Law Exponential Decline)

K = carrying capacity (Logistic Growth Model)

K = decline coefficient of fracture pressure, M/L×T^3 (psi/day for field unit system)

k = permeability, L^2 (matrix or fracture, md for field unit system)

k_1 = permeability of enhanced fracture region, L^2

k_2 = permeability of matrix, L^2

l = characteristic dimension of a matrix, L (Warren-Root Model)

L = fracture spacing, L (ft for field unit system)

ΔL = distance between point of matrix's average internal pressure and point of fracture pressure, L

$L1$ = Linear flow of enhanced permeability region

$L2$ = Linear flow of matrix towards to hydraulic fracture

m = negative slope of q/G_p vs. time log-log plot (Duong's Model)

n = number of fracture set (Warren-Root Model)

n = summation number in infinite sum series

n = hyperbolic exponent (Logistic Growth Model)

n = time exponent (Power Law Exponential Decline)

n = model parameter (Stretched Exponential Decline Model)

P = pressure, M/L×T^2 ($\overline{P}$ = mean pressure, psi for field unit system)

P_{f0} = initial fracture pressure, M/L×T^2 (psi for field unit system)

P_{BHP} = well bottom-hole pressure, M/L×T^2 (psi for field unit system)

P_D = dimensionless pressure

P_{DH} = dimensionless pressure for homogeneous problem

P_{DT} = dimensionless pressure for time-dependent problem

$\bar{P}_D$ = mean dimensionless pressure

ΔP_0 = initial drawdown pressure, M/L×T^2 ($\Delta P_0 = P_i - P_{f0} = dP$, psi for field unit system)

ΔP_w =well drawdown pressure, M/L×T^2 (psi for field unit system)

R = matrix radius, L (ft for field unit system)

q = flux per unit time per unit area, L/T (Constant Flux Boundary Condition, 5.615 ft/day for field unit system)

q = flow rate, L^3/T (stb/day for field unit system)

$\hat{q}$ = volumetric flux per unit time per unit rock volume, L^3/L^3×T (day^{-1} for field unit system)

q_i = initial flow rate, L^3/T (Arps Hyperbolic Decline Model)

$\widehat{q_i}$ =rate intercept ($\neq q_i$) , L^3/T (Power Law Exponential Decline)

q = produced gas, Mscf/month (Stretched Exponential Decline Model)

q_1 = flow rate at first day, L^3/T (Duong's Model)

t = time, T (day for field unit system)

t_s = switching time, T (day for field unit system)

t = cumulative production time, T (Arps Hyperbolic Decline Model)

t = time period, # of months (Stretched Exponential Decline Model)

t_D = dimensionless time

t_{Ds} = dimensionless switching time

t_{pss} = elapsed time to reach pseudo-steady state condition, T

v_m = unit matrix volume, L^3

V = matrix volume, L^3

x_D = dimensionless distance in x-direction

Xe = Hydraulic fracture spacing, L (ft for field unit system)

X_f = Hydraulic fracture half-length, L (ft for field unit system)

y_D = dimensionless distance in y-direction

z_D = dimensionless distance in z-direction

ϕ = porosity, fraction (matrix or fracture)

σ = shape factor, $1/L^2$ ($1/ft^2$ for field unit system)

μ = fluid viscosity, M/L×T (cp for field unit system)

η = diffusivity coefficient, L^2/T (ft^2/day for field unit system)

τ = characteristic time constant (Stretched Exponential Decline Model)

CHAPTER 1

INTRODUCTION

In oil industry, Masters (1979) used resource triangle concept introduced by Gray (1977) to evaluate the gas accumulation in low porosity-low permeability Cretaceous sandstones in Canada. According to this concept, distribution of the natural resources looks like a triangle where high-grade deposits are at the top of triangle by covering smallest part of the triangle while low-grade deposits stay at the bottom and they constitute much greater portion of the triangle. In terms of oil and gas resources, this concept is depicted in **Fig. 1.1**.

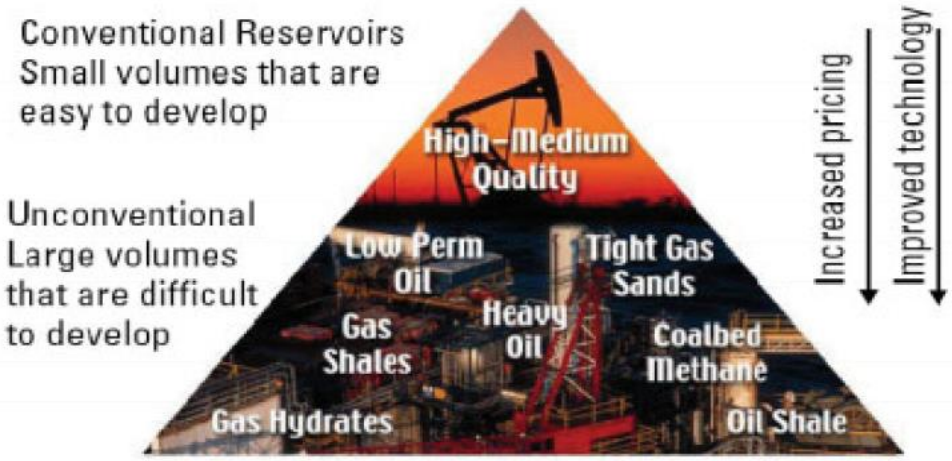

Figure 1.1: The resource triangle for oil and gas deposits (Martin et al., 2010)

However, having enormous amount of unconventional resources doesn't necessarily end up with favorable economic results. Holditch (2006) emphasized on commerciality by defining tight gas reservoir as "a reservoir that cannot be produced at economic flow rates nor recover economic volumes of natural gas unless the well is stimulated by a large hydraulic fracture treatment or produced by use of a horizontal wellbore or multilateral wellbores".

United States (US) is the leading country to utilize horizontal drilling and multi-stage hydraulic fracturing technologies to its giant tight oil/gas and shale oil/gas plays (see in **Fig. 1.2**).

Figure 1.2: Major tight oil and shale gas plays in United States (EIA (2021a))

As shown in **Fig. 1.3**, multi-stage fractured horizontal wells in shale and tight reservoirs of US has increased country production (red line) from 5 million barrel per day (MMstb/d) in 2008 to record level of 12.5 MMstb/d in 2019. Eagle Ford, Bakken and Permian (Spraberry, Wolfcamp and Bonespring) are major contributing shale plays to this production. Similarly, the US gas production has almost doubled and reached to daily total gas production of 120 billion standard cubic feet per day (Bscf/d) in 2021 (red line in **Fig. 1.4**), where almost 75 Bscf/d of it comes from shale reservoirs. Currently, Marcellus, Permian, Haynesville and Utica shale plays are dominating the shale gas production in US.

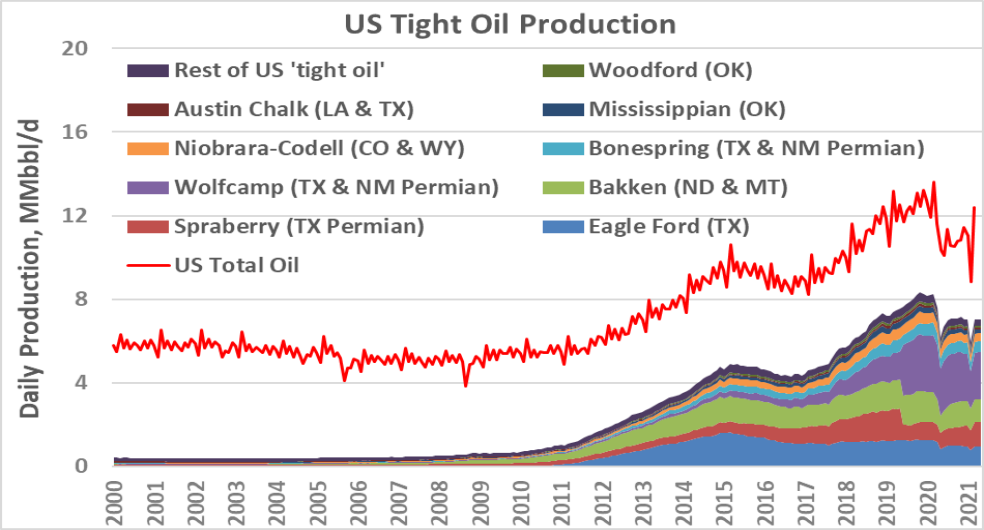

Figure 1.3: Effect of tight oil production in US total oil production (EIA (2021b))

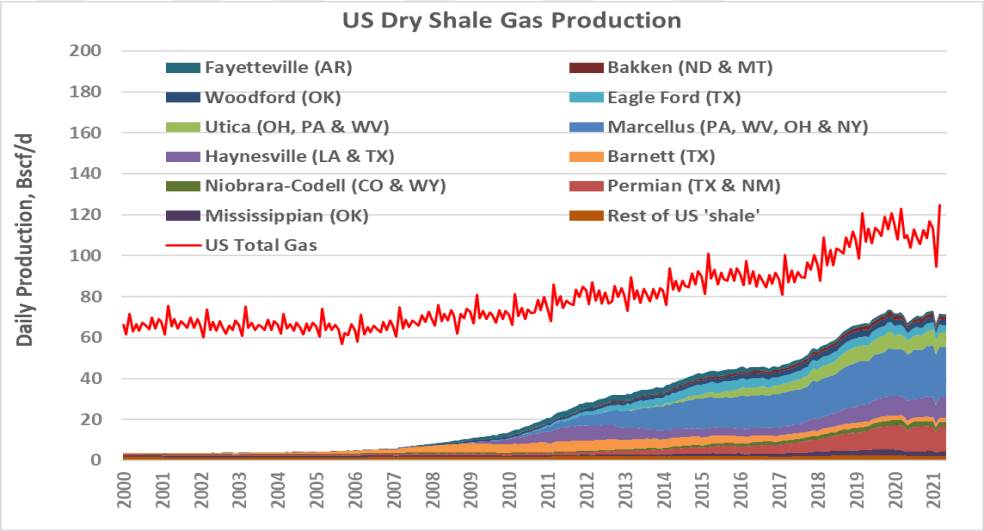

Figure 1.4: Effect of dry shale gas production in US total gas production (EIA (2021c))

Achieving high oil and gas production from these reservoirs has led to enter many new companies into this business. To assign fair value, both buyer and seller need reliable performance prediction of an associated asset. Generally, practitioner engineers in oil industry prefer to use classical historical analysis techniques even though underlying assumptions of these techniques are not valid for these new reservoirs. In performance prediction, commonly used techniques are decline curve

analysis, analytical or semi-analytical models and numerical reservoir simulation, specifically dual-porosity simulation.

This study aims to revisit validity of existing dual-porosity reservoir simulation with constant shape factors for fractured shale reservoirs. In order to assure accuracy, different types of boundary conditions are considered in derivation of analytical solutions for pressure diffusion. Validation of new time-dependent shape factors for 3D rectangular anisotropic matrix and proposed simplifications is carried out by comparing results using fine scale single-porosity numerical models. Also, time-dependent behavior of b-parameter used in hyperbolic decline curve analysis is assessed for fractured shale reservoirs by sensitivity analysis.

The thesis is organized as:

- Chapter II covers literature review of existing techniques in performance prediction of hydraulically fractured wells in shale formations.
- Chapter III presents statement of problem.
- Chapter IV provides derivation of time-dependent shape factors for different boundary conditions and their validations.
- Chapter V shows sensitivity of ***b***-exponent in hyperbolic decline curve analysis.
- Chapter VI summarizes conclusions and recommendations for future studies.

CHAPTER 2

LITERATURE REVIEW

This chapter begins with fundamentals of shale reservoirs. Main features of their geology, key reservoir parameters and transport mechanisms are provided. Then, current techniques in reservoir modeling to perform production forecasting, starting from simple to complex one will be reviewed. In this respect, first decline curve analysis, which is a simple emprical method is discussed. After that, analytical and semi-analytical models, which are idealized models of reservoirs are analyzed. Finally, details of numerical reservoir simulation methods, particularly dual-porosity formulation in fractured formations are given.

2.1 Fundamentals of Shale Reservoirs

Shale formations are very fine-grained sedimentary rocks, mostly comprised of silts, muds and clays. Apart from shales, many tight carbonate formations exist in the world. Even though most shales are clastic, carbonate components can be present as well. Concurrent deposition of very fine-grained organic material with silt, mud and clay generates shales in the form of laminated layers. Depending on thermal maturity and kerogen type, the organic content converts shales to source rock filling to conventional oil and gas reservoirs. Huge amount of remaining hydrocarbons in extremely low permeability source rocks is the current target for multi-stage fractured horizontal wells (Ahmed and Meehan (2016)).

Total organic carbon content (TOC, weight%), kerogen type, thermal maturity, mineralogy, brittleness, presence of natural fractures, stress regime, expected HC type, thickness, porosity, matrix permeability and pressure are some of the important parameters that should be considered to assess economic viability of shale reservoirs

(Kennedy et al. (2012)). Generally speaking, Type-I and Type-II kerogen with TOC greater than 2% and vitrinite reflectance (R_o) values of 0.5% to 1.1% are good for shale oil reservoirs (For example deposited in deep lake environments of China) while Type-II kerogen with TOC greater than 3% and R_o values of 0.6% to 1.5% are common in US marine shale oil reservoirs (Jiang et al. (2016)). Shale gas plays have mainly Type-III kerogen with TOC greater than 2% and R_o values of 1.1% to 1.5% (Rezaee and Rothwell (2015)). In terms of fracability, shales deposited in marine environment tend to have lower clay content and more brittle materials like quartz, feldspar and carbonates, which make them better candidates for fracking. However, non-marine shales with higher clay content are more ductile, thus they don't respond to fracking as favorably as marine shales (Ahmed and Meehan (2016)). Gandossi et al. (2017) developed the following ranking methodology illustrated in **Fig. 2.1** as screening criteria to calculate oil and gas in place for countries in the European Union.

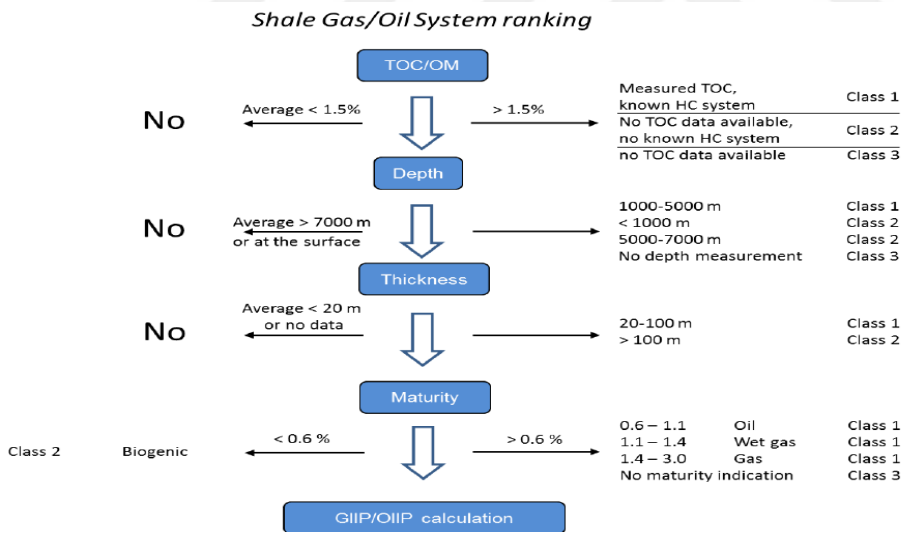

Figure 2.1: Ranking system for shale resources based on TOC, depth, thickness and maturity (Gandossi et al. (2017))

Varying pore sizes from nanometer to micrometer level creates complex matrix pore network that could be classified with three main pore types. First one is interparticle (interP) pores, which occur between particles and grains. The second one is

intraparticle (intraP) pores that are found within particles. In addition to these pores in inorganic matter, which are formed by mechanical and chemical diagenesis, organic matter pores, which are formed during maturation as intraparticle pores within organic matter constitute the third type. Interparticle pores and organic matter pores are important in terms of forming effective pore network due to their interconnectivity (Loucks et al. (2012)). Authors enhanced early classification of Choquette and Pray (1970) by adding nanopores and picopores. They also provided a pore size classification under five different categories for mud rock pores as shown in **Fig. 2.2**.

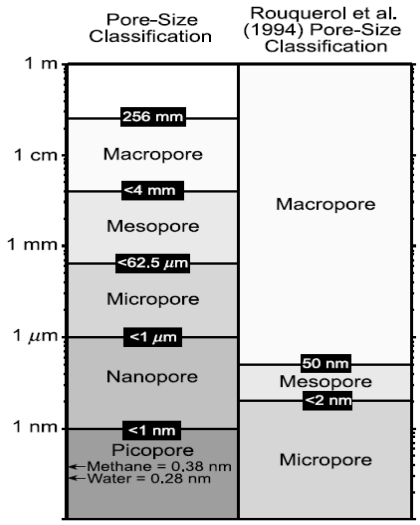

Figure 2.2: Comparison of pore-size classification with another one proposed by Rouquerol et al. (1994) (Loucks et al. (2012)).

Considering various pore types, it is quite challenging to measure porosity whether it is total or effective **(Fig. 2.3)**. Passey et al. (2010) showed disparities in calculated porosity and permeability values from different laboratories for the same sample, which is cord at the same depth to prevent vertical variability. Typical values of total porosity in shale reservoirs are in the range of 5 to 12% (Bratovich and Walles (2016)).

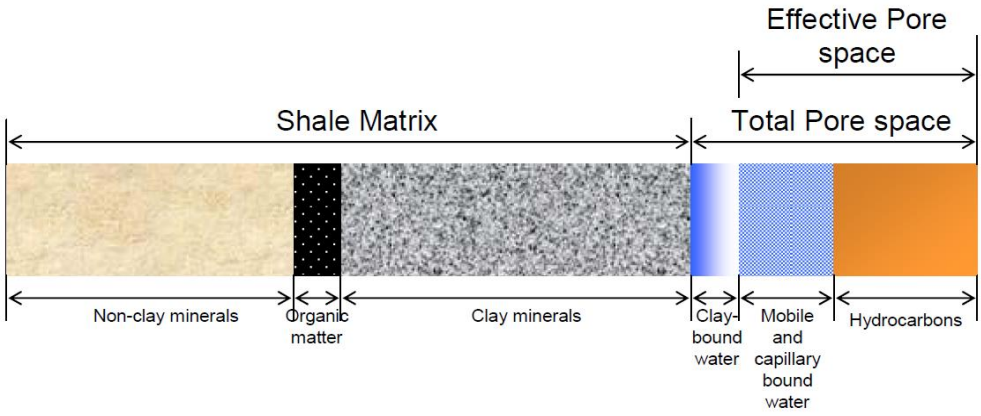

Figure 2.3: Pore space distribution of organic rich shale matrix (Passey et al. (2010)).

Nelson (2009) measured pore throat size for sandstone, tight sandstone and shale samples collected in US and Canada. He considered not only rocks but also molecular diameters of some liquids such as methane, water and mercury on logarithmic scale as illustrated in **Fig. 2.4** to highlight fluid flow through fine-grained source rocks. Smaller pore throat size results in extremely low permeability **(Fig. 2.5),** which limits wells to reach economical flow rates unless they are hydraulically fractured.

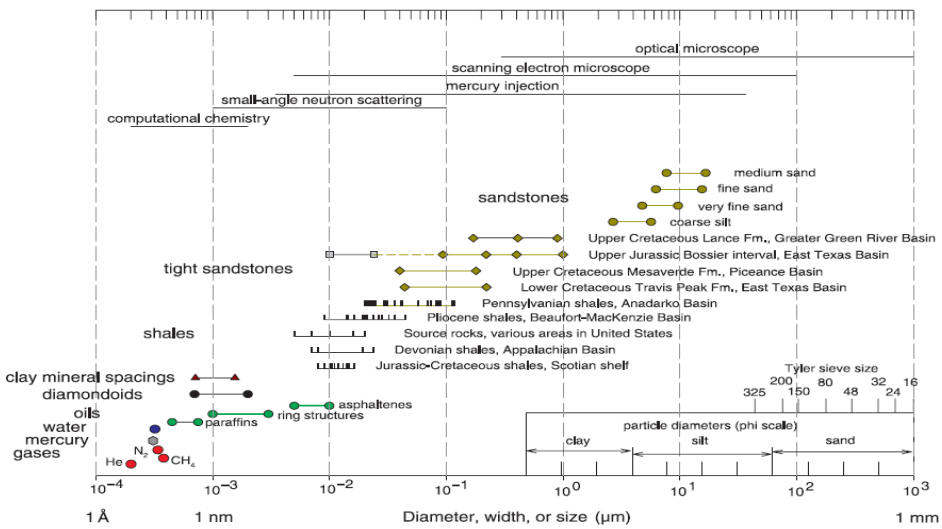

Figure 2.4: Logarithmic difference in pore throat size measurements (Nelson (2009))

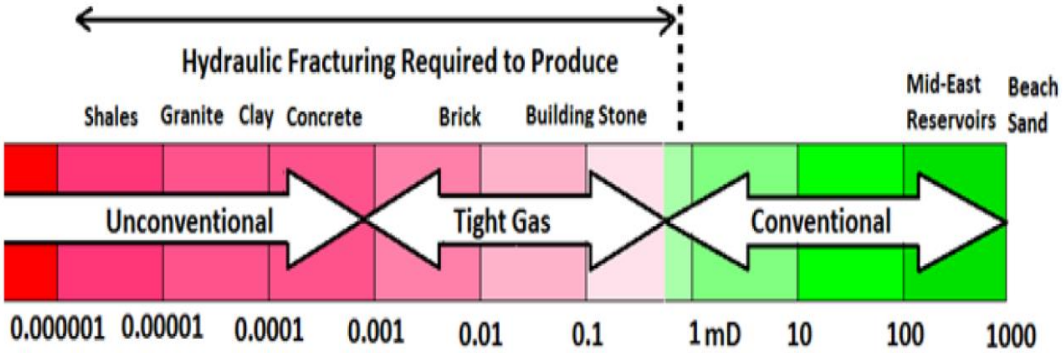

Figure 2.5: Permeability ranges associated with reservoir types requiring hydraulic fracturing (King (2012)).

Due to presence of multi-scale multi-pore systems in these formations, Javadpour et al. (2007) claimed that Darcy flow models originated from Navier-Stokes equation shouldn't be used to simulate shale gas production behavior (see in **Fig. 2.6**). Authors calculated Knudsen number, which shows the degree of deviation from continuum flow (Darcy flow) for gas mixture as a function of pressure as seen in **Fig. 2.6**. Knudsen number smaller than 0.001 results in no-slip flow, so Darcy flow is valid. However, Darcy's law is not applicable at high Knudsen numbers ranging from 0.001 to 0.1, where slip-flow conditions exist. In this region, Knudsen diffusion should be used as transport mechanism instead of Darcy flow. Multi-scale flow from multi-porosity systems in shale reservoirs has not been understood clearly. The main transport mechanism (i.e. diffusion, convection or desorption) is still a hot topic for discussion and has not been agreed on yet (Sun et al. (2015)). In addition stress dependent reservoir properties and complex fracture network formed by hydraulic fractures and in-situ (induced or not induced) fractures foster challenges in understanding and modeling of fluid flow in ultra-tight source rock (shale oil and shale gas) reservoirs.

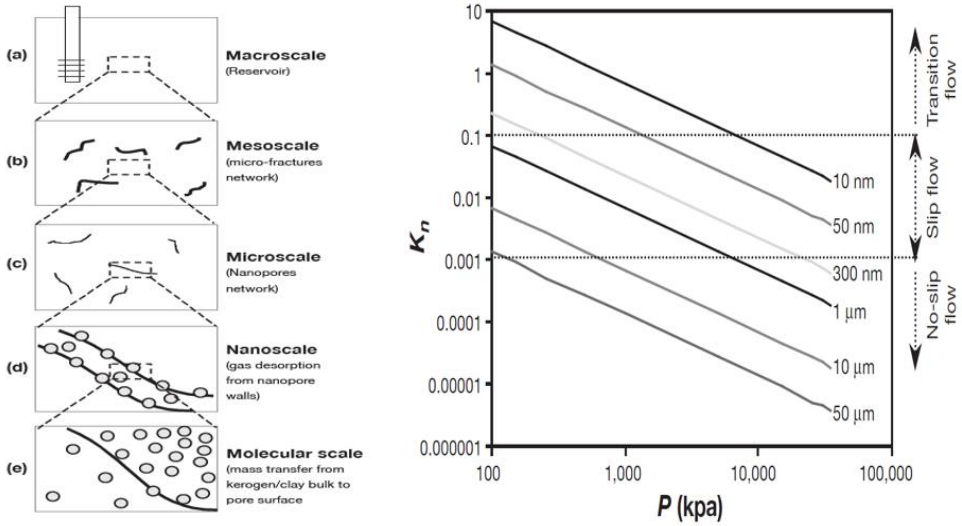

Figure 2.6: Multi-scale gas flow with different transport mechanisms (modified from Javadpour et al. (2007))

2.2 Decline Curve Analysis

Decline curve analysis has been used for many decades in the oil and gas industry for performance prediction, expected ultimate recovery (EUR) calculation and reserve estimation. Its practicality comes from not only its simplicity to use because it is just a curve fitting technique, but also it requires minimum resources as well as minimum data (i.e. rate and time). Therefore, one can easily perform production forecasting in quite large number of wells within very short time compared to other methods. Beyond that many commercially available software have advanced functionalities that enables automated decline curve analysis.

The term “decline” in this respect was first used in oil industry by Arnold and Anderson (1908). Decline was expressed as production drop percent per month. Lewis and Beal (1918) plotted percentage decline and cumulative percentage decline vs. time curves called as appraisal curves based on initial production rate in order to estimate future production for different leases. Observations in various oil field decline curves has led Cutler (1924) to use log-log plot for more reliable straight-line relationship which suggests a hyperbolic decline instead semi-log plot which

provided pessimistic results. The "loss-ratio" method was introduced by Johnson and Bollens (1927) as a novel statistical method for extrapolation of decline curves. Authors defined loss-ratio and its derivative as shown in below.

$$\text{Loss-ratio} = \frac{1}{D(t)} = \frac{-q(t)}{dq(t)/dt} \tag{1}$$

$$\text{Derivative of Loss-ratio} = b(t) = \frac{d}{dt}\left[\frac{1}{D(t)}\right] = \frac{d}{dt}\left[\frac{-q(t)}{dq(t)/dt}\right] \tag{2}$$

Contributions of many other authors to decline curve analysis before 1945 was summarized by Arps (1945) who is famous with providing mathematical equations for exponential and hyperbolic decline in terms of two distinct loss ratio case.

Accordingly, exponential decline, which has a constant loss ratio (*1/D*) is defined as:

$$q(t) = q_i e^{(-Dt)} \tag{3}$$

where q_i is initial flow rate, D is nominal decline rate (or *1/loss-ratio*), and t is cumulative production time. In order to visualize this constant percentage decline as a straight line, rate vs. time should be plotted on a semi-log paper where slope is $-D$ (or *-1/ loss-ratio*). In case of rate vs. cumulative relationship, a cartesian plot should be used to obtain straight line.

By assuming first difference of loss-ratio is constant or nearly constant, hyperbolic decline can be formulated as:

$$q(t) = \frac{q_i}{(1+bD_i t)^{1/b}} \tag{4}$$

where ***b*** is Arps hyperbolic decline exponent (*or first derivative of loss-ratio*) and D_i is initial decline rate or inverse of initial loss ratio at $t=0$. In contrast to exponential decline, decline rate is not constant, rather it is varying and decreasing according to the given formula below (Kupchenko et al. (2008)):

$$D(t) = \left(\frac{1}{D_i} + bt\right)^{-1} \tag{5}$$

As opposed to exponential decline case, a straight line is obtained from rate vs. time on log-log plot with a slope of *-1/**b***. The same log-log plot can be used for rate vs. cumulative relationship. However, both requires some shifting and attention during extrapolation. It is worth to mention that Eq. 4 is more generalized form of decline curve analysis such that extreme values of ***b*** results in exponential decline (***b***=0) or harmonic decline (***b***=1), which is a special case of hyperbolic decline.

Use of classical decline curve analysis in unconventional wells results in ***b*** values greater than unity showing that hyperbolic decline model becomes unbounded. Maley (1985) was the first to report a ***b*** value greater than unity during curve fitting of historical production for a tight gas well and questioned proper implementation of this method in order to avoid misleading EUR estimations. Rushing et al. (2007) also showed significant overestimation in EUR calculation by conducting classical decline curve analysis in tight formations. The reason for this overestimation is that existing data in unconventional wells are generally in transient flow period due to reservoir rock's tightness, violating boundary dominated flow assumption.

To overcome this problem, two different approaches have been suggested. Several studies preferred to use existing Arps hyperbolic decline model (Kupchenko et al. (2008), Fulford and Blasingame (2013), Xiong et al. (2017), Varma et al. (2018) and, Tugan and Weijermars (2020)) while investigating behavior of time-dependent ***b*** exponent using simple semi-analytical and numerical reservoir models. It has been shown that ***b*** exponent follows a different pattern for each individual flow regime **(Fig. 2.7)**. As a result, multi-segment DCA was suggested and specific values for ***b*** exponent associated to each flow regime were estimated. Fulford and Blasingame (2013) presented calculation of ***b*** exponent using Gompertz logistic function for decline of gas production in a simple fractured well model.

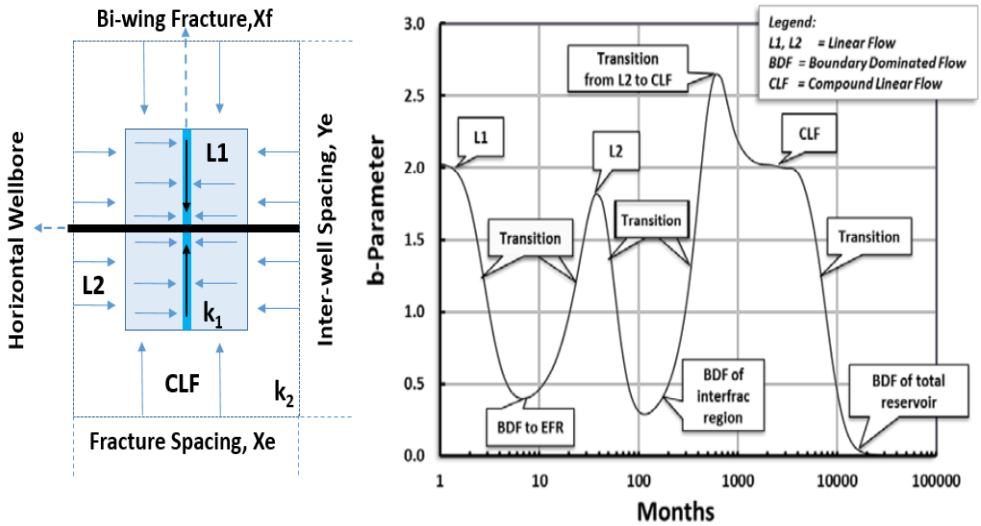

Figure 2.7: Variation of ***b*** exponent with flow regime based on symmetric reservoir model bounded by two no-flow boundaries (Modified from Varma et al. (2018)).

Second approach in eliminating failure of Arps hyperbolic decline model in tight wells is using different rate-time relations. To constrain hyperbolic model with b greater than unity, Robertson (1988) introduced *modified hyperbolic decline* by dividing historical production into two periods at which first period is modelled by hyperbolic decline. Once the instantaneous decline reaches D_{limit}, exponential decline is used during last period starting from switch point.

$$q = \begin{Bmatrix} \frac{qi}{(1+bD_i t)^{1/b}}, & D > D_{limit} \\ q_i e^{(-D_{limit} t)}, & D \leq D_{limit} \end{Bmatrix} \tag{6}$$

Ilk et al. (2008) revisited constant loss ratio case used in Arps exponential decline model and approximated loss ratio in the form of decaying power function at which late time responses are constant. Final form of *power law exponential decline model (PLE)* is given as:

$$q = \hat{q}_i e^{[-D_\infty t - \hat{D}_i t^n]} \tag{7}$$

where $\hat{q}_i$ is rate intercept (not q_i), D_∞ is decline constant at infinite time, $\hat{D}_i$ is another decline constant and it equals to D_1/n, where n is time exponent.

Observations from decline trends in group production of large number of shale gas wells led Valko (2009) and, Valko and Lee (2010) to introduce another empirical decline model called *stretched exponential decline model (SEPM).* The rate-time formula of SEPM is provided as:

$$q = q_i e^{-\left(t/\tau\right)^n} \tag{8}$$

where q_i is maximum (or initial) production rate, q is produced gas in period(mscf/month), t is period (# of months), n is model parameter and τ is characteristic time constant. Gamma function and incomplete gamma function were used to determine model parameters of n and τ from historical production by solving non-linear equations. The most important advantage of this model over Arps decline method is to bound EUR estimations without cutoffs in time or rate for shale wells, which have typically unbounded nature (***b***>1) in Arps model. However, historical production should be long enough to assign model parameters accurately in SEPM (Zuo et al. (2016)).

Duong (2011) recognized that log-log plot of q/G_p vs. time in unconventional wells shows a linear trend and derived an empirical decline model based on long-term linear flow named as fractured-dominated flow. The negative slope of "$-m$" (m is generally higher than unity for unconventional wells) and intercept of "a" on the log-log plot are two parameters to make forecast by using *Duong's model*, where flow rate is calculated based on:

$$q = q_1 t^{-m} e^{\frac{a}{1-m}\left(t^{1-m}-1\right)} \tag{9}$$

where q_1 is flow rate at first day. He showed various examples for different hydrocarbon production cases and suggested certain steps to get reliable EUR estimations from this method. Since Duong model relies only on transient flow period, Joshi and Lee (2013) proposed *modified Duong's model* by forcing q_∞ to zero and switching to hyperbolic decline when decline rate-D becomes %5 for wells having long historical production with boundary dominated flow regimes to avoid misleading remaining production estimates. EUR estimations for varying length of

production changed least in Power law exponential decline model and modified Duong model (Meyet et al. (2013)).

Clark et al. (2011) proposed Logistic Growth Model by adopting its general form to hyperbolic one to represent decline behavior observed in low permeability reservoirs. Model parameters are assigned from cumulative oil and gas production and instantaneous rate is calculated by derivative of cumulative production with respect to time as shown in below:

$$q = \frac{dQ}{dt} = \frac{Knbt^{n-1}}{(a+t^n)^2} \tag{10}$$

In addition to these methods, there are other methods like extended exponential decline and fractional decline models. Tan et al. (2018) provided a comprehensive summary of these methods and listed their advantages and disadvantages for shale gas reservoirs **(Table 2.1)**.

Table 2.1: Common Decline Models for Hydraulically Fractured Tight Rocks (modified from Tan et al. (2018))

Decline Model	Author	Rate-Time Equation
Arps Hyperbolic Decline Model	Arps (1945)	$q(t) = \frac{q_i}{(1 + bD_i t)^{1/b}}$
Modified Hyperbolic Decline Model	Robertson (1988)	$q = \begin{cases} \frac{qi}{(1 + bD_i t)^{1/b})}, & D > D_{limit} \\ q_i e(-D_{limit} t), & D \leq D_{limit} \end{cases}$
Power Law Exponential Decline Model	Ilk et al. (2008)	$q = \hat{q}_i e\left[-D_\infty t - \hat{D}_i t^n\right]$
Stretched Exponential Decline Model	Valko (2009)	$q = q_i e^{-(t/\tau)^n}$
Duong Model	Duong (2011)	$q = q_1 t^{-m} e^{\frac{a}{1-m}(t^{1-m}-1)}$
Logistical Growth Model	Clark et al. (2011)	$q = \frac{Kn\hat{a}t^{n-1}}{(\hat{a} + t^n)^2}$

To sum up, no matter which model is used, the fundamental drawback of decline curve analysis is that none of these methods has physical background. Accuracy of measured rates, presence of noise in rates, length of the historical production and

whether it is still in transient or boundary dominated period are important points to be checked before selecting any model and predicting future performance. In addition to these, any interference to subsurface and/or surface during historical production should be determined and its effect on existing trends as well as effects of planned actions in the future should be considered.

2.3 Analytical / Semi-Analytical Models

As opposed to decline curve analysis with lack of physics, analytical models include fundamental physical concepts occurring in fluid flow. They are simplified versions of reality with idealized treatment of reservoir conditions, flow regions and production scenarios in order to solve partial differential equations in an efficient way. Even though these simplifications may lead to some errors during prediction, their quick implementation is a major advantage over numerical reservoir simulation.

Multi-stage fractured horizontal wells (MFHWs) in unconventional reservoirs exhibit transient linear flow for a long time. This observation has led to development of analytical linear models in order to model historical production of these wells and perform future predictions. The common methodology followed in analytical modeling is solving diffusivity equation for defined case in Laplace domain (or other transform methods like Fourier Transform) and inverting numerically to real time domain when analytical inversion is not possible or convenient, which makes such models semi-analytical. These models can vary significantly from each other because of assumptions made during derivation. Reservoir boundary, number of flow regions, type of dual porosity, matrix geometry, equation of state, stress-sensitivity of reservoir parameters, wellbore effects like storage and skin, boundary conditions and other concepts specific to gas cases such as desorption and non-Darcy flow are some of the main aspects in having different analytical models. Many analytical models exist because of these reasons, therefore only commonly used models are described with their distinctive features.

In petroleum engineering literature, many authors like Prats et al. (1962), Gringarten et al. (1974) and, Cinco-Ley and Samaniego (1981) studied complicated cases for fractured vertical wells. However, dominant flow regime in their cases was pseudo radial flow after short duration of linear flow. Also, constant rate solution was common to analyze PBU curves as opposed to constant pressure solutions used for long-term production analysis (Wattenbarger et al. (1998)). New transient solutions to linear dual porosity model of Aguilera (1987) were provided by El-Banbi (1998) for various inner and outer boundary conditions as well as pseudo-pressure correction for gas in order to analyze fractured tight gas well performance. Bello (2009) extended this transient model in a bounded rectangular reservoir with slab matrix as shown in **Fig. 2.8** and included convergence skin to account for distortion of flow from linear to radial around wellbore in actual horizontal well. He identified five flow regions and developed asymptotic analysis equations to be used in rate transient analysis of shale gas wells.

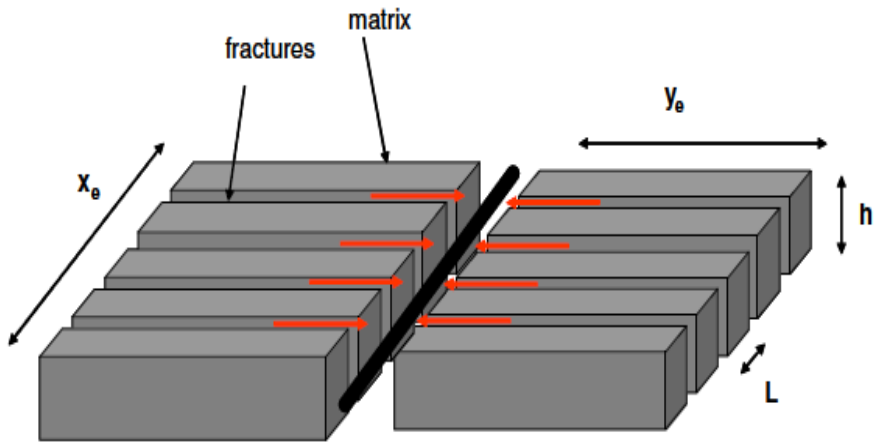

Figure 2.8: Conceptual model of slab matrix linear model in hydraulically fractured well (Bello (2009)).

Brown et al. (2009) introduced *trilinear model (TLM)* as depicted in **Fig. 2.9** for MFHWs in shale reservoirs and derived asymptotic approximations, which are limiting forms of main equation for early, intermediate and late time to assign critical

reservoir parameters. The mathematical model consists of outer reservoir region beyond stimulated rock volume (SRV), dual-porosity inner reservoir region and hydraulic fracture medium. The flow is modelled by sequential 1D linear flow in each isotropic medium. Matrix-fracture transfer model in dual-porosity inner region can be either pseudo-state (Warren and Root (1963)) or transient (Kazemi (1969), De-Swaan (1976) and Serra et al. (1983)) by appropriate f(s) parameter which also allows reducing dual porosity to single porosity in case of f(s)=1. Choking effects, wellbore storage and pseudo-pressure formulation for gas cases were included in the solution.

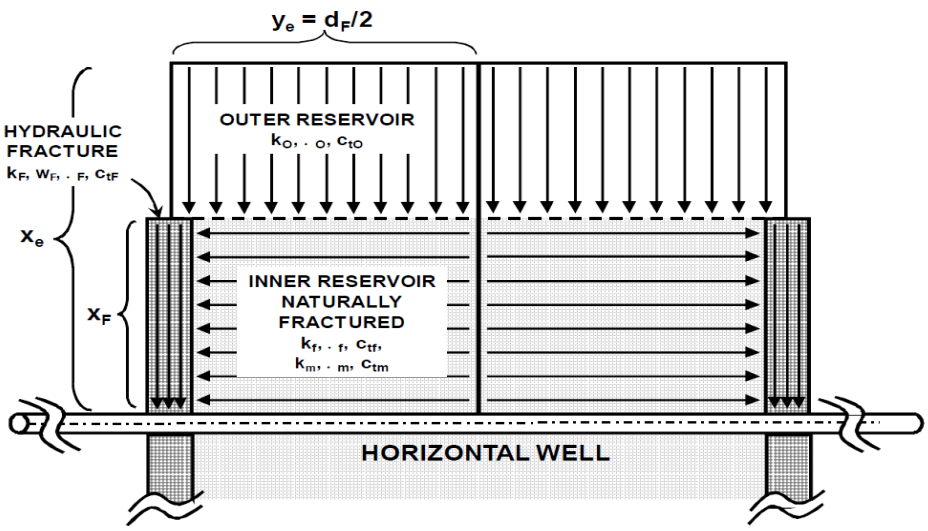

Figure 2.9: Trilinear conceptual model for three contiguous media (Brown et al. (2009))

A *triple-porosity model* was presented by Al-Ahmadi (2010) by extending linear dual-porosity model (Bello (2009)) to incorporate flow from micro-fractures. As illustrated by **Fig. 2.10**, sequential 1D linear flow occurs initially from matrix to micro fractures, then the from micro-fractures to macro-fractures. Only macro-fracture can flow to the wellbore. Analytical solutions were also provided for sub-models of triple-porosity with different inter-porosity flow assumptions either transient or pseudo-steady state, between each medium. Numerical reservoir simulation was used to verify proposed analytical solution. Fully transient state

model was used to identify flow regions observed in rate transient analysis and associated reservoir parameters were determined by using Least Squares (LS) method as a non-linear regression technique.

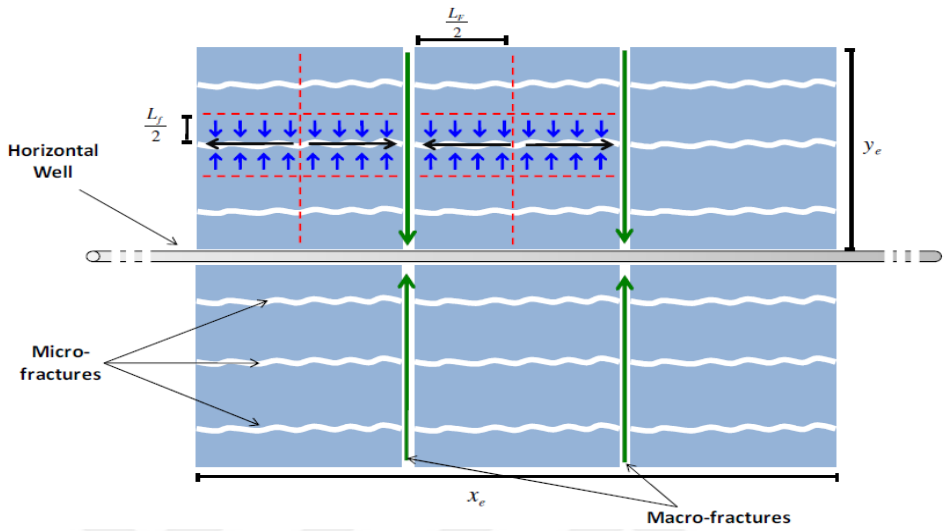

Figure 2.10: Top view of Triple-porosity model with sequential flow (Al-Ahmadi (2010))

Ezulike and Dehghanpour (2014) proposed a *quadrilinear flow model (QFM)* for reasonably high matrix-hydraulic fracture interaction cases to eliminate misleading interpretation of reservoir parameters from existing sequential flow models where matrix-micro-fracture communication is much more dominant. The sequential depletion assumption used in those models were relaxed by allowing matrix region to simultaneously feed into both micro-fractures and hydraulic fractures as seen in **Fig. 2.11**. Constant pressure and constant rate solutions were obtained in Laplace space and numerically converted to real time by Gaver-Stefhest algorithm. The QFM was validated against existing triple-porosity and linear dual porosity via type-curves.

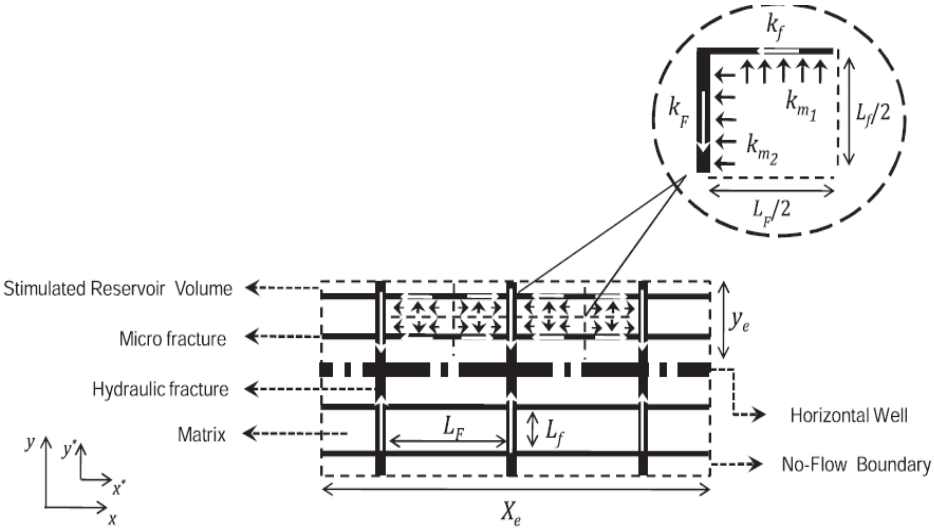

Figure 2.11: Simultaneous matrix flow into MF and HF in QFM model (Ezulike and Dehghanpour (2014))

To simulate complexity in reservoirs with MFHWs, Stalgorova and Mattar (2013) subdivided reservoir into five regions in trilinear model (Brown et al. (2009)) and amalgamated it with enhanced fracture region model (Stalgorova and Mattar (2013)) to construct a general flow model called *five-region model (FLM)*.

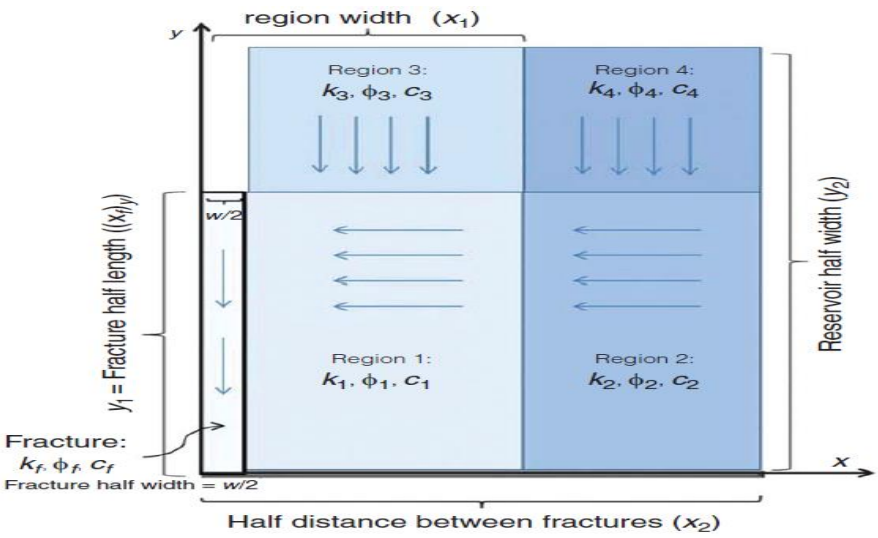

Figure 2.12: Symmetric element of five-region model-one-quarter of a hydraulic fracture (Stalgorova and Mattar (2013))

As seen in **Fig. 2.12**, Region 1 represents enhanced permeability region nearby hydraulic fracture while Region 2, Region 3 and Region 4 corresponds to unstimulated reservoir sections. Constant rate solution including wellbore storage and choking skin was obtained by solving 1D linear diffusivity equations, and its accuracy was benchmarked with fine scale numerical model. Authors also showed that provided solution is valid for different reservoir size if stimulated zone is not too small compared to whole reservoir.

To model contribution of unstimulated reservoir region in case of partially penetrating fracture, Zeng et al. (2016) added two upper/lower regions (Region 5 and Region 6) to existing five-region model as illustrated in **Fig. 2.13** and named it as *seven-flow-region model*. 1D linear flow was assumed to occur in each flow region and model verification was carried out by well testing software.

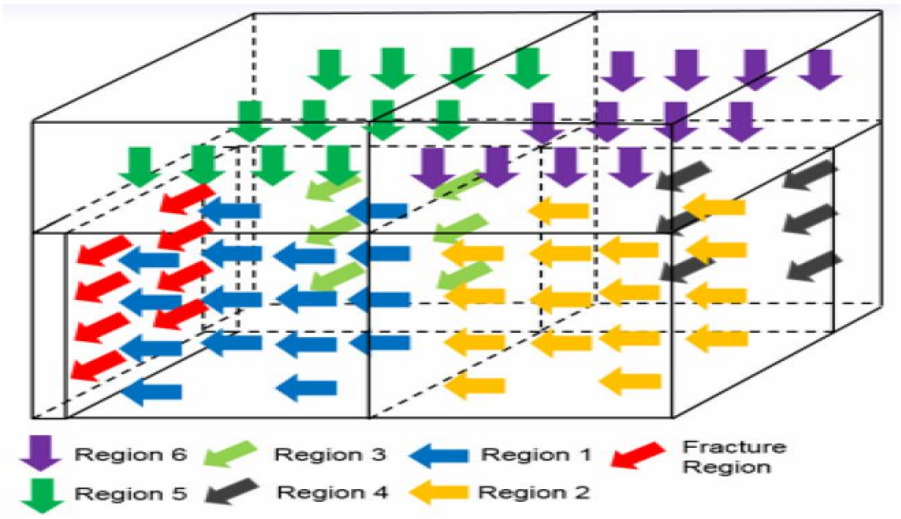

Figure 2.13: Symmetric element of seven region flow model (Zeng et al. (2016))

As mentioned previously, these models rely on simplified assumptions to allow that diffusivity equations can be handled easily. The most common assumptions of these models are:

- Hydraulic fracturing effects on pressure and saturation of defined regions are neglected and reservoir is treated as undisturbed at t=0.

- Fully penetrating well at the center of a closed reservoir with equally spaced hydraulic fractures.
- Homogeneous and isotropic regions.
- Single phase slightly compressible fluid with constant viscosity.
- Constant reservoir properties.
- Wells are producing at either constant rate or constant bottom-hole pressure

However, reality is much more different than these assumptions. These simplifications were eliminated by adding new functionalities, which obey underlying physics of related phenomena. Ren and Guo (2015) came up with a novel semi-analytical model to represent reservoir heterogeneity by different fracture lengths, different fracture spacing, various angles between the fractures and the horizontal well, fracture asymmetry, and partially penetrating fractures. Zeng et al. (2019) extended seven-flow-region model (Zeng et al. (2016)) by splitting fracture region into four new regions in order to model fracture damages like choked section at nearby wellbore, partially propped section at nearby tips and other damages at fracture face. Traditionally, variation of liquid properties and rock properties in single phase oil flow is ignored. In case of single-phase gas flow, using pseudo-pressure (Al-Hussainy and Ramey (1966)) and pseudo-time (Agarwal (1979)) allows to linearize diffusivity equation for changes in fluid properties. Qanbari and Clarkson (2013) implemented pseudo-pressure formulation while Roadifier and Kalaei (2015) and, Stalgorova and Mattar (2016) used both pseudo-pressure and pseudo-time for single phase oil flow to estimate reservoir parameters accurately.

In addition to variation of fluid properties, major changes occur in rock properties, i.e. porosity and permeability. Reduction in pore pressure due to fluid withdrawal increases net stress on the rock, which ultimately decreases porosity and permeability of the flow elements. Considerable drop in reservoir permeability significantly affects EUR and well economics in a negative manner. Change in reservoir property, especially permeability as a response to change in net stress was handled by either pseudo function method (Raghavan et al. (1972)) as in the case of variable fluid

property. Pseudo-function approach has been applied to stress-sensitive natural fractures by Ozkan et al. (2010) and Cho et al. (2013) for shale gas. Tabatabaie et al. (2017) applied both pseudo-pressure and pseudo-time formulation for liquid flow in hydraulically fractured formations with pressure-dependent permeability. The pseudo-time was calculated based on average reservoir pressure within the region of investigation proposed by Anderson and Mattar (2007). Molina (2019) extended trilinear flow model by adding exponential pressure-dependent rock and fluid properties, which increases non-linearity of partial differential equations for single-phase, slightly compressible fluid flowing at constant rate. Another method to tackle non-linearity of the problem is Pedrosa' perturbation technique where permeability modulus as a parameter in power series expansion for solution transforms nonlinear boundary value problem in a sequence of linear problems (Pedrosa (1986)) is introduced. Some authors (Wang et al. (2015), Wang and Wang (2016), Chen et al. (2016), Ji et al. (2017), Huang et al. (2019)) implemented this technique to analyze transient behavior of shale reservoirs having stress-sensitive permeability.

Shale gas modeling requires special attention due to its complex transport mechanism such as slip flow, diffusion and desorption. Having adsorbed gas on the surface of organic matter, non-Darcy flow in hydraulic fracture and stress-sensitive reservoir parameters add other challenges to its modeling. A recent semi-analytical model presented by Yu et al. (2017) incorporates a revised diffusivity equation, which considers all the major gas transport mechanisms with segmented complex non-planar fracture in order to replicate reality as much as possible. Tao et al. (2018) developed a fractal-anomalous diffusion based analytical model to enhance existing modeling capability for heterogeneous shale matrix and complex fractures.

Apart from the summarized models in this section, many other analytical/semi-analytical models have been developed with different simplified assumptions. Using them like a black box without knowing underlying assumptions can result in misleading interpretations. Therefore, selecting proper model with available data is a must before using it for any production forecast study. Including fundamental physical concepts occurring in fluid flow and its easiness to use allow engineers to

perform many analyses with analytical/semi-analytical model in a limited time as opposed to numerical reservoir simulation. However, change in pressure and saturation of defined regions due to hydraulic fracturing is neglected. Hence, model initialization is not physically correct in these models.

2.4 Numerical Reservoir Simulation

Instead of using single-averaged value for a reservoir property as in case of analytical model, spatial variation of a reservoir property can be modelled by numerical reservoir simulation. Also, pressure and saturation changes as a result of fracking are considered. The numerical reservoir simulation can model multiple wells, multiphase flow and heterogeneous reservoir properties in a 3D environment, which are not possible by analytical models (Vassilellis et al. (2016)).

The most commonly used approaches in numerical reservoir simulation of unconventional reservoirs are dual-porosity/dual-permeability (DP/DK) with local grid refinement (LGR) and discrete fracture model (DFM) (Jiang and Younis (2016)). LGR is used nearby hydraulic fracture to calculate transients accurately while dual permeability stands for matrix and small-scale fractures (Rubin (2010)). The main drawback of this approach is that hydraulic fractures should follow matrix grid alignment. Therefore, complex fracture network with non-ideal fracture geometries cannot be modeled by this approach unless some simplifications are assumed. The discrete fracture model (DFM) can overcome this limitation by generating unstructured grid on the basis of fracture geometry without any simplification. However, its high computational cost and complex setup discourage its application for history matching and optimization at the field level (Xue et al. (2019)). The embedded discrete fracture model (EDFM) was introduced by Li and Lee (2008) as a hybrid finite volume method to simulate multiphase flow in a field-scale naturally fractured reservoir. In this numerically efficient hybrid model, large fractures are modeled by discrete fracture networks while small and medium fractures are modeled by effective permeability. The lower computational cost and

high-resolution modeling capability led to get consideration from many authors (Jiang and Younis (2016), Ren et al. (2017), Yang et al. (2018) and Xue et al. (2019)) to be used in unconventional reservoir modeling.

Numerical reservoir simulation is a very powerful and reliable tool for modeling of unconventional reservoirs. It allows users to model multi-scale, multiphase fluid flow with heterogeneous rock and fluid properties under varying production/injection schedule and volume. On the other hand, enough and reliable data honoring aforementioned functionalities should be available to create a detailed model and carry out production forecast after history match. Without having enough data, which increases uncertainty, multiple reservoir models with different set of reservoir parameters could end up with same results. This questions, which model represents reality and should be used during forecast.

To sum up, numerical reservoir simulation with proper implementation replicates reality much better than other methods. However, it requires much more data, well-trained personnel, time and other resources compared to simpler methods like analytical models and decline curve analysis.

2.4.1 Dual-Porosity Approach

Since fractured rocks have complex geological and dynamic features, modeling of proper modeling of such formations is challenging. Also, matrix and fracture properties are different with orders of magnitude differences such that numerical approaches have difficulty in handling it in a stable and efficient way. Two commonly used formulations in simulation of fractured rocks are single medium (porosity) and dual-medium (porosity) approaches. In single porosity (SP) formulation, intrinsic properties are defined for each cell at its specific location. Therefore, there is no transfer term to perform flow calculations. Fractured basement rocks or high permeability reservoirs that have extremely low secondary porosity are good candidates for single-porosity modeling. However, complex nature of fracture

system doesn't allow engineers to identify fracture properties such as fracture geometry and flow properties spatially. Discrete fracture network (DFN) models could solve such problems by generating these properties stochastically for each fracture. However, such explicit definition requires much more computational time than classical way to solve equations. Therefore, DFN modeling is not very efficient for routine studies. As opposed to this approach, averaged values of reservoir properties over representative elementary volume for each matrix and fracture cell are used in dual-porosity (DP) formulation.

The dual-porosity concept was introduced by Barenblatt et al. (1960) for modeling fluid seepages into fissured rocks. Warren and Root (1963) adopted this concept to oil industry by introducing "sugar-cube" model. In this idealized model, uniform fractures and separated cubic matrix blocks represent naturally fractured reservoir as shown in **Fig. 2.14**.

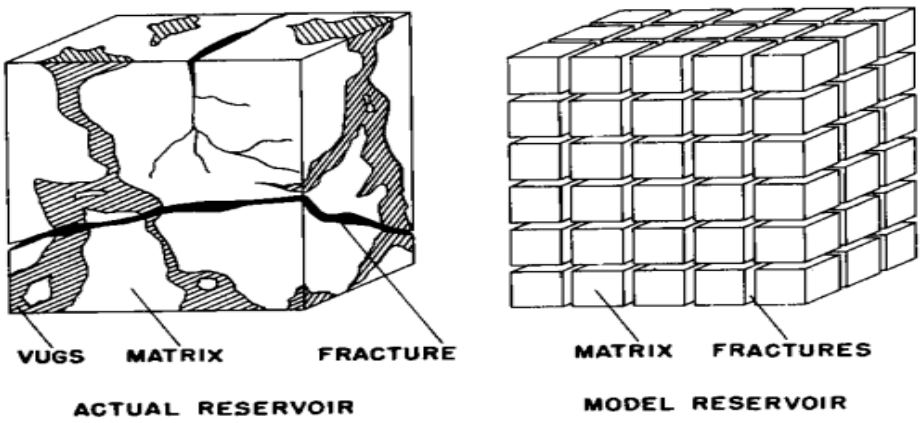

Figure 2.14: Simplified model for naturally fractured reservoir (Warren and Root (1963))

The first key assumption in dual-porosity simulation is that there is no flow within matrix itself. Instead, matrix can only flow to fracture. This assumption eliminates the need of discretization of matrix and matrix contribution is handled by a source term in fracture diffusivity equation. For the sake of simplicity, several authors including Barenblatt et al. (1960) and, Warren and Root (1963) related inter-porosity

flow term with pressure difference between average matrix pressure and fracture pressure (**Fig. 2.15**). In other words, transfer term is linear function of this pressure difference.

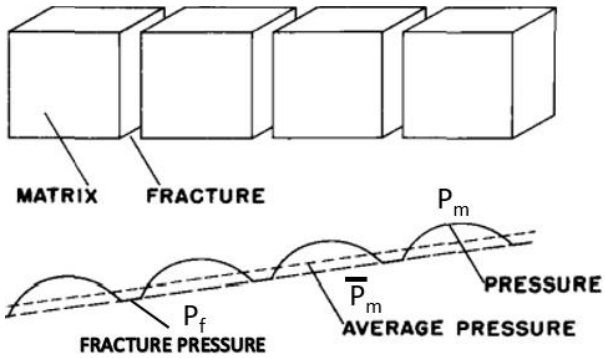

Figure 2.15: Pressure definitions for dual-porosity simulation (modified from Warren and Root (1963))

Accordingly, they defined inter-porosity flow term as (mathematical details are provided in Chapter 4):

$$q = -\left(\phi c_t\right)_m \frac{\partial \overline{P_m}}{\partial t} = -\sigma c_u \frac{k_m}{\mu}\left(P_f - \overline{P}_m\right) \tag{11}$$

where, $\hat{q}$ is volumetric flux per unit time per unit total rock volume ($L^3/L^3 \times T$), ϕ is matrix porosity (fraction), c_t is total compressibility of the matrix ($L \times T^2/M$), k_m is matrix permeability (L^2), μ is fluid viscosity ($M/L \times T$), $\overline{P_m}$ is mean matrix pressure ($M/L \times T^2$) while P_f is mean fracture pressure ($M/L \times T^2$) and c_u is unit conversion factor (it is unity for Darcy unit system and 0.006328 for field unit system).

This linear relationship is based on the pseudo-steady state flow condition for matrix, which is 2nd important assumption. Under this condition, pressure disturbance at matrix boundary reaches to center of the matrix block (dashed line in **Fig. 2.16**) within very small time ($t_{pss} \cong 0$). In other words, transient flow period (solid lines in **Fig. 3.2**) is neglected.

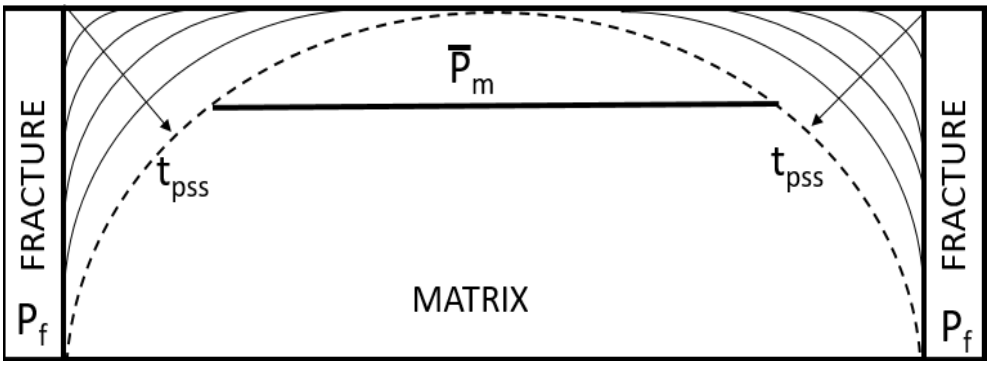

Figure 2.16: Pressure profile for a matrix block

Both authors used transfer function (or shape factor) to calculate inter-porosity flow between matrix and fracture. Barenblatt et al. (1960) related shape factor with square of total fracture surface area per unit rock volume, having unit of area^{-1}. On the other hand, Warren and Root (1963) expressed it in terms of number of fracture sets and matrix characteristic dimension with following equation:

$$\sigma = \frac{4n(n+2)}{l^2} \tag{12}$$

where, σ is shape factor (1/L^2), n is number of normal sets of fracture while l is characteristic dimension (L). This characteristic dimension was defined for 3D, 2D and 1D matrix geometry, respectively:

$$l_{n=3} = \frac{3abc}{(ab+bc+ac)}, \quad l_{n=2} = \frac{2ab}{(a+b)} \text{ and } \quad l_{n=1} = a \tag{13}$$

where, a, b and c are matrix dimensions (L) in x, y and z- direction, respectively. On the other hand, Chang (1993) represented shape factor from Darcy's Law perspective as:

$$\sigma = \frac{A}{V\Delta L} \tag{14}$$

where, A is area open to flow (L^2), V is volume of the matrix (L^3) and ΔL is distance between point of matrix's average internal pressure and point of fracture pressure (L).

Warren and Root (1963) solution was extended by Kazemi et al. (1976) for modeling two phase water-oil flow using finite difference simulator without gravity term by introducing a different shape factor definition. Coats (1989) doubled shape factor values proposed by Kazemi et al. (1976) for quasi-steady state single phase flow. Later, Ueda et al. (1989) came up with a similar proposal such that Kazemi's shape factor should be doubled and tripled for 1D and 2D flow, respectively. De-Swaan (1990) found new shape factors for slabs and cubes from semi-analytical solution of unit-step pressure change in the fractures. Chang (1993) considered different boundary conditions and provided shape factors for 1D, 2D and 3D rock matrix for pseudo-steady state flow period. In derivation of shape factors, Lim and Aziz (1995) used approximations to pressure diffusion equations like Zimmerman et al. (1993) by taking only first term in the infinite sum series. As it can be seen in **Table 2.2**, some of the proposed shape factors are different although same matrix geometry is used. More recently, Rangel-German et al. (2010) highlighted that shape factors are process dependent. Therefore, an appropriate shape factor based on flow mechanism should be chosen. Another important aspect of shape factors is that, they are constant throughout simulation time.

Table 2.2: Shape Factor Comparison

Shape Factor*L^2 (Rectangular Matrix) OR Shape Factor*R^2 (Cylindrical or Spherical Matrix)								
Matrix Geometry	Warren and Root (1963)	Kazemi et al. (1976)	Coats (1989)	Ueda et al. (1989)	De-Swaan (1990)	Chang (1993)	Zimmerman et al. (1993)	Lim and Aziz (1995)
Slab	12	4	8	8	15	π^2	π^2	π^2
Bar	32	8	16	24	-	$2\pi^2$	$2\pi^2$	$2\pi^2$
Cube	60	12	24	-	60	$3\pi^2$	$3\pi^2$	$3\pi^2$
Cylinder	-	-	-	-	-	8	5.784	5.784
Sphere	-	-	-	-	-	15	π^2	π^2

CHAPTER 3

STATEMENT OF PROBLEM

As mentioned in previous section, transfer rate between matrix and fracture in classical dual-porosity simulation depends on pressure difference between average matrix pressure and fracture pressure linearly. However, this linear relationship is due to assumption of pseudo-steady state flow condition in matrix such that any pressure disturbance at matrix boundary is felt at matrix center immediately. Therefore, transient flow period within matrix is not taken into consideration. Under this assumption, a single value of shape factor can be used throughout whole simulation period to calculate inter-porosity flow term.

Duration of transient flow depends on matrix reservoir properties and its shape. Shale formations have extremely low permeability, which results in long period of unsteady-state flow. As opposed to pseudo-steady state flow condition, pressure behavior is non-linear in transient flow period. Therefore, linear relationship between inter-porosity flow term and differential pressure does not exist during this period. In order to model non-linear pressure behavior during transient flow period in existing dual-porosity approach, shape factor should be time-dependent instead of being constant.

This study investigates accuracy of constant shape factor arising from this assumption for different matrix geometries and assess accuracy loss in production forecasts in fractured shale reservoirs. In this regard, analytical solutions of pressure diffusion and associated time-dependent shape factors are derived for 3D rectangular anisotropic matrix under different type of boundary conditions. Fine scale single-porosity numerical models are used to benchmark new time dependent shape factors. Several simplifications are proposed to mimic exact solutions for considered problems.

CHAPTER 4

TIME-DEPENDENT SHAPE FACTORS

This chapter starts with methodology section, which summarizes main steps followed during derivation of time-dependent shape factors. After revisiting dual-porosity formulation, new analytical solutions of pressure diffusion are derived for 3D rectangular anisotropic matrix under constant fracture pressure, constant rate and constant fracture pressure followed by linearly declining fracture pressure boundary conditions. Time-dependent shape factors are obtained accordingly.

4.1 Methodology

In this section, dual-porosity formulation and shape factor definitions are presented. Once time-dependent shape factor is derived in its general form, three different type of boundary conditions are studied for 3D rectangular anisotropic matrix. These are constant fracture pressure, constant rate and constant fracture pressure followed by linearly declining fracture pressure boundary conditions. After writing partial differential equation (PDE) and associated initial (IC) and boundary conditions (BCs) for pressure diffusion in matrix, their dimensionless forms are obtained from defined dimensionless parameters. Then, analytical solution of pressure diffusion for a given problem is achieved by appropriate solution technique. Finally, time-dependent shape factors are calculated from pressure solution.

Before moving to validation, shape factor profiles are generated for extended production period in order to cover extremely low permeabilities. Based on their behaviors, some empricial functions and/or reduced forms of solutions are proposed to mimic exact solutions. Verification of the derivations are done against fine-scale single porosity numerical model, where reservoir properties are obtained from literature. It is worth to mention that heterogeneties like bedding planes, lamination

and mineral composition within matrix block are not considered as well as stress dependency of reservoir properties in numerical modeling. In addition to dual-porosity model with time-dependent shape factor obtained either from simplification or from full-solution, classical dual-porosity model with constant shape factor is constructed for comparison. Summary of the workflow is depicted in **Fig. 4.1**.

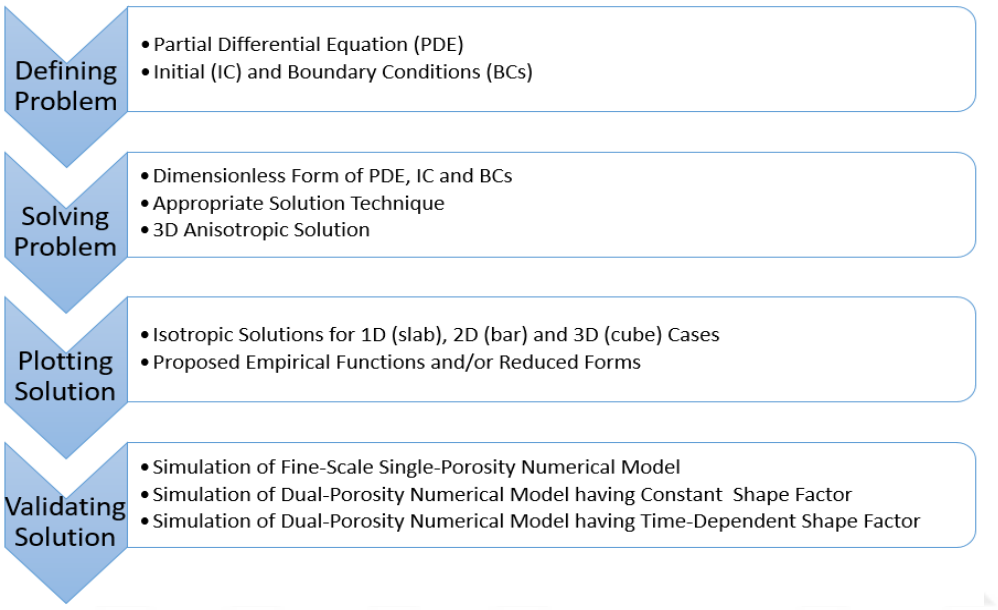

Figure 4.1: Workflow for obtaining time-dependent shape factors

4.2 Dual-Porosity Formulation

The diffusivity equation of a single-phase slightly compressible fluid in fracture medium is written as (Matthews and Russell (1967)):

$$c_u \frac{k_f}{\mu} \nabla^2 P_f(u_f, t) + q(u_f, t) = (\phi c_t)_f \frac{\partial P_f(u_f, t)}{\partial t} \tag{15}$$

Similarly, it can be written for matrix medium as:

$$c_u \frac{k_m}{\mu} \nabla^2 P_m(u_m, t) = (\phi c_t)_m \frac{\partial P_m(u_m, t)}{\partial t}$$

(16)

Even though fractures constitute a small portion of the reservoir, it dominates fluid transport. As a result, fracture diffusivity equation is written on total volume with bulk properties in dual-porosity formulation. Matrix is main medium in total storage capacity of system such that it is treated as a source term in the diffusivity equation of fracture. Therefore, matrix domain is not discretized, which reduces computation time. Since flow from matrix to fracture occurs only at matrix boundary ($u_m = u_f$), it is not included in matrix diffusivity equation (Eq. 16). From Darcy's Law, Duguid and Lee (1977) calculated flux term between two mediums by integrating it over matrix boundary (**Fig 4.2**) as:

$$q(u_f, t) = \frac{1}{v_m} \int_{\partial V_m} -c_u \frac{k_m}{\mu} \frac{\partial P_m}{\partial n} dA \tag{17}$$

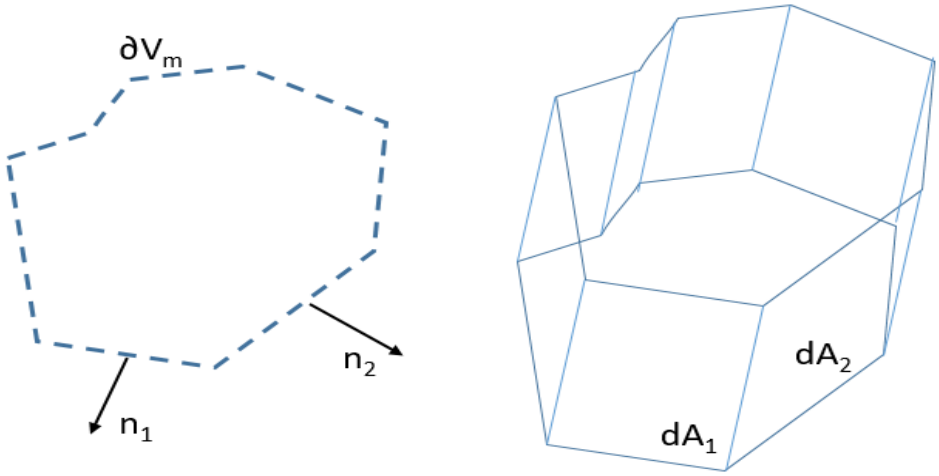

Figure 4.2: Matrix boundary open to flow.

Volume integration is used to find average matrix pressure and divergence theorem allows converting volume integral of Laplacian term in matrix diffusivity equation to surface integral (see Zimmerman et al. (1993) for details). Then, flux term becomes:

$$\frac{1}{v_m} \int_{\partial V_m} c_u \frac{k_m}{\mu} \frac{\partial P_m}{\partial n} dA = (\phi c_t)_m \frac{\partial \overline{P_m}(u_f, t)}{\partial t} = -q(u_f, t) \tag{18}$$

Having an average matrix pressure of:

$$\overline{P_m}(u_f,t)=\frac{1}{v_m}\int_{V_m}P_m(u_m,t)dV \tag{19}$$

Flow condition is assumed as quasi-steady state to calculate source term such that transfer rate from matrix to fracture is a linear function of pressure difference (Barenblatt et al. (1960) and, Warren and Root (1963)). Final relation of inter-porosity flow term with respect to average matrix pressure and shape factor can be written as:

$$q=-\left(\phi c_t\right)_m\frac{\partial\overline{P_m}}{\partial t}=-\sigma c_u\frac{k_m}{\mu}\left(P_f-\overline{P}_m\right) \tag{20}$$

Then, time-dependent shape factor in dual-porosity approach becomes:

$$\sigma(t)=\frac{1}{\eta_m}\frac{1}{P_f-\overline{P_m}}\frac{\partial\overline{P_m}}{\partial t} \tag{21}$$

Having a matrix diffusivity coefficient:

$$\eta_m=\frac{c_u k_m}{(\phi c_t)_m\mu} \tag{22}$$

where, $\nabla^2$is Laplacian which takes specific form based on coordinate system (cartesian, cylindrical or spherical), u is position vector, v_m is unit matrix volume , ∂V_m is matrix boundary, n direction of outward unit normal vector to matrix, $\hat{q}$ is volumetric flux per unit time per unit total rock volume ($L^3/L^3\times T$), ϕ is matrix porosity (fraction), c_t is total compressibility of the matrix ($L\times T^2/M$), σ is shape factor ($1/L^2$), k_m is matrix permeability (L^2), μ is fluid viscosity ($M/L\times T$), $\overline{P_m}$ is mean matrix pressure ($M/L\times T^2$) while P_f is mean fracture pressure ($M/L\times T^2$) and c_u is unit conversion factor (it is unity for Darcy unit system and 0.006328 for field unit system).

4.3 Constant Fracture Pressure Boundary Condition

General solution for pressure diffusion and associated time-dependent shape factor are derived for a 3D anisotropic matrix (shown in **Fig. 4.3**).

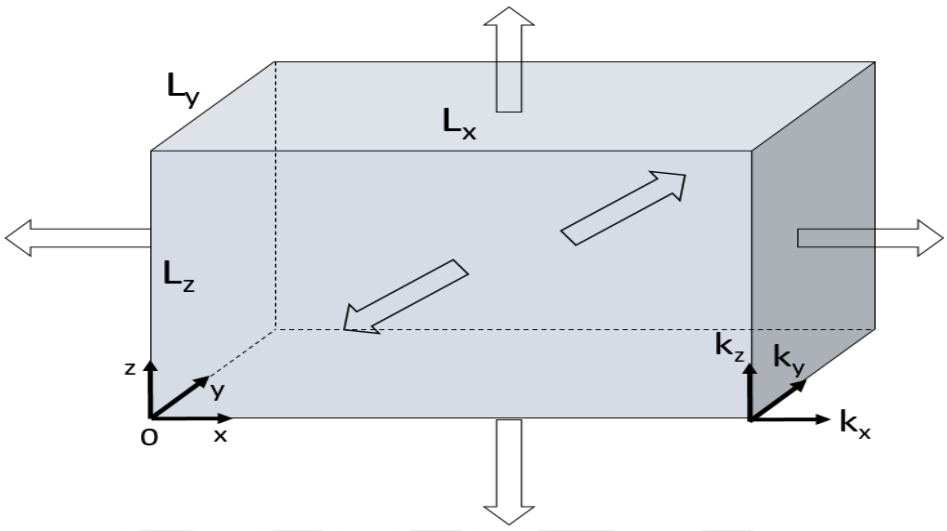

Figure 4.3: 3D anisotropic matrix geometry.

For a single-phase slightly compressible fluid, diffusivity equation (partial differential equation-PDE) in anisotropic matrix medium can be written as:

$$c_u k_x \frac{\partial^2 P}{\partial x^2} + c_u k_y \frac{\partial^2 P}{\partial y^2} + c_u k_z \frac{\partial^2 P}{\partial z^2} = (\phi \mu c_t) \frac{\partial P}{\partial t} \qquad \begin{matrix} 0 \le x \le L_x \\ 0 \le y \le L_y \\ 0 \le z \le L_z \end{matrix} \qquad (23)$$

where k_x, k_y and k_z are matrix permeability in x, y and z-direction, having fracture spacing of L_x, L_y and L_z, respectively. Initial condition (IC) and constant fracture pressure boundary conditions (BCs) for all directions are given below:

$$P(x, y, z, t = 0) = P_i \qquad (24)$$

$$P \begin{bmatrix} x = 0 \ \& \ x = L_x \\ y = 0 \ \& \ y = L_y \\ z = 0 \ \& \ z = L_z \end{bmatrix} = P_f \qquad t > 0 \qquad (25)$$

where P_i is initial pressure. To simplify original PDE given in Eq. 23, following dimensionless parameters are used:

$$P_D = \frac{P - P_i}{P_f - P_i}, \quad x_D = \frac{x}{L_x}, \quad y_D = \frac{y}{L_y}, \quad z_D = \frac{z}{L_z}, \quad t_D = \frac{c_u k_x t}{(\phi \mu c_t) L_x^2} = \frac{\eta_x}{L_x^2} t \quad (26)$$

where P_D is dimensionless pressure, x_D, y_D and z_D are dimensionless length in x, y and z-direction, t_D is dimensionless time, η_x is diffusivity coefficient in x-direction (L^2/T). Finally, PDE in dimensionless form becomes:

$$C_x \frac{\partial^2 P_D}{\partial x_D{}^2} + C_y \frac{\partial^2 P_D}{\partial y_D{}^2} + C_z \frac{\partial^2 P_D}{\partial z_D{}^2} = \frac{\partial P_D}{\partial t_D} \quad (27)$$

with coefficients of:

$$C_x = 1, \quad C_y = \frac{k_y L_x^2}{k_x L_y^2}, \quad C_z = \frac{k_z L_x^2}{k_x L_z^2} \quad (28)$$

Initial condition (IC) and boundary conditions (BCs) in all directions are also written in dimensionless form, such that:

$$P_D(x_D, y_{D,} z_D, t_D) = 0 \quad @\, t_D = 0 \quad (29)$$

$$P_D \begin{bmatrix} x_D = 0 \ \& \ x_D = 1, t_D \\ y_D = 0 \ \& \ y_D = 1, t_D \\ z_D = 0 \ \& \ z_D = 1, t_D \end{bmatrix} = 1 \quad (30)$$

As seen in Eq. 29 and Eq. 30, boundary conditions are not homogeneous. To apply separation of variable technique, problem is converted to a homogenous one by defining new dimensionless pressure (P_{DH}). Accordingly, new PDE, IC and BCs becomes:

$$P_{DH} = \frac{P_f - P}{P_f - P_i} = 1 - P_D \quad (31)$$

$$PDE: \quad C_x \frac{\partial^2 P_{DH}}{\partial x_D{}^2} + C_y \frac{\partial^2 P_{DH}}{\partial y_D{}^2} + C_z \frac{\partial^2 P_{DH}}{\partial z_D{}^2} = \frac{\partial P_{DH}}{\partial t_D} \tag{32}$$

$$IC: \quad P_{DH}(x_D, y_D, z_D, 0) = 1 \tag{33}$$

$$BCs: \quad P_{DH}(boundaries, t_D) = 0 \tag{34}$$

Based on those, analytical solution for new dimensionless pressure is obtained as (derivation details are given in Appendix A):

$$P_{DH}(x_D, y_D, z_D, t_D) = \frac{64}{\pi^3} \sum_{n=0}^{\infty} \sum_{m=0}^{\infty} \sum_{k=0}^{\infty} \frac{\exp\left\{-\left[(2n+1)^2 C_x + (2m+1)^2 C_y + (2k+1)^2 C_z\right]\pi^2 t_D\right\}}{(2n+1)(2m+1)(2k+1)} \times \sin\left[(2n+1)\pi x_D\right] \sin\left[(2m+1)\pi x_D\right] \sin\left[(2k+1)\pi x_D\right] \tag{35}$$

It is worth to mention that same solution can also be obtained by product solution technique as initial condition is suitable. By using relation in Eq. 27, P_D is found as:

$$P_D(x_D, y_D, z_D, t_D) = 1 - \frac{64}{\pi^3} \sum_{n=0}^{\infty} \sum_{m=0}^{\infty} \sum_{k=0}^{\infty} \frac{\exp\left\{-\left[(2n+1)^2 C_x + (2m+1)^2 C_y + (2k+1)^2 C_z\right]\pi^2 t_D\right\}}{(2n+1)(2m+1)(2k+1)} \times \sin\left[(2n+1)\pi x_D\right] \sin\left[(2m+1)\pi x_D\right] \sin\left[(2k+1)\pi x_D\right] \tag{36}$$

Using shape factor formula given in Eq. 21, time-dependent shape factor is calculated as:

$$\sigma_{3D}(t) = \frac{1}{\eta_m} \frac{\eta_x}{L_x^2} \pi^2 \frac{\sum_{n=0}^{\infty} \sum_{m=0}^{\infty} \sum_{k=0}^{\infty} \frac{\left[\left[(2n+1)^2 C_x + (2m+1)^2 C_y + (2k+1)^2 C_z\right] \times \exp\left\{-\left[(2n+1)^2 C_x + (2m+1)^2 C_y + (2k+1)^2 C_z\right]\pi^2 t_D\right\}\right]}{(2n+1)^2 (2m+1)^2 (2k+1)^2}}{\sum_{n=0}^{\infty} \sum_{m=0}^{\infty} \sum_{k=0}^{\infty} \frac{\exp\left\{-\left[(2n+1)^2 C_x + (2m+1)^2 C_y + (2k+1)^2 C_z\right]\pi^2 t_D\right\}}{(2n+1)^2 (2m+1)^2 (2k+1)^2}} \tag{37}$$

For an isotropic case where $k_x = k_y = k_z = k$ and $L_x = L_y = L_z = L$, time-dependent 3D shape factor can be found as:

$$\sigma_{3D}(t) = \frac{\pi^2}{L^2} \frac{\sum_{n=0}^{\infty}\sum_{m=0}^{\infty}\sum_{k=0}^{\infty} \frac{\left[\left[(2n+1)^2 + (2m+1)^2 + (2k+1)^2\right] \times \exp\left\{-\left[(2n+1)^2 + (2m+1)^2 + (2k+1)^2\right]\pi^2 t_D\right\}\right]}{(2n+1)^2 (2m+1)^2 (2k+1)^2}}{\sum_{n=0}^{\infty}\sum_{m=0}^{\infty}\sum_{k=0}^{\infty} \frac{\exp\left\{-\left[(2n+1)^2 + (2m+1)^2 + (2k+1)^2\right]\pi^2 t_D\right\}}{(2n+1)^2 (2m+1)^2 (2k+1)^2}} \tag{38}$$

In the literature, analytical solutions were obtained by same technique for different shapes like cylinder and sphere to model either heat conduction (Carslaw and Jeager (1959)) or diffusion (Crank (1975)). Based on these solutions, time-dependent shape factors are calculated from Eq. 21. Summary of mean matrix pressure in dimensionless form and time-dependent shape factors are given in **Table 4.1**.

Table 4.1: Dimensionless Mean Matrix Pressure and Time-Dependent Shape Factors for Different Matrix Shapes

MATRIX GEOMETRY	FUNCTION	SOLUTION
SLAB	$\frac{\overline{P_m}-P_i}{P_f-P_i}$	$1-\frac{8}{\pi^2}\sum_{n=0}^{\infty}\frac{exp[-\pi^2 t_D(2n+1)^2]}{(2n+1)^2}$
	$\sigma(t)$	$\frac{\pi^2}{L^2}\left[\sum_{n=0}^{\infty}\frac{exp[-\pi^2 t_D(2n+1)^2]}{(2n+1)^2}\Big/\sum_{n=0}^{\infty}\frac{exp[-\pi^2 t_D(2n+1)^2]}{(2n+1)^2}\right]$
BAR	$\frac{\overline{P_m}-P_i}{P_f-P_i}$	$1-\left(\frac{8}{\pi^2}\right)^2\sum_{m=0}^{\infty}\sum_{n=0}^{\infty}\frac{exp[-\pi^2 t_D\{(2m+1)^2+(2n+1)^2\}]}{(2m+1)^2(2n+1)^2}$
	$\sigma(t)$	$\frac{\pi^2}{L^2}\left[\frac{\sum_{m=0}^{\infty}\sum_{n=0}^{\infty}\frac{exp[-\pi^2 t_D\{(2m+1)^2+(2n+1)^2\}]}{(2m+1)^2(2n+1)^2}\{(2m+1)^2+(2n+1)^2\}}{\sum_{m=0}^{\infty}\sum_{n=0}^{\infty}\frac{exp[-\pi^2 t_D\{(2m+1)^2+(2n+1)^2\}]}{(2m+1)^2(2n+1)^2}}\right]$
CUBE	$\frac{\overline{P_m}-P_i}{P_f-P_i}$	$1-\left(\frac{8}{\pi^2}\right)^3\sum_{k=0}^{\infty}\sum_{m=0}^{\infty}\sum_{n=0}^{\infty}\frac{exp[-\pi^2 t_D\{(2k+1)^2+(2m+1)^2+(2n+1)^2\}]}{(2k+1)^2(2m+1)^2(2n+1)^2}$
	$\sigma(t)$	$\frac{\pi^2}{L^2}\left[\frac{\sum_{k=0}^{\infty}\sum_{m=0}^{\infty}\sum_{n=0}^{\infty}\frac{exp[-\pi^2 t_D\{(2k+1)^2+(2m+1)^2+(2n+1)^2\}]}{(2k+1)^2(2m+1)^2(2n+1)^2}\{(2k+1)^2+(2m+1)^2+(2n+1)^2\}}{\sum_{k=0}^{\infty}\sum_{m=0}^{\infty}\sum_{n=0}^{\infty}\frac{exp[-\pi^2 t_D\{(2k+1)^2+(2m+1)^2+(2n+1)^2\}]}{(2k+1)^2(2m+1)^2(2n+1)^2}}\right]$
CYLINDER	$\frac{\overline{P_m}-P_i}{P_f-P_i}$	$1-4\sum_{n=1}^{\infty}\frac{exp[-\beta_n^2 t_D]}{\beta_n^2}$
	$\sigma(t)$	$\frac{1}{R^2}\left[\sum_{n=1}^{\infty}exp[-\beta_n^2 t_D]\Big/\sum_{n=1}^{\infty}\frac{exp[-\beta_n^2 t_D]}{\beta_n^2}\right]$
SPHERE	$\frac{\overline{P_m}-P_i}{P_f-P_i}$	$1-\frac{6}{\pi^2}\sum_{n=1}^{\infty}\frac{exp[-n^2\pi^2 t_D]}{n^2}$
	$\sigma(t)$	$\frac{\pi^2}{R^2}\left[\sum_{n=1}^{\infty}exp[-n^2\pi^2 t_D]\Big/\sum_{n=1}^{\infty}\frac{exp[-n^2\pi^2 t_D]}{n^2}\right]$

where $t_D = \eta_m t/d^2$ is the dimensionless time and d is characteristic length equals to either thickness (L) or radius (R) of matrix depending on matrix geometry. For cylinder, β_n is the root of 1st kind of Bessel function with zero order such that $J_0(\beta_n) = 0$.

From mathematical perspective, infinite sum series in time-dependent shape factor formula are in decaying order such that adding new terms into the summation does not change final sum. Thus, first term in the summation is enough and shape factor becomes no longer time dependent. This is true if dimensionless time is higher than 0.1. Generally, this time is less than a day for most of the fractured reservoirs as previously stated by Coats (1989) and Chang (1993). That's why, linear pressure profile with constant shape factor is a valid assumption for conventional reservoirs since reaching pseudo-steady state flow condition is quite fast, resulting in loss of accuracy being limited to only very early time. However, having three orders of magnitude lower permeability than conventional reservoirs, tight rocks leads to same order of reduction in dimensionless time while keeping remaining reservoir parameters same for both cases. This reduction eventually increases required flow period to reach pseudo-steady state flow conditions by three orders of magnitude. In other words, transient period may last more than 1,000 days in a shale reservoir as opposed to 1 day for a conventional reservoir mentioned above. As highlighted by Ilk et al. (2016), this flow period can continue for most of the producing life of a well producing in an ultra-low permeability reservoir. Under these circumstances, each new term to be added into the summation beyond the first one becomes important as it directly affects final value of the shape factor. The smaller dimensionless time amplifies its effect on shape factor. Consequently, inaccuracy in fluid transfer between matrix and fracture associated with this assumption becomes significant and cannot be ignored.

In this respect, there are some approximations presented by different authors in the literature. Dykhuizen (1990) proposed two separate equations to approximate early time and late time for step-change boundary condition for slab shaped matrix. Early

time equation is used before pressure transient reaches to the center of the block named as “switch-over time”. Pruess and Wu (1993) adopted an integral solution method originally developed by Vinsome and Westerveld (1980) to determine matrix pressure as a function of initial pressure, fracture pressure, penetration depth based on diffusivity coefficient and some coefficients that must be calculated at each time step. Zimmerman et al. (1993) introduced an elegant way to handle this problem by implementing a single empirical function initially used for ion exchange by Vermeulen (1953). Using the same function with reservoir properties to approximate spherical matrix under step-rate boundary condition in dual-porosity simulation, mean matrix pressure was obtained. Proposed function was compared with those obtained using an analytical solution and Warren and Root’s approach. Results showed that empirical function is very accurate both at early time and late time as opposed to Warren and Root’s solution, which is accurate only at late time.

Studied cases mentioned above are limited in terms of geometry of matrix shape. Generally, only one type of geometry was used to test functionality of the proposed approximation. Also, minimum dimensionless time was around 1×10^{-4}, which could be much lower for rocks with extremely low permeability. Due to aforementioned concerns, detailed analysis of mean pressure behavior using its associated shape factor is conducted for different matrix geometries including cylinder and sphere. Dimensionless time range (1×10^{-10} to 10 with equally spaced 1000 points) is selected wide enough to cover extreme cases in early time and late time as well. In order to prevent any misleading calculation for extremely small values, calculation tolerance is set to 1×10^{-15}. Therefore, whenever any term in the infinite sum series is less than the given tolerance, summation operation is finalized, and it is accepted as analytical solution at the corresponding point.

To assess accuracy of the approximations, 1st term approximation with constant shape factor proposed by Chang (1993) and Lim and Aziz (1995) is considered as a starting point. Although Zimmerman et al. (1993) used Vermeulen’s simple empirical function for sphere and cube, its performance on modeling other geometries was not presented. Therefore, it is considered as an alternative method of

calculation. In addition to these methods, new empirical functions are introduced to test their capability of modeling both early and late time behavior. All of these methods are compared with exact solution for each matrix geometry, including associated absolute errors.

4.3.1 Slab

Slab matrix denotes a single fracture set with one-dimensional flow in cartesian coordinate system. It is an ideal candidate for modeling linear flow, which is commonly seen hydraulically fractured wells in unconventional reservoirs. Analyzed methods with their approximations of mean matrix pressure and shape factor are presented in **Table 4.2** for slab matrix having thickness of L.

Table 4.2: Mean matrix pressure and shape factor for slab matrix in dual-porosity model

Method	$\overline{P_D}$	**Shape Factor (σ)**
1st Term	$1-\frac{8}{\pi^2}exp[-\pi^2 t_D]$	$\frac{\pi^2}{L^2}$
Vermeulen's Function	$\sqrt{1-exp(-\pi^2 t_D)}$	$\frac{1}{2}\frac{\pi^2}{L^2}\left(1+\frac{1}{\sqrt{1-exp(-\pi^2 t_D)}}\right)$
New Empirical Function	$\sqrt{tanh(\frac{\pi^2 t_D}{2})}$	$\frac{1}{4}\frac{\pi^2}{L^2}\left[\frac{(1+tanh(\frac{\pi^2 t_D}{2}))(1+\sqrt{tanh(\frac{\pi^2 t_D}{2})})}{\sqrt{tanh(\frac{\pi^2 t_D}{2})}}\right]$

The mean matrix pressure, shape factor and corresponding absolute errors (same colors with dashed lines) for slab matrix are given in **Fig. 4.4** and **Fig. 4.5**, respectively. It is obvious that 1st term approximation to analytical solution with constant shape factor fails to represent early time behavior, which is very important for fractured shale reservoirs. Significant underestimation exists in transfer rate for this method before reaching to pseudo-steady state. Another deviation can be seen for Vermeulen's function, which overestimates shape factor by 40% before it

converges to analytical solution. On the other hand, new empirical function accurately aligns with analytical solution at each time domain except for t_D values between 0.02 and 0.3, where observed maximum error is 10%. Overall, average absolute error is less than 2% both in mean matrix pressure and transfer rate from matrix.

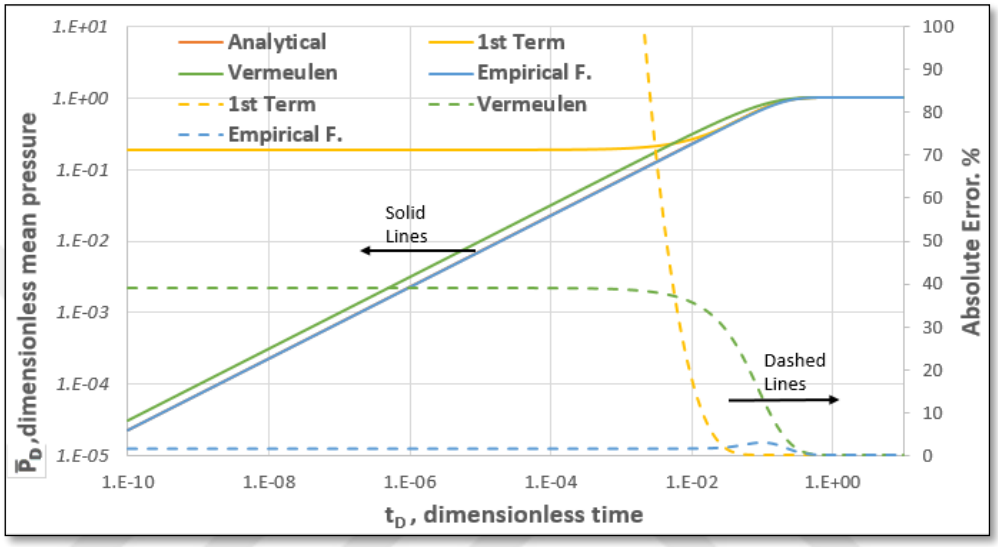

Figure 4.4: Mean matrix pressure behavior for slab matrix.

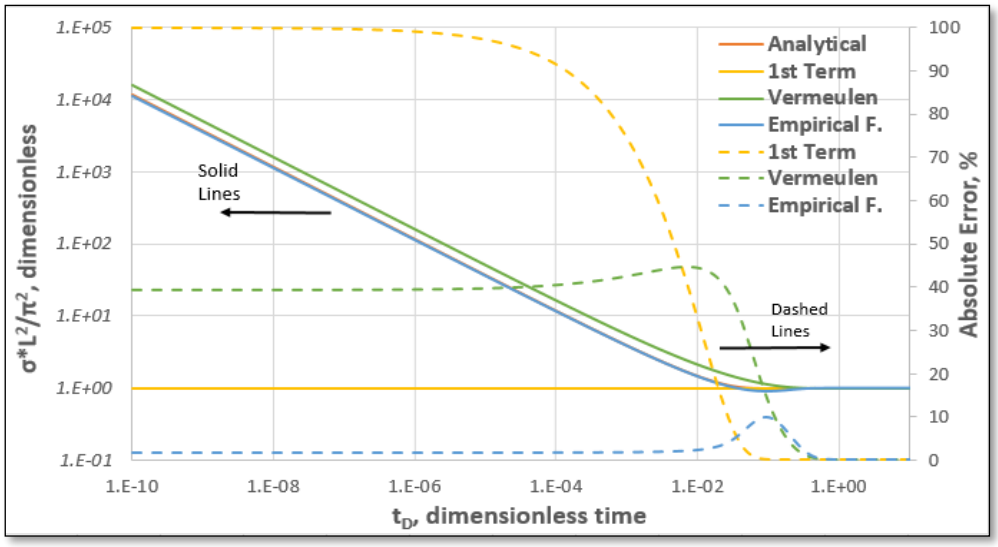

Figure 4.5: Time dependent shape factor for slab matrix.

4.3.2 Bar

For two orthogonal fracture sets, bar shaped matrix can be used to model two-dimensional flow in Cartesian coordinate system. Since number of flow surface is doubled compared to slab case, constant term in both proposed 1st function and Vermeulen's approach are multiplied by 2. In addition, another empirical function is introduced by considering exact analytical solution presented in **Table 4.1** in the form of $1-(8/\pi\times\sum sum)^2 = (1-8/\pi\times\sum sum)(1+8/\pi\times\sum sum)$ as a rough estimate, where $\sum sum = \sum exp[-(2n+1)^2\pi^2 t_D]/(2n+1)^2$. Since the behavior of $(1-8/\pi\times\sum sum)$ term is matched with new empirical function in slab matrix, it is used to obtain final form of 2nd empirical function by simple algebra. The mean matrix pressure and corresponding shape factor are given in **Table 4.3** for each method.

Table 4.3: Mean matrix pressure and shape factor for bar matrix in dual-porosity model

Method	$\overline{P_D}$	**Shape Factor (σ)**
1st Term	$1-\left(\frac{8}{\pi^2}\right)^2 exp[-2\pi^2 t_D]$	$\frac{2\pi^2}{L^2}$
Vermeulen's Function	$\sqrt{1-exp(-2\pi^2 t_D)}$	$\frac{\pi^2}{L^2}\left(1+\frac{1}{\sqrt{1-exp(-2\pi^2 t_D)}}\right)$
New Empirical Function-1	$\sqrt{tanh(\pi^2 t_D)}$	$\frac{1}{2}\frac{\pi^2}{L^2}\left[\frac{(1+tanh(\pi^2 t_D))(1+\sqrt{tanh(\pi^2 t_D)})}{\sqrt{tanh(\pi^2 t_D)}}\right]$
New Empirical Function-2	$2\sqrt{tanh(\frac{\pi^2 t_D}{2})} - tanh(\frac{\pi^2 t_D}{2})$	$\frac{1}{2}\frac{\pi^2}{L^2}\left[\frac{(1+tanh(\frac{\pi^2 t_D}{2}))(1+\sqrt{tanh(\frac{\pi^2 t_D}{2})})}{\sqrt{tanh(\frac{\pi^2 t_D}{2})}}\right]$

As it can be seen from **Fig. 4.6** and **Fig. 4.7**, 1st term approximation to analytical solution with constant shape is not capturing transient behavior. As opposed to slab matrix case, Vermeulen's function can match analytical solution with high accuracy at each time domain. Its average absolute error (dashed lines) is less than 2% except for dimensionless time values between 1×10^{-3} and 1×10^{-1}, where maximum error

reaches up to 16%. Our 1st empirical function yields 30% error before it converges to analytical solution while second one performs much better in predicting unsteady-state flow behavior. The maximum absolute error with respect to analytical solution of time-dependent shape factor is less than 10%, compared to 16% seen in Vermeulen's function. As it may be noticed the hump seen in mean matrix pressure error is magnified in shape factor error as a result of derivative form of these functions.

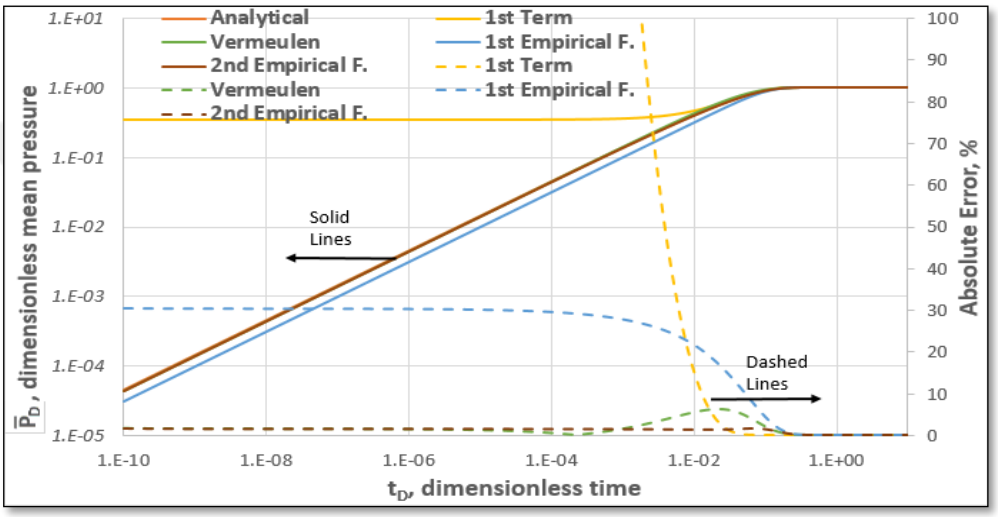

Figure 4.6: Mean matrix pressure behavior for bar matrix.

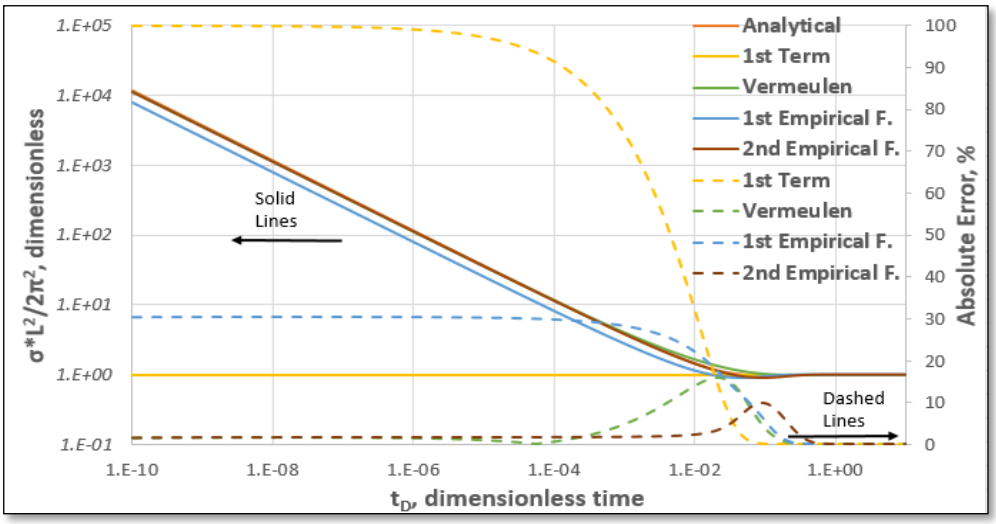

Figure 4.7: Time dependent shape factor for bar matrix.

4.3.3 Cube

Cubic matrix is used to model three orthogonal fracture sets by solving three-dimensional flow in cartesian coordinate system. Cube has six flow faces, so constant term is tripled accordingly in our 1st empirical function and Vermeulen's approach. Similar to bar shaped matrix, a rough estimate from equation of $1-(8/\pi\times\sum sum)^3=(1-8/\pi\times\sum sum)(1+8/\pi\times\sum sum+(8/\pi\times\sum sum)^2)$ is used to obtain 2nd empirical function, where $\sum sum = \sum exp[-(2n+1)^2\pi^2 t_D]/(2n+1)^2$. From slab matrix, $(1-8/\pi\times\sum sum)$ term is replaced by appropriate tanh function and final form of 2nd function was obtained. As shown in **Table 4.4**, 2nd proposed function has much more complex than 2D bar case, as expected. Taking its derivative further increases its complexity due to use of additional terms, which poses instability risk.

Table 4.4: Mean matrix pressure and shape factor for cubic matrix in dual-porosity model

Method	$\overline{P_D}$	**Shape Factor (σ)**
1st Term	$1-\left(\frac{8}{\pi^2}\right)^3 exp[-3\pi^2 t_D]$	$\frac{3\pi^2}{L^2}$
Vermeulen's Function	$\sqrt{1-exp(-3\pi^2 t_D)}$	$\frac{3}{2}\frac{\pi^2}{L^2}\left(1+\frac{1}{\sqrt{1-exp(-3\pi^2 t_D)}}\right)$
New Empirical Function-1	$\sqrt{tanh(\frac{3\pi^2 t_D}{2})}$	$\frac{3}{4}\frac{\pi^2}{L^2}\left[\frac{(1+tanh(\frac{3\pi^2 t_D}{2}))(1+\sqrt{tanh(\frac{3\pi^2 t_D}{2})})}{\sqrt{tanh(\frac{3\pi^2 t_D}{2})}}\right]$
New Empirical Function-2	$3\,tanh(\frac{\pi^2 t_D}{2})^{\frac{1}{2}} - 3\,tanh(\frac{\pi^2 t_D}{2}) + tanh(\frac{\pi^2 t_D}{2})^{\frac{3}{2}}$	$\frac{3\pi^2}{4L^2}\left[\frac{(1-tanh(\frac{\pi^2 t_D}{2})^2)\left(\frac{1}{tanh(\frac{\pi^2 t_D}{2})^{\frac{1}{2}}}-2+tanh(\frac{\pi^2 t_D}{2})^{\frac{1}{2}}\right)}{1-3\,tanh(\frac{\pi^2 t_D}{2})^{\frac{1}{2}}+3\,tanh(\frac{\pi^2 t_D}{2})-tanh(\frac{\pi^2 t_D}{2})^{\frac{3}{2}}}\right]$

The best approximation in predicting of mean matrix pressure (**Fig. 4.8**) and matrix transfer rate (**Fig. 4.9**) is achieved by 2nd proposed function. However, it loses its stability as dimensionless time exceeds unity due to its complex form. Therefore, it is suggested that this function can be used confidently before dimensionless time of unity and then simulation can continue with constant shape factor obtained from

analytical solution. The second closest match is achieved by Vermeulen's function with 20% error. On the other hand, first approximation function has 43% error in predicting mean matrix pressure and shape factor, which is much higher than slab and bar matrix cases. Like previous cases, constant shape factor is much lower than actual shape factor during unsteady-state period, which results in underestimated matrix transfer rate.

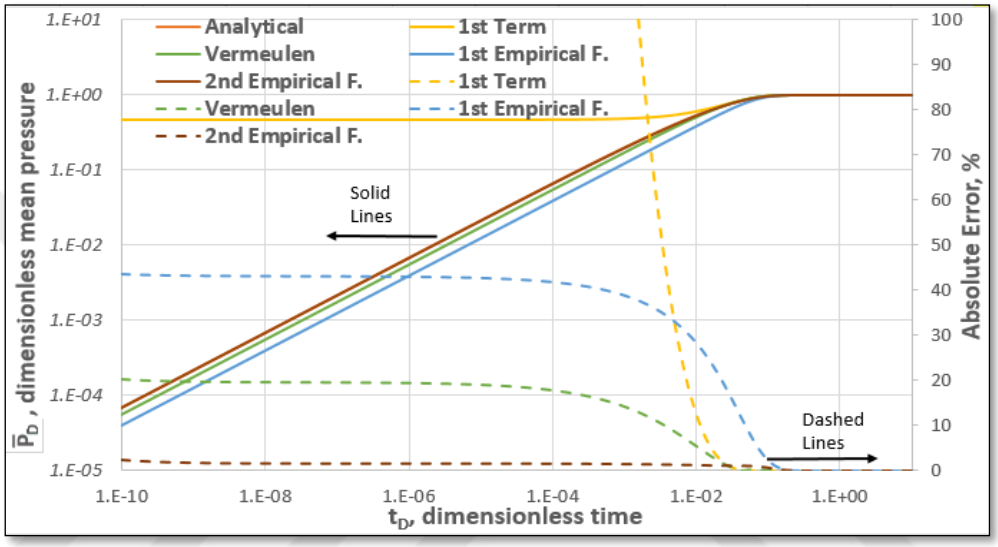

Figure 4.8: Mean matrix pressure behavior for cubic matrix

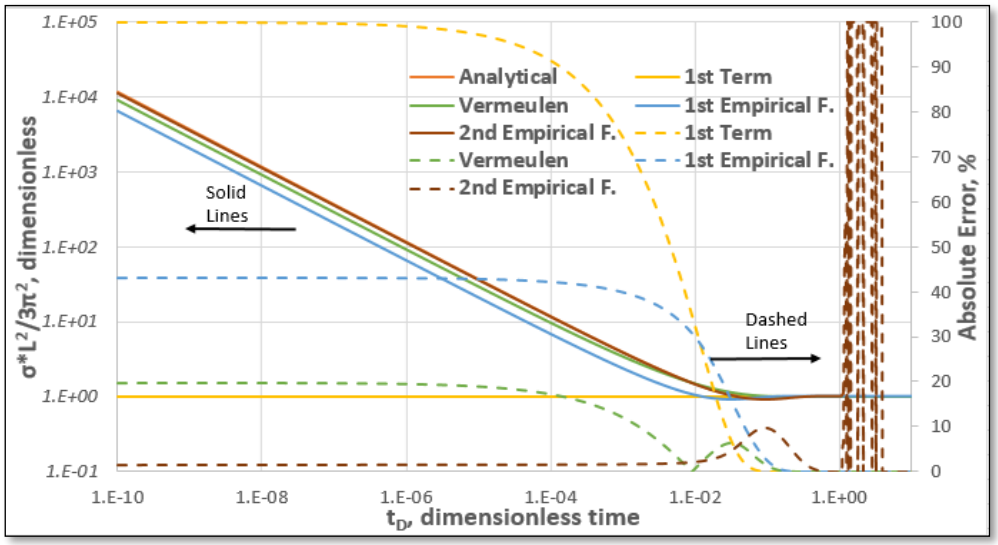

Figure 4.9: Time dependent shape factor for cube geometry.

4.3.4 Cylinder

Due to its shape, cylindrical matrix offers a practical way to model radial flow. Two-dimensional flow seen in rectangular matrix crossed with two perpendicular fracture can be approximated by this geometry. This analytical solution requires roots of Bessel function of 1st kind with zero order. Therefore, square of the first root is assigned to Vermeulen's function and our first approximation as a constant term. As shown in **Table 4.5**, modified Vermeulen's function with a smaller coefficient is also tested.

Table 4.5: Mean matrix pressure and shape factor for cylindrical matrix in dual-porosity model

Method	$\overline{P_D}$	Shape Factor (σ)
1st Term	$1-\frac{4}{5.784}exp[-5.784t_D]$	$\frac{5.784}{R^2}$
Vermeulen's Function	$\sqrt{1-exp(-5.784t_D)}$	$\frac{1}{2}\frac{5.784}{R^2}\left(1+\frac{1}{\sqrt{1-exp(-5.784t_D)}}\right)$
New Empirical Function-1	$\sqrt{tanh(5.784t_D/2)}$	$\frac{1}{4}\frac{5.784}{R^2}\left[\frac{(1+tanh(\frac{5.784t_D}{2}))(1+\sqrt{tanh(\frac{5.784t_D}{2})})}{\sqrt{tanh(\frac{5.784t_D}{2})}}\right]$
New Empirical Function-2	$\sqrt{1-exp(-\frac{\pi^2 t_D}{2})}$	$\frac{1}{4}\frac{\pi^2}{R^2}\left(1+\frac{1}{\sqrt{1-exp(-\frac{\pi^2 t_D}{2})}}\right)$

Accuracy loss of mean matrix pressure and matrix transfer rate are obvious for 1st term approximation. As illustrated in **Fig. 4.10** and **Fig. 4.11**, 1st empirical function underestimates these parameters by 24% before converging to exact solution. While Vermeulen's function has less than 10% error during transient period, error is further reduced to 2% by modified version. However, new Vermeulen's function fails at late time starting from dimensionless time of 0.1 as its coefficient leads to smaller shape factor compared to analytical one. As observed in cubic matrix, switching between

this empirical function and constant shape factor at the dimensionless time of 0.1 during simulation should be preferred in order to model actual matrix transfer rate.

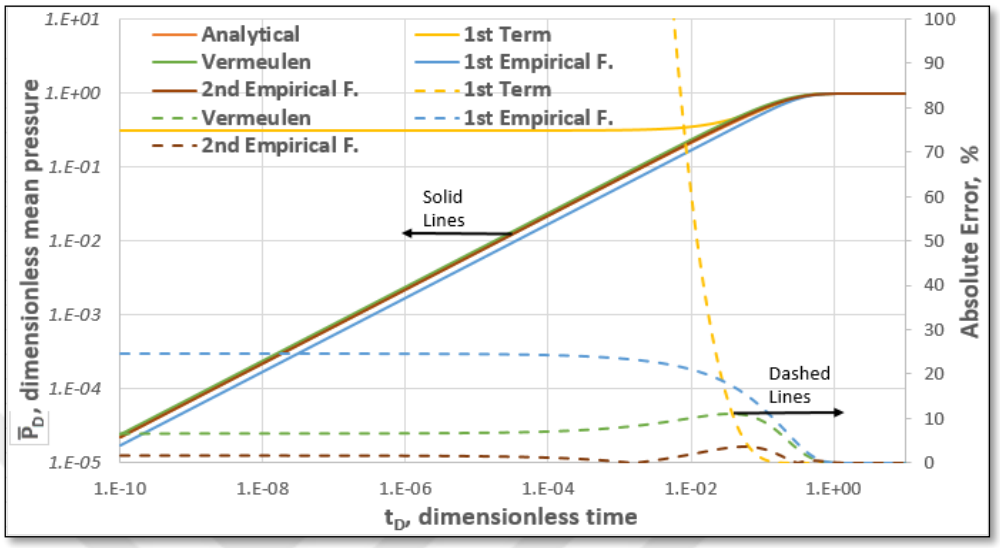

Figure 4.10: Mean matrix pressure behavior for cylindrical matrix.

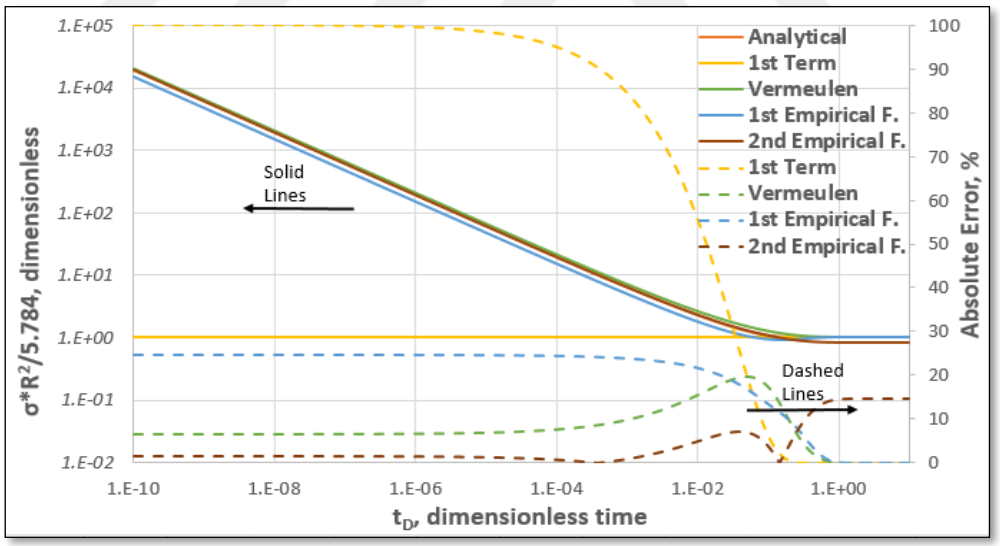

Figure 4.11: Time dependent shape factor for cylinder geometry.

4.3.5 Sphere

Spherical matrix is generally preferred to reduce three-dimensional flow to one-dimensional flow by changing variable in diffusivity equation for spherical coordinates. In case of three perpendicular fracture sets, diffusion can be modelled by considering spherical shaped matrix instead of a rectangular one. From analytical solution, constant term of π^2 is assigned to both Vermeulen's function and 1st proposed function. Zimmerman et al. (1993) mentioned another constant used by Crank (1975) for early time but they didn't show any results. That's why, it is added to list for comparison as presented in **Table 4.6**.

Table 4.6: Mean matrix pressure and shape factor for spherical matrix in dual-porosity model

Method	$\overline{P_D}$	**Shape Factor (σ)**
1st Term	$1-\frac{6}{\pi^2}exp[-\pi^2 t_D]$	$\frac{\pi^2}{R^2}$
Vermeulen's Function	$\sqrt{1-exp(-\pi^2 t_D)}$	$\frac{1}{2}\frac{\pi^2}{R^2}\left(1+\frac{1}{\sqrt{1-exp(-\pi^2 t_D)}}\right)$
New Empirical Function-1	$\sqrt{tanh(\frac{\pi^2 t_D}{2})}$	$\frac{1}{4}\frac{\pi^2}{R^2}\left[\frac{(1+tanh(\frac{\pi^2 t_D}{2}))(1+\sqrt{tanh(\frac{\pi^2 t_D}{2})})}{\sqrt{tanh(\frac{\pi^2 t_D}{2})}}\right]$
New Empirical Function-2	$\sqrt{1-exp(-36t_D/\pi)}$	$\frac{18}{\pi}\frac{1}{R^2}\left(1+\frac{1}{\sqrt{1-exp(-36t_D/\pi)}}\right)$

Similar to previous cases, 1st term approximation with constant shape factor leads to a huge deviation during unsteady-state period (**Fig. 4.12** and **Fig. 4.13**). Although 2nd empirical function with Crank's coefficient is successful at very early times with almost no error, deviation starts from a dimensionless time of 1×10^{-4}. Since $36/\pi$ is bigger than π^2, transfer rate in pseudo-steady state period is overestimated. On the other hand, 1st empirical function underestimates matrix transfer by 35% before converging to exact solution at dimensionless time of 0.5. This kind of error should

be expected since proposed function value for sphere is exactly same when compared with that of slab even tough sphere has more area to volume ratio than slab. Among others, Vermeulen's function is robust at predicting exact solution for all times with less than 10% error.

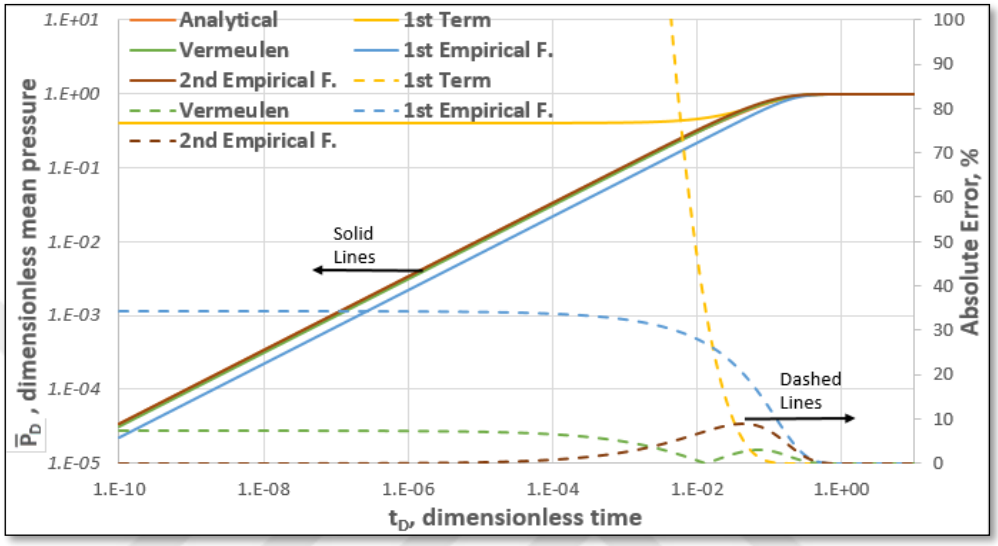

Figure 4.12: Mean matrix pressure behavior for spherical matrix.

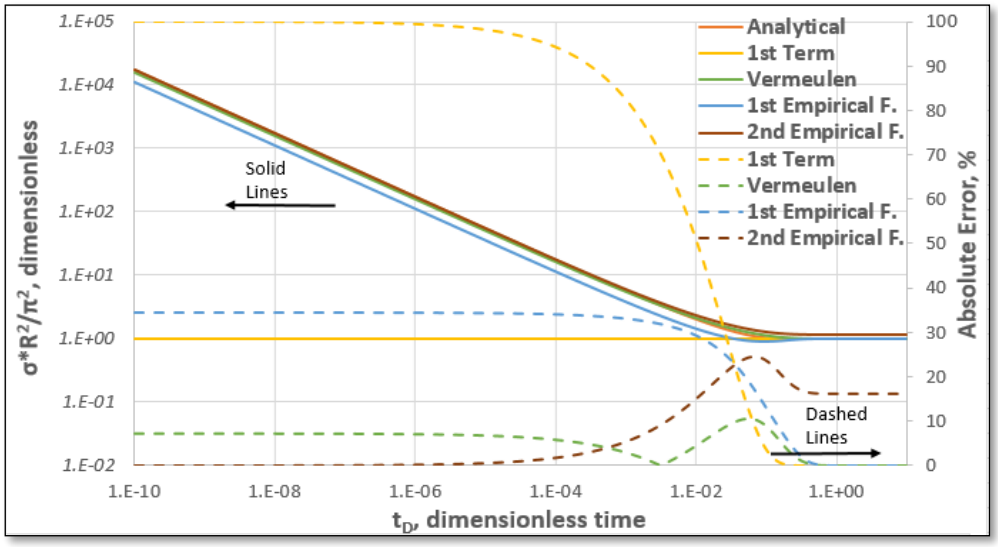

Figure 4.13: Time dependent shape factor for sphere geometry.

4.3.6 Validation

In order to show uses and advantages of proposed shape factors, a test model is prepared by considering unconventional reservoirs, which are inherently tight. Planar hydraulic fracture within shale reservoir is an ideal candidate for dual-porosity modeling with an emphasis of slab matrix. In this respect, one-dimensional model with constant reservoir properties is constructed for modeling flow in a single planar fracture. One of the key reservoir parameters in modeling such systems is fracture conductivity, which actually enhances system permeability in tight formations. Mayerhofer et al. (2017) calculated 5 md-ft for different fracture half-lengths in Middle Bakken and Three Folks. However, Shahvali et al. (2016) used 100 md-ft in simulation of hydraulically fractured wells drilled in the same basin. Therefore, 50 md-ft is assumed as representative value for fracture conductivity. Matrix porosity and permeability are taken from a study of core measurements under in-situ conditions reported by Bhandari et al. (2018) as 0.05 and 1×10^{-5} md (10 nano Darcy), respectively. Matrix rock compressibility is 1×10^{-6} psi^{-1} (Davudov et al. (2018)) and it is increased by 10 times for fracture due to its tendency for compaction (Kurtoglu (2013)). To eliminate any complexity related to fluid behavior in calculating shape factor values at each time step, water is selected as the fluid phase. Initial reservoir pressure is 7,000 psi at a depth of 10,000 ft (Weijarmars et al. (2017)) and well is controlled by constant bottom-hole pressure which is set at 2,000 psi in order to mimic high drawdown seen in these reservoirs.

Model size in the y-direction is limited to fracture length and fracture spacing per cluster is used to determine it in the x-direction. From the study by Mayerhofer et al. (2017) and Weijers et al. (2019), average fracture half-length and spacing per cluster is taken as 320 ft and 80 ft, respectively. Formation thickness is assumed to be 70 ft. As highlighted by Barree et al. (2015), production during first five year dominates economic life of the well, which is capitally intensive. Therefore, simulation period is limited to 5 years. To eliminate any discretization error, matrix cells are set as 0.75 ft along the flow direction. Instead of running fracture at its actual aperture of less

than 0.01 ft, 0.5 ft is assigned as cell width by appropriate fracture properties in order to reduce simulation time without losing accuracy (Rubin (2010)). In addition to meshing, time-step size is constrained to 1 day throughout simulation run. Bulk reservoir parameters are used for dual-porosity models and grid system is kept same with single porosity model to prevent any error related to upscaling as much as possible. Constant shape factor calculated from 1st term approximation is used in 1st dual porosity model. On the other hand, a new shape factor is calculated at each time step from the proposed function by using a script for 2nd dual-porosity model and it is overwritten in the Schedule section of the data file by MULTSIG keyword. A commercial black-oil simulator (Eclipse (2019)) was used to perform these simulation runs. **Table 4.7** presents key input parameters for simulation models.

Table 4.7: Input parameters for numerical simulation of single-porosity (SP) and dual-porosity (DP) models

PARAMETER	SP	DP	MODEL
Model Size, ft	80x640x70		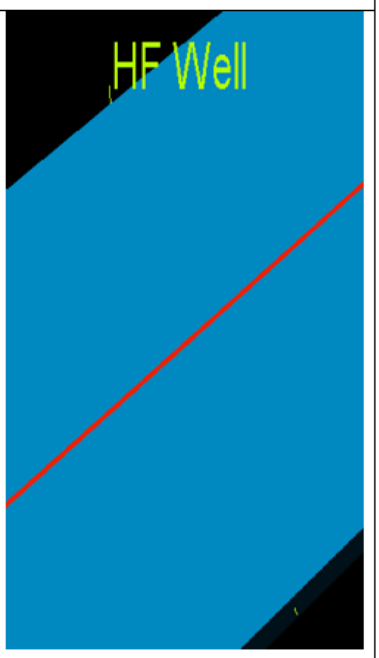
Grid System	107x1x1		
Fracture porosity, fraction	0.02	1.25×10^{-4}	
Fracture permeability, md	100 (50 md-ft)	0.625	
Matrix permeability, md	1×10^{-5}	9.94×10^{-6}	
Matrix porosity, fraction	0.05	0.0497	
Matrix Compressibility, psi^{-1}	1×10^{-6}		
Fracture Compressibility, psi^{-1}	1×10^{-5}		
Water Compressibility, psi^{-1}	1.35×10^{-5}		
Water FVF, rbbl/stb	1		
Viscosity, cp	0.35		
Time step, day	1		

Mean matrix pressure and cumulative water production are used to compare cases. As it can be seen in **Fig. 4.14**, classical dual-porosity formulation (DP) underestimates flow contribution from matrix while overestimating average pressure

in the matrix, even with 1st term of analytical solution. On the contrary, time-dependent transfer rate by using proposed empirical function (DP-N) copes with this deficiency reasonably well. Small difference with single-porosity model (SP) arises from both dual-porosity upscaling and increased error in empirical function's estimation of shape factor between t_D of 0.02 and 0.3, as mentioned earlier. Beyond that, new dual-porosity modeling accurately replicates actual reservoir responses throughout simulation period.

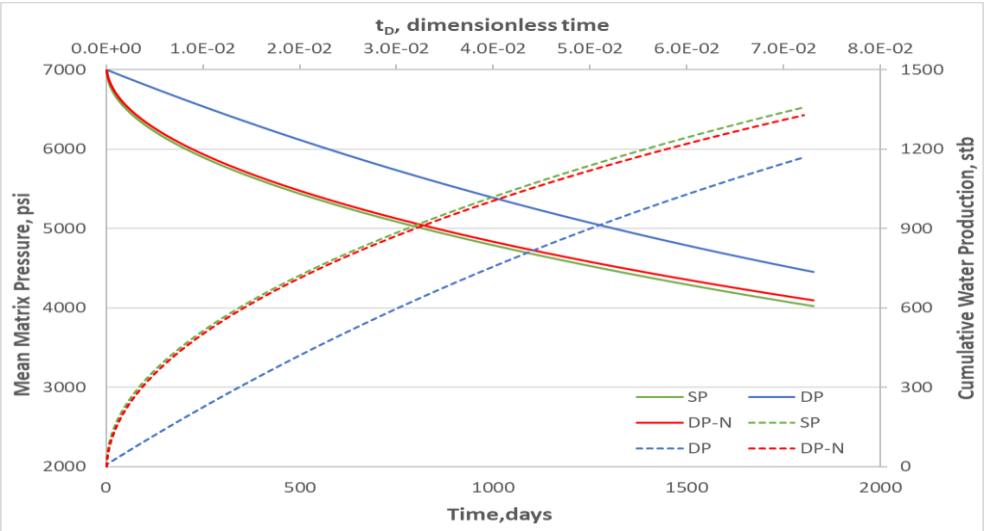

Figure 4.14: Comparison of dual-porosity models with single-porosity solution in average matrix pressure and cumulative water production (dashed lines).

Since transient time for this representative case lasts 2,566 days (more than 7 years), 1st term shape factor is expected to fail. It yields more than 6-folds larger absolute error in cumulative production (13.9% vs. 2.2%) than proposed approximation. Similarly, pressure overestimation is 5.9 times larger (10.7% vs. 1.8%). It is worth to mention that this simulation was conducted on a single planar fracture. One can easily recognize that error in flow rate will be magnified proportionally with the number of created planar fractures. Considering current industry practice of 40 stage fracturing (Weijers et al. (2019)), this error cannot be neglected. Furthermore, error in prediction grows severely with increase of formation tightness. Even though this fundamental error in existing dual-porosity modeling can be compensated by

modifying other reservoir parameters to match existing well performance, doing so adversely affects both technical and commercial assessment of the field. This study can be conducted for other matrix geometries as long as flow behavior is representative of simulated one.

4.4 Constant Rate (Flux) Boundary Condition

For a single-phase slightly compressible fluid, diffusivity equation (partial differential equation-PDE) in anisotropic matrix medium (Cartesian coordinate system) can be written:

$$c_u k_x \frac{\partial^2 P}{\partial x^2} + c_u k_y \frac{\partial^2 P}{\partial y^2} + c_u k_z \frac{\partial^2 P}{\partial z^2} = (\phi \mu c_t) \frac{\partial P}{\partial t} \qquad \begin{matrix} 0 \le x \le L_x \\ 0 \le y \le L_y \\ 0 \le z \le L_z \end{matrix} \qquad (39)$$

Initial condition (IC) and constant flux (rate per flow area) boundary conditions (BCs) for all directions are given:

$$P(x, y, z, t = 0) = P_i \qquad (40)$$

$$-c_u k_x \frac{\partial P}{\partial x} = q_x \quad @\, x = L_x \quad \& \quad -c_u k_x \frac{\partial P}{\partial x} = -q_x \quad @\, x = 0 \qquad (41)$$

$$-c_u k_y \frac{\partial P}{\partial y} = q_y \quad @\, y = L_y \quad \& \quad -c_u k_y \frac{\partial P}{\partial y} = -q_y \quad @\, y = 0 \qquad (42)$$

$$-c_u k_z \frac{\partial P}{\partial z} = q_z \quad @\, z = L_z \quad \& \quad -c_u k_z \frac{\partial P}{\partial z} = -q_z \quad @\, z = 0 \qquad (43)$$

To simplify original PDE given in Eq. 39, following dimensionless parameters are used:

$$P_D = \frac{P - P_i}{P_{f0} - P_i}, \quad x_D = \frac{x}{L_x}, \quad y_D = \frac{y}{L_y}, \quad z_D = \frac{z}{L_z}, \quad t_D = \frac{c_u k_x t}{(\phi \mu c_t) L_x^2} \qquad (44)$$

where P_D is dimensionless pressure, x_D, y_D and z_D are dimensionless length in x, y and z-direction, t_D is dimensionless time, P_{f0} is initial fracture pressure (M/L×T^2). Finally, PDE in dimensionless form becomes:

$$C_x \frac{\partial^2 P_D}{\partial x_D{}^2} + C_y \frac{\partial^2 P_D}{\partial y_D{}^2} + C_z \frac{\partial^2 P_D}{\partial z_D{}^2} = \frac{\partial P_D}{\partial t_D} \tag{45}$$

with coefficients of :

$$C_x = 1, \quad C_y = \frac{k_y L_x^2}{k_x L_y^2}, \quad C_z = \frac{k_z L_x^2}{k_x L_z^2} \tag{46}$$

Initial condition (IC) and boundary conditions (BCs) in all directions are also written in dimensionless form, such that:

$$P_D(x_D, y_{D,} z_D, t_D) = 0 \quad @\, t_D = 0 \tag{47}$$

$$\frac{\partial P_D}{\partial x_D} = f_x \quad @\, x_D = 1 \quad \& \quad \frac{\partial P_D}{\partial x_D} = -f_x \quad @\, x_D = 0, \quad f_x = \frac{q_x \mu L_x}{c_u k_x} \tag{48}$$

$$\frac{\partial P_D}{\partial y_D} = f_y \quad @\, y_D = 1 \quad \& \quad \frac{\partial P_D}{\partial y_D} = -f_y \quad @\, y_D = 0, \quad f_y = \frac{q_y \mu L_y}{c_u k_y} \tag{49}$$

$$\frac{\partial P_D}{\partial z_D} = f_z \quad @\, z_D = 1 \quad \& \quad \frac{\partial P_D}{\partial z_D} = -f_z \quad @\, z_D = 0, \quad f_z = \frac{q_z \mu L_z}{c_u k_z} \tag{50}$$

where f_x, f_y and f_z are associated flux terms (L^3×M/T^2) in x, y and z-direction, respectively.

Since this initial boundary value problem (IBVP) has non-homogenous Neumann boundary conditions (Eq. 48, Eq. 49 and Eq. 50), superposition of one-dimensional (1D) unsteady-state solutions can be used to obtain final solution (Taler (2014)). Main idea is decomposing original problem into sub-problems where only one non-homogeneous boundary condition exists. **Fig. 4.15** shows solution strategy for one-dimensional problem.

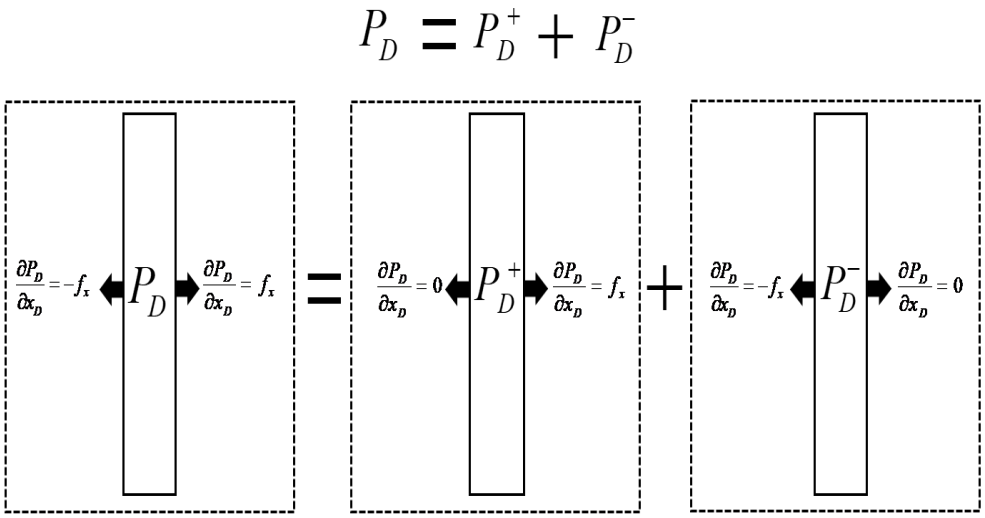

Figure 4.15: Superposition principle for non-homogeneous Neumann boundary conditions

Considering initial condition and boundary conditions, Laplace transform technique is used to reduce partial differential equation to ordinary differential equation. After solving pressure equation for each sub-problem in Laplace domain, inversion to real time domain is achieved analytically. Once pressure solution is obtained in real time domain, time-dependent shape factor is derived based on Eq. 21. Since shape factor is directly related to area open to flow per unit volume, summation of 1D shape factors yields multi-dimensional (2D or 3D) shape factors. For a 3D anisotropic matrix under constant fluxes at its boundaries, pressure solution and time-dependent shape factor are given in Eq. 51 and Eq. 52, respectively. Derivation details are provided in Appendix-B.

$$
\begin{aligned}
P_D(x_D, y_D, z_D, t_D) = {} & f_x \left\{ \begin{array}{l} \displaystyle\sum_{n=0}^{\infty} 2\sqrt{\frac{C_x t_D}{\pi}} \left[\begin{array}{l} \exp\left(\frac{-(2n+1-x_D)^2}{4t_D}\right) + \exp\left(\frac{-(2n+1+x_D)^2}{4t_D}\right) \\ + \exp\left(\frac{-(2n+2-x_D)^2}{4t_D}\right) + \exp\left(\frac{-(2n+x_D)^2}{4t_D}\right) \end{array} \right] \\ - \left[\begin{array}{l} (2n+1-x_D) erfc\left(\frac{(2n+1-x_D)}{2\sqrt{t_D}}\right) + (2n+1+x_D) erfc\left(\frac{(2n+1+x_D)}{2\sqrt{t_D}}\right) \\ + (2n+2-x_D) erfc\left(\frac{(2n+2-x_D)}{2\sqrt{t_D}}\right) + (2n+x_D) erfc\left(\frac{(2n+x_D)}{2\sqrt{t_D}}\right) \end{array} \right] \end{array} \right\} \\
& + f_y \left\{ \begin{array}{l} \displaystyle\sum_{n=0}^{\infty} 2\sqrt{\frac{C_y t_D}{\pi}} \left[\begin{array}{l} \exp\left(\frac{-(2n+1-y_D)^2}{4t_D}\right) + \exp\left(\frac{-(2n+1+y_D)^2}{4t_D}\right) \\ + \exp\left(\frac{-(2n+2-y_D)^2}{4t_D}\right) + \exp\left(\frac{-(2n+y_D)^2}{4t_D}\right) \end{array} \right] \\ - \left[\begin{array}{l} (2n+1-y_D) erfc\left(\frac{(2n+1-y_D)}{2\sqrt{t_D}}\right) + (2n+1+y_D) erfc\left(\frac{(2n+1+y_D)}{2\sqrt{t_D}}\right) \\ + (2n+2-y_D) erfc\left(\frac{(2n+2-y_D)}{2\sqrt{t_D}}\right) + (2n+y_D) erfc\left(\frac{(2n+y_D)}{2\sqrt{t_D}}\right) \end{array} \right] \end{array} \right\} \\
& + f_z \left\{ \begin{array}{l} \displaystyle\sum_{n=0}^{\infty} 2\sqrt{\frac{C_z t_D}{\pi}} \left[\begin{array}{l} \exp\left(\frac{-(2n+1-z_D)^2}{4t_D}\right) + \exp\left(\frac{-(2n+1+z_D)^2}{4t_D}\right) \\ + \exp\left(\frac{-(2n+2-z_D)^2}{4t_D}\right) + \exp\left(\frac{-(2n+z_D)^2}{4t_D}\right) \end{array} \right] \\ - \left[\begin{array}{l} (2n+1-z_D) erfc\left(\frac{(2n+1-z_D)}{2\sqrt{t_D}}\right) + (2n+1+z_D) erfc\left(\frac{(2n+1+z_D)}{2\sqrt{t_D}}\right) \\ + (2n+2-z_D) erfc\left(\frac{(2n+2-z_D)}{2\sqrt{t_D}}\right) + (2n+z_D) erfc\left(\frac{(2n+z_D)}{2\sqrt{t_D}}\right) \end{array} \right] \end{array} \right\}
\end{aligned}
\tag{51}
$$

$$\sigma_{3D}(t)=\frac{2}{\eta_m}\left(\frac{c_u k_x}{(\phi\mu c_t)L_x^2}\right)\left\{\begin{array}{c}\dfrac{C_x}{\left[\left\{\begin{array}{c}\sum_{n=0}^{\infty}2\sqrt{\dfrac{C_x t_D}{\pi}}\left[\exp(\dfrac{-(2n)^2}{4t_D})+2\exp(\dfrac{-(2n+1)^2}{4t_D})+\exp(\dfrac{-(2n+2)^2}{4t_D})\right]\\ -\left[(2n)erfc(\dfrac{2n}{2\sqrt{t_D}})+2(2n+1)erfc(\dfrac{2n+1}{2\sqrt{t_D}})+(2n+2)erfc(\dfrac{2n+2}{2\sqrt{t_D}})\right]\end{array}\right\}-2C_x t_D\right]}\\ +\\ \dfrac{C_y}{\left[\left\{\begin{array}{c}\sum_{n=0}^{\infty}2\sqrt{\dfrac{C_y t_D}{\pi}}\left[\exp(\dfrac{-(2n)^2}{4t_D})+2\exp(\dfrac{-(2n+1)^2}{4t_D})+\exp(\dfrac{-(2n+2)^2}{4t_D})\right]\\ -\left[(2n)erfc(\dfrac{2n}{2\sqrt{t_D}})+2(2n+1)erfc(\dfrac{2n+1}{2\sqrt{t_D}})+(2n+2)erfc(\dfrac{2n+2}{2\sqrt{t_D}})\right]\end{array}\right\}-2C_y t_D\right]}\\ +\\ \dfrac{C_z}{\left[\left\{\begin{array}{c}\sum_{n=0}^{\infty}2\sqrt{\dfrac{C_z t_D}{\pi}}\left[\exp(\dfrac{-(2n)^2}{4t_D})+2\exp(\dfrac{-(2n+1)^2}{4t_D})+\exp(\dfrac{-(2n+2)^2}{4t_D})\right]\\ -\left[(2n)erfc(\dfrac{2n}{2\sqrt{t_D}})+2(2n+1)erfc(\dfrac{2n+1}{2\sqrt{t_D}})+(2n+2)erfc(\dfrac{2n+2}{2\sqrt{t_D}})\right]\end{array}\right\}-2C_z t_D\right]}\end{array}\right\} \tag{52}$$

For an isotropic case where $k_x = k_y = k_z = k$, $L_x = L_y = L_z = L$ and $q_x = q_y = q_z = q$, time-dependent 3D shape factor becomes:

$$\sigma_{3D}(t)=\frac{6}{L^2}\frac{1}{\left[\left\{\begin{array}{c}\sum_{n=0}^{\infty}2\sqrt{\dfrac{t_D}{\pi}}\left[\exp(\dfrac{-(2n)^2}{4t_D})+2\exp(\dfrac{-(2n+1)^2}{4t_D})+\exp(\dfrac{-(2n+2)^2}{4t_D})\right]\\ -\left[(2n)erfc(\dfrac{2n}{2\sqrt{t_D}})+2(2n+1)erfc(\dfrac{2n+1}{2\sqrt{t_D}})+(2n+2)erfc(\dfrac{2n+2}{2\sqrt{t_D}})\right]\end{array}\right\}-2t_D\right]} \tag{53}$$

After derivation, detailed analysis of time-dependent shape factor is performed for slab (1D), bar (2D) and cube (3D) matrix geometries, where matrix is isotropic with equally spaced fracture for bar and cube. In this respect, in order to cover extreme cases for early and late times, a wide dimensionless time range (1×10^{-10} to 10 with equally spaced 1000 points) is selected. Calculation tolerance is set to 1×10^{-15} to eliminate any round-off errors even for extremely small values such that summation operation is finalized whenever any term in the infinite sum series is less than the given tolerance. Final summation is accepted as analytical solution at the corresponding point.

As shown in **Fig. 4.16**, shape factor is not constant but decreases with time until t_D of 0.1 for all cases. After t_D of 0.1, it becomes constant and becomes $12/L^2$ for 1D-slab matrix (black solid line), $24/L^2$ for 2D-bar matrix (gray solid line) and $36/L^2$ for 3D-cube matrix (dark gray solid line), respectively. Similar observation was pointed out by Chang (1993). As stated previously, our focus is not pseudo-steady state period but transient flow period, which generally covers payout time of a typical fractured well in a shale reservoir. That's why; accurate modeling of this period is crucial for realistic technical and economical assessment. In this regard, two different approximations are tested against exact analytical solution. Instead of adding new terms to summation until reaching to tolerance of 1×10^{-15}, shape factor is calculated based on 1st term approximation (n=0 in Eq. 53) and 2nd term approximation (n=0 and n=1 in Eq. 53). As it can be seen in **Fig. 4.16**, 1st term approximation (dotted lines with same color code) perfectly matches analytical solution in transient flow period for all matrix shapes. However, it starts to deviate from exact solution around t_D of 0.3 at which shape factor is already constant. 2nd term approximation (dashed lines with same color code) is obtained by adding one more term (n=1) to 1st term approximation. It only delays deviation from t_D of 0.3 to t_D of 1. It can be concluded that more terms are needed to achieve required accuracy in shape factor estimation at late time even though shape factor is constant during that period. According to these results, following approximation reported below is suggested to calculate shape factor for 1D-slab matrix geometry. Same formula can be used for isotropic 2D-bar

and 3D-cube matrix shapes as long as they are multiplied by a factor of 2 and 3, respectively.

$$\sigma_{1D}(t)=\begin{cases}\dfrac{1}{L^2}\dfrac{1}{\left[\sqrt{\dfrac{t_D}{\pi}}\left(1+2\exp(-\dfrac{1}{4t_D})+\exp(-\dfrac{1}{t_D})\right)-erfc(\dfrac{1}{2\sqrt{t_D}})-erfc(\dfrac{1}{\sqrt{t_D}})-t_D\right]}, & t_D<0.1\\ \dfrac{12}{L^2}, & t_D\geq 0.1\end{cases} \tag{54}$$

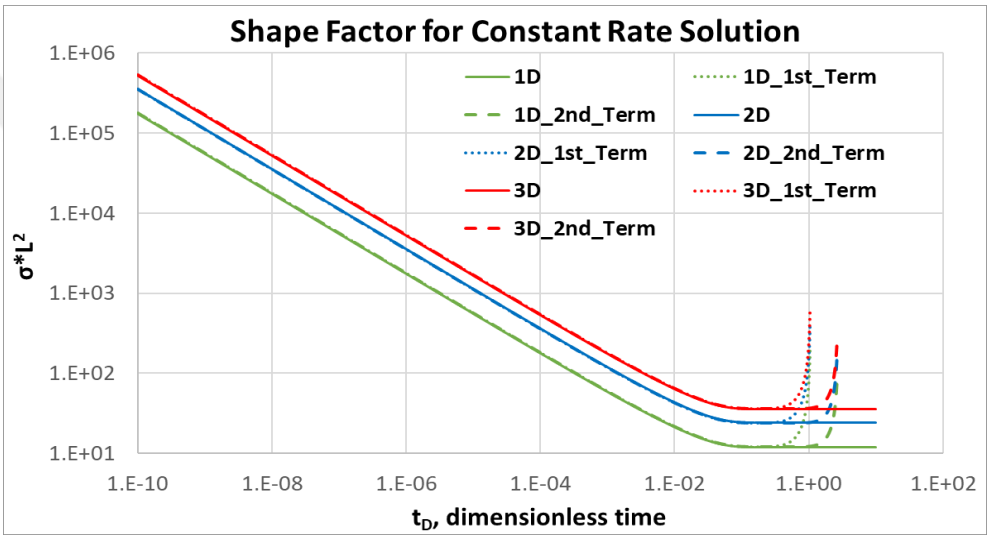

Figure 4.16: Time-dependent shape factor profile for an isotropic rock matrix under constant flux.

4.4.1 Validation

For validation, same numerical models (**Table 4.7**) used in constant fracture pressure case are preferred to test time-dependent shape factor derivation. However, constant shape factor value used in first dual-porosity model is changed from π^2/L^2 to $12/L^2$ to reflect pseudo-steady state flow for this boundary condition. Again, time-dependent shape factor is calculated at each time step based on Eq. 54 by using a script for dual-porosity model and it is overwritten by MULTSIG keyword. Since

boundary condition is constant flux, well production rate is constrained to 0.5 STB/day throughout simulation.

To compare cases under constant rate production constraint, bottom-hole pressure and cumulative water production parameters are used. As it can be seen in **Fig. 4.17**, all cases produce same amount of fluid (dashed lines), which assures accuracy of considered constraint. However, classical dual-porosity formulation with constant shape factor (blue solid line) requires much more depletion in order to produce same amount of fluid compared to fine-scale single porosity model (green solid line). The underlying reason for this behavior is that shape factor based on pseudo-steady state flow condition is much lower than its actual value in shale reservoirs. It means that flow contribution from matrix to fracture is underestimated. As a matter of fact, additional depletion is needed to satisfy constant rate constraint in simulation. Maximum difference observed between single-porosity model and 1st dual-porosity model in bottom-hole pressures is 1,711 psi while average one is 471 psi within 5 years simulation run. On the other hand, mismatch is removed by using time-dependent shape factor in 2nd dual-porosity model (red solid line) and pressure profile is same with single-porosity model.

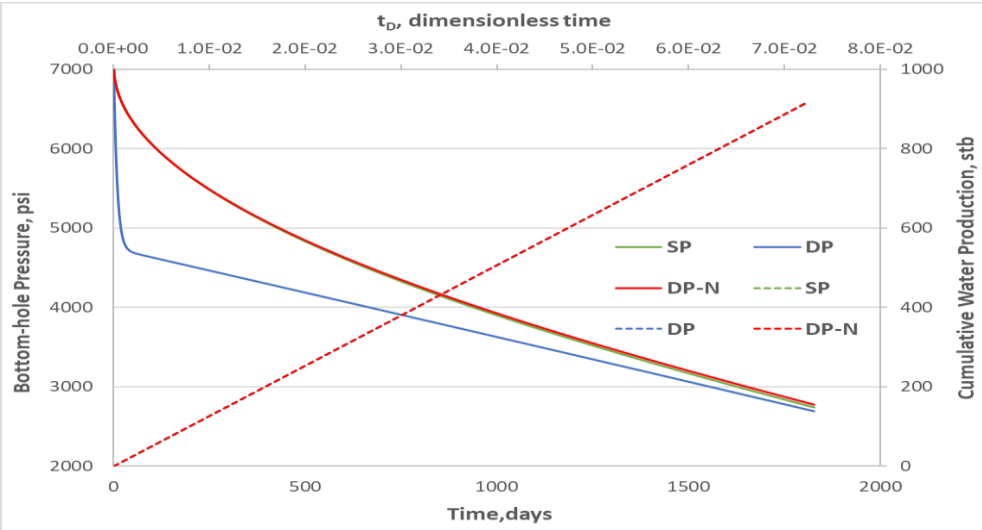

Figure 4.17: Comparison of dual-porosity models with single-porosity solution in bottom-hole pressure and cumulative water production.

Such a significant error in bottom-hole pressure occurs only for 0.5 STB/day of production. Obviously, it becomes significantly larger as the withdrawal is larger. Modifying other reservoir parameters to match well performance could be another option to compensate this fundamental error in existing dual-porosity models. However, such approach adversely affects both technical and commercial assessment of the field.

4.5 Constant Fracture Pressure Followed by Linearly Declining Fracture Pressure Boundary Condition

For considered problem in anisotropic matrix medium with a single-phase slightly compressible fluid, PDE, IC and BCs are defined in Eq. 55, Eq. 56 and Eq. 57, respectively.

$$c_u k_x \frac{\partial^2 P}{\partial x^2} + c_u k_y \frac{\partial^2 P}{\partial y^2} + c_u k_z \frac{\partial^2 P}{\partial z^2} = (\phi \mu c_t) \frac{\partial P}{\partial t} \qquad \begin{matrix} 0 \le x \le L_x \\ 0 \le y \le L_y \\ 0 \le z \le L_z \end{matrix} \tag{55}$$

$$P(x, y, z, t = 0) = P_i \tag{56}$$

$$P \begin{bmatrix} x = 0 \ \& \ x = L_x, t \\ y = 0 \ \& \ y = L_y, t \\ z = 0 \ \& \ z = L_z, t \end{bmatrix} = \begin{Bmatrix} P_f & t \le t_s \\ P_f - K(t - t_s) & t > t_s \end{Bmatrix} \tag{57}$$

where K is decline coefficient of fracture pressure (P/T or M/L×T^3) and t_s is switching time (T) from constant fracture pressure to linearly declining fracture pressure. Using dimensionless parameters defined in Eq. 44 yields same PDE in Eq. 45 with same coefficients in Eq. 46. IC and BCs for this problem becomes:

$$P_D(x_D, y_{D,} z_D, t_D) = 0 \quad @ t_D = 0 \tag{58}$$

$$P_D\begin{bmatrix} x_D=0 \ \& \ x_D=1, t_D \\ y_D=0 \ \& \ y_D=1, t_D \\ z_D=0 \ \& \ z_D=1, t_D \end{bmatrix}=\begin{Bmatrix} 1 & t_D \le t_{Ds} \\ 1+\dfrac{K(t_D-t_{Ds})}{\Delta P_0 \dfrac{\eta_x}{L_x^2}} & t_D > t_{Ds} \end{Bmatrix} \tag{59}$$

As seen from the BCs given above, this problem can be treated as superimposed version of two distinct problems. Therefore, it can be written as summation of those, where one of them is time-dependent problem. Definitions of these sub-problems are arranged such that they should be easy to solve as much as possible. In this respect, two new PDEs are constructed based on Eq. 60 in below. Also, new dimensionless pressure definition shown in Eq. 61 is used to find IC and BCs of sub-problems.

$$P_D = 1-(P_{DH}+P_{DT}) \tag{60}$$

$$P_{DH} = P_{DT} = \frac{P_f - P}{P_f - P_i} \tag{61}$$

where P_{DH} is dimensionless pressure for homogeneous problem while P_{DT} is dimensionless pressure for time-dependent problem. Their final versions including IC and BCs become:

$$PDE: \quad C_x \frac{\partial^2 P_{DH}}{\partial {x_D}^2} + C_y \frac{\partial^2 P_{DH}}{\partial {y_D}^2} + C_z \frac{\partial^2 P_{DH}}{\partial {z_D}^2} = \frac{\partial P_{DH}}{\partial t_D} \tag{62}$$

$$IC: \quad P_{DH}(x_D, y_D, z_D, 0) = 1 \tag{63}$$

$$BCs: \quad P_{DH}(boundaries, t_D) = 0 \tag{64}$$

$$PDE: \quad C_x \frac{\partial^2 P_{DT}}{\partial {x_D}^2} + C_y \frac{\partial^2 P_{DT}}{\partial {y_D}^2} + C_z \frac{\partial^2 P_{DT}}{\partial {z_D}^2} = \frac{\partial P_{DT}}{\partial t_D} \tag{65}$$

$$IC: \quad P_{DT}(x_D, y_D, z_D, 0) = 0 \tag{66}$$

$$BCs: \quad \begin{cases} P_{DT}(boundaries, t_D) = 0 & t_D \le t_{Ds} \\ P_{DT}(boundaries, t_D) = -\dfrac{K(t_D - t_{Ds})}{\Delta P_0 \dfrac{\eta_x}{L_x^2}} & t_D > t_{Ds} \end{cases} \tag{67}$$

Verifications to original problem can be carried out by summing PDE, IC and BCs of two separate problems based on Eq. 60 and comparing those with Eq. 58 and Eq. 59. The first problem called homogeneous problem due its boundary conditions is already solved in previous section as:

$$P_{DH}(x_D, y_D, z_D, t_D) = \frac{64}{\pi^3} \sum_{n=0}^{\infty} \sum_{m=0}^{\infty} \sum_{k=0}^{\infty} \frac{\exp\left\{-\left[(2n+1)^2 C_x + (2m+1)^2 C_y + (2k+1)^2 C_z\right]\pi^2 t_D\right\}}{(2n+1)(2m+1)(2k+1)} \times \sin\left[(2n+1)\pi x_D\right] \sin\left[(2m+1)\pi x_D\right] \sin\left[(2k+1)\pi x_D\right] \tag{68}$$

As seen in Eq. 66 and in Eq. 67, P_{DT} is simply zero from beginning to switching time. Once time exceeds that point, BCs are neither zero nor constant. To solve PDE with time-dependent boundary conditions, Duhamel's theorem is implemented. Solution strategy is forming an auxiliary problem where initial condition is zero while boundary conditions are unity. Once auxiliary problem is solved, time-dependent dimensionless solution is obtained from Duhamel's superposition integral as (derivation details are provided in Appendix-C):

$$P_{DT}(x_D, y_D, z_D, t_D) = -\left(\frac{K}{\Delta P_0 \dfrac{\eta_x}{L_x^2}} (t_D - t_{Ds}) \right) - \left(\frac{K}{\Delta P_0 \dfrac{\eta_x}{L_x^2}} \frac{64}{\pi^3} \sum_{n=0}^{\infty} \sum_{m=0}^{\infty} \sum_{k=0}^{\infty} \frac{\exp\left\{-\left[(2n+1)^2 C_x + (2m+1)^2 C_y + (2k+1)^2 C_z\right]\pi^2 (t_D - t_{Ds})\right\} - 1}{\left[(2n+1)^2 C_x + (2m+1)^2 C_y + (2k+1)^2 C_z\right]\pi^2 (2n+1)(2m+1)(2k+1)} \times \sin\left[(2n+1)\pi x_D\right] \sin\left[(2m+1)\pi x_D\right] \sin\left[(2k+1)\pi x_D\right] \right) \tag{69}$$

By using Eq. 60, final form of the dimensionless pressure solution for a 3D anisotropic matrix is:

$$P_D(x_D, y_D, z_D, t_D) = 1 - \left(\frac{64}{\pi^3} \sum_{n=0}^{\infty} \sum_{m=0}^{\infty} \sum_{k=0}^{\infty} \frac{\exp\left\{ -\left[(2n+1)^2 C_x + (2m+1)^2 C_y + (2k+1)^2 C_z \right] \pi^2 t_D \right\}}{(2n+1)(2m+1)(2k+1)} \times \sin\left[(2n+1)\pi x_D \right] \sin\left[(2m+1)\pi x_D \right] \sin\left[(2k+1)\pi x_D \right] \right)$$

$$+ \left(\frac{K}{\Delta P_0 \frac{\eta_x}{L_x^2}} (t_D - t_{Ds}) \right)$$

$$+ \left(\frac{K}{\Delta P_0 \frac{\eta_x}{L_x^2}} \frac{64}{\pi^3} \sum_{n=0}^{\infty} \sum_{m=0}^{\infty} \sum_{k=0}^{\infty} \frac{\exp\left\{ -\left[(2n+1)^2 C_x + (2m+1)^2 C_y + (2k+1)^2 C_z \right] \pi^2 (t_D - t_{Ds}) \right\} - 1}{\left[(2n+1)^2 C_x + (2m+1)^2 C_y + (2k+1)^2 C_z \right] \pi^2 (2n+1)(2m+1)(2k+1)} \times \sin\left[(2n+1)\pi x_D \right] \sin\left[(2m+1)\pi x_D \right] \sin\left[(2k+1)\pi x_D \right] \right)$$

(70)

Time-dependent shape factor is calculated from Eq. 21 as:

$$\sigma_{3D}(t) = \frac{1}{\eta_m} \frac{\eta_x}{L_x^2} \pi^2 \frac{\sum_{n=0}^{\infty} \sum_{m=0}^{\infty} \sum_{k=0}^{\infty} \frac{\left[\begin{array}{l} \left[(2n+1)^2 C_x + (2m+1)^2 C_y + (2k+1)^2 C_z \right] \frac{\eta_x}{L_x^2} \pi^2 \times \\ \exp\left\{ -\left[(2n+1)^2 C_x + (2m+1)^2 C_y + (2k+1)^2 C_z \right] \pi^2 t_D \right\} \\ -\frac{K}{\Delta P_0} (\exp\left\{ -\left[(2n+1)^2 C_x + (2m+1)^2 C_y + (2k+1)^2 C_z \right] \pi^2 (t_D - t_{Ds}) \right\} - 1) \end{array} \right]}{(2n+1)^2 (2m+1)^2 (2k+1)^2}}{\sum_{n=0}^{\infty} \sum_{m=0}^{\infty} \sum_{k=0}^{\infty} \frac{\left[\begin{array}{l} \left[(2n+1)^2 C_x + (2m+1)^2 C_y + (2k+1)^2 C_z \right] \frac{\eta_x}{L_x^2} \pi^2 \times \\ \exp\left\{ -\left[(2n+1)^2 C_x + (2m+1)^2 C_y + (2k+1)^2 C_z \right] \pi^2 t_D \right\} \\ -\frac{K}{\Delta P_0} (\exp\left\{ -\left[(2n+1)^2 C_x + (2m+1)^2 C_y + (2k+1)^2 C_z \right] \pi^2 (t_D - t_{Ds}) \right\} - 1) \end{array} \right]}{\left[(2n+1)^2 C_x + (2m+1)^2 C_y + (2k+1)^2 C_z \right] (2n+1)^2 (2m+1)^2 (2k+1)^2}}$$

(71)

For an isotropic case where $k_x = k_y = k_z = k$ and $L_x = L_y = L_z = L$, time-dependent 3D shape factor is:

$$\sigma_{3D}(t)=\frac{\pi^2}{L^2}\frac{\sum_{n=0}^{\infty}\sum_{m=0}^{\infty}\sum_{k=0}^{\infty}\frac{\left[\begin{array}{l}\left[(2n+1)^2+(2m+1)^2+(2k+1)^2\right]\pi^2\times\exp\left\{-\left[(2n+1)^2+(2m+1)^2+(2k+1)^2\right]\pi^2 t_D\right\}\\ -\frac{K}{\Delta P_0}\frac{L^2}{\eta_m}(\exp\left\{-\left[(2n+1)^2+(2m+1)^2+(2k+1)^2\right]\pi^2(t_D-t_{Ds})\right\}-1)\end{array}\right]}{(2n+1)^2(2m+1)^2(2k+1)^2}}{\sum_{n=0}^{\infty}\sum_{m=0}^{\infty}\sum_{k=0}^{\infty}\frac{\left[\begin{array}{l}\left[(2n+1)^2+(2m+1)^2+(2k+1)^2\right]\pi^2\times\exp\left\{-\left[(2n+1)^2+(2m+1)^2+(2k+1)^2\right]\pi^2 t_D\right\}\\ -\frac{K}{\Delta P_0}\frac{L^2}{\eta_m}(\exp\left\{-\left[(2n+1)^2+(2m+1)^2+(2k+1)^2\right]\pi^2(t_D-t_{Ds})\right\}-1)\end{array}\right]}{\left[(2n+1)^2+(2m+1)^2+(2k+1)^2\right](2n+1)^2(2m+1)^2(2k+1)^2}} \tag{72}$$

Contrary to constant rate boundary condition, achieving desired tolerance of 1×10^{-15} in infinite sum series within reasonable computational time is not possible for time-dependent shape factor of constant fracture pressure followed by linearly declining fracture pressure case, especially for 2D and 3D matrix geometries. Calculating 3D shape factors corresponding to 16 dimensionless time values takes almost 15 days on a 32 gb ram PC with 3.60 GHz of I9 processor, where calculation tolerance is only set to 1×10^{-5}. In this respect, dimensionless time (t_D) range is narrowed such that it starts from 1×10^{-5} to 10 in order to eliminate convergence problems observed in too small t_D values. To keep computation time at reasonable level, tolerance in summation terms is determined as 1×10^{-15}, 1×10^{-6} and 1×10^{-5} for 1D-slab, 2D-bar and 3D-cube matrix shapes, respectively. Finally, flow control terms in Eq. 67 are selected as K=1 psi/day, ΔP_0=dP=10 psi, t_D/t=η_m/L^2=1E-10 day^{-1} and t_{Ds}=0.

Based on parameters above, calculated shape factors are plotted as seen in **Fig. 4.18**. Similar to constant pressure and constant rate solutions, shape factor decreases with time until t_D of 0.1. Once t_D exceeds 0.1, it is no longer time-dependent rather it becomes constant during late time or pseudo-steady state flow, as expected. For a 1D-slab matrix (green color), constant shape factor is found as $12/L^2$, same value was also reported by Chang (1993). On the other hand, $28.4/L^2$ and $49.5/L^2$ are calculated for 2D-bar (blue) and 3D-cube (red) matrix cases, respectively. As opposed to constant pressure and constant rate solutions, proportionality of shape factor with respect to matrix dimension is not observed. In other words, 2D and 3D

cases do not converge to values of $24/L^2$ and $36/L^2$, respectively. This unexpected result can be attributed to complex form of infinite sum series. Lack of precise tolerance could be considered another reason but its effect on late time calculation is limited. Increasing tolerance does not reduce difference between $49.5/L^2$ and $36/L^2$, rather it increases very slightly.

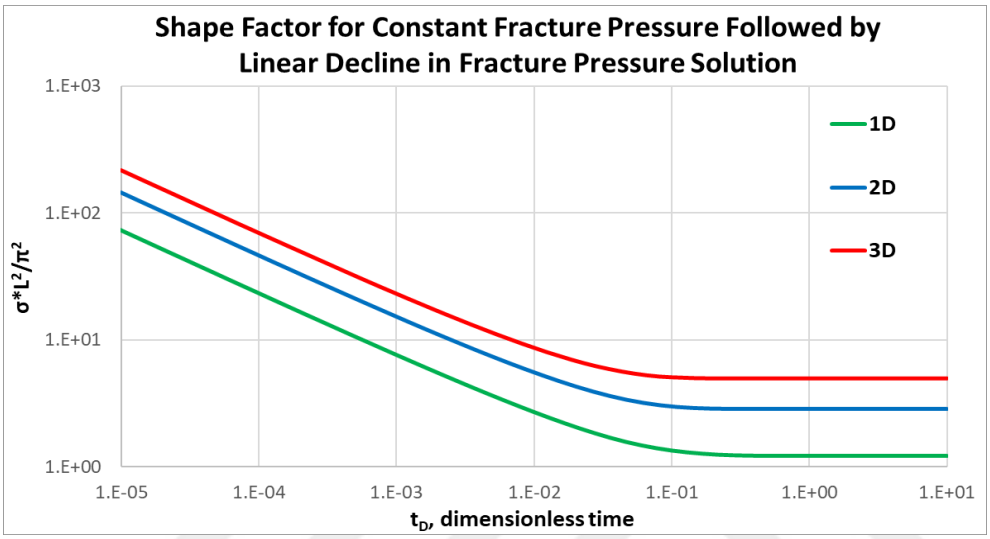

Figure 4.18: Time-dependent shape factor profile for an isotropic rock matrix under constant fracture pressure followed by linearly declining fracture pressure.

Since high accuracy calculation of shape factor with a tolerance of 1×10^{-15} is achieved in 1D matrix shape, sensitivity analysis is conducted on flow control parameters mentioned above for this case. First parameter to be tested is switching time. As illustrated in **Fig. 4.19**, shape factor is calculated for three switching times. If fracture pressure starts to decline linearly at the beginning (black dashed line), shape factor deviates from constant pressure solution (blue line) immediately and follows its own trend until converging to constant rate solution (red line) at late time. On the contrary, shape factor is aligned with constant pressure solution before switching times of $t_{Ds}=1\times10^{-6}$ (yellow dashed line) and $t_{Ds}=1\times10^{-2}$ (green dashed line), as expected. After initial spikes to higher values at these points, shape factor lines up its particular trend. Ultimately, they converge to constant rate solution at late time, where shape factor is almost constant.

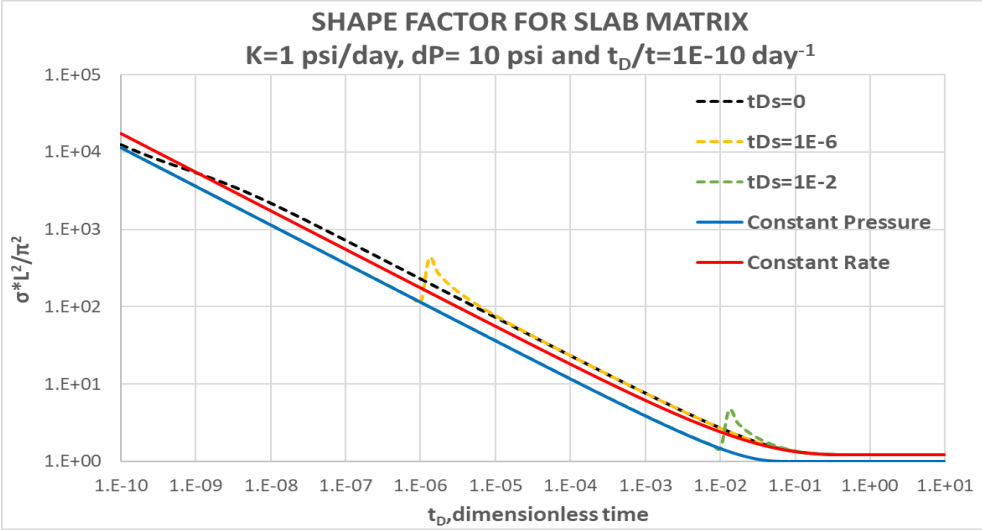

Figure 4.19: Effect of switching time on time-dependent shape factor behavior.

Second analysis focuses on both t_D/t (η_m/L^2), which is an amalgamated reservoir-completion property and dP (ΔP_0), which is an operational property. Not only their individual effects on shape factor but also their combined effects are investigated. In this respect, t_{Ds} is selected as zero for all cases in order to amplify their sensitiveness while K is kept as 1 psi/day.

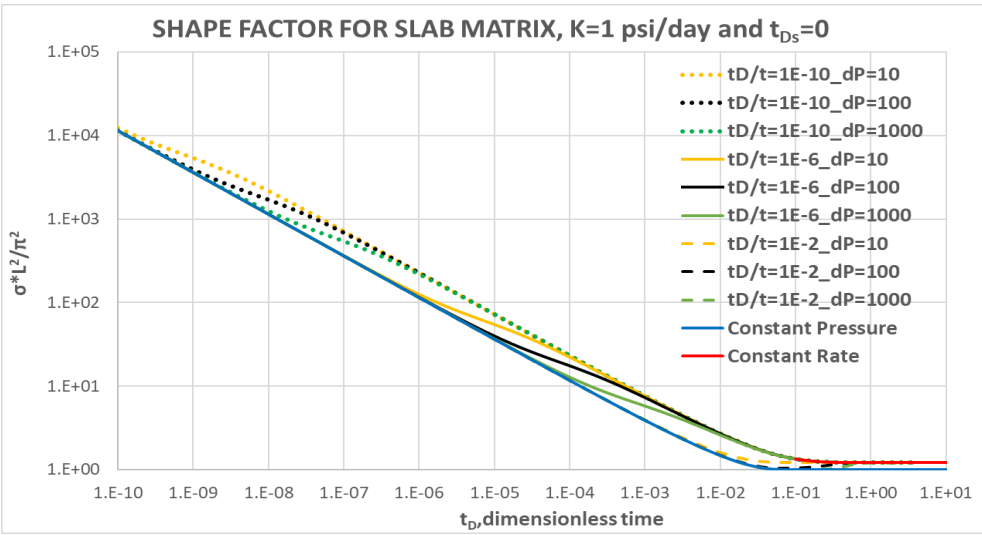

Figure 4.20: Effect of t_D/t and dP parameters on time-dependent shape factor behavior.

It is shown in **Fig. 4.20** that higher initial drawdown pressure or dP (yellow, black and green colors, respectively) prolongs constant pressure behavior in shape factor profile, regardless of t_D/tvalue. Same observation is also obvious for increase in t_D/t parameter (dotted, solid and dashed lines, respectively). From physical perspective, effect of linear decline in fracture pressure on shape factor profile is masked in a shale reservoir with better rock quality or denser fracture sets. If t_D/t value is large, shape factor profiles for different initial drawdown pressures (yellow, black and green dashed lines, respectively) are very similar. Finally, shape factor becomes constant around t_D of 0.1 as in the case of constant rate solution illustrated by red solid line (whole profile is limited because it hinders other ones).

Last analysis is performed with operational parameters of K and dP. Again, linear decline in fracture pressure is started immediately to allow their effects on shape factor under this boundary condition much more recognizable. In order to extend transient flow period, t_D/t is chosen as 1×10^{-10} day^{-1}.

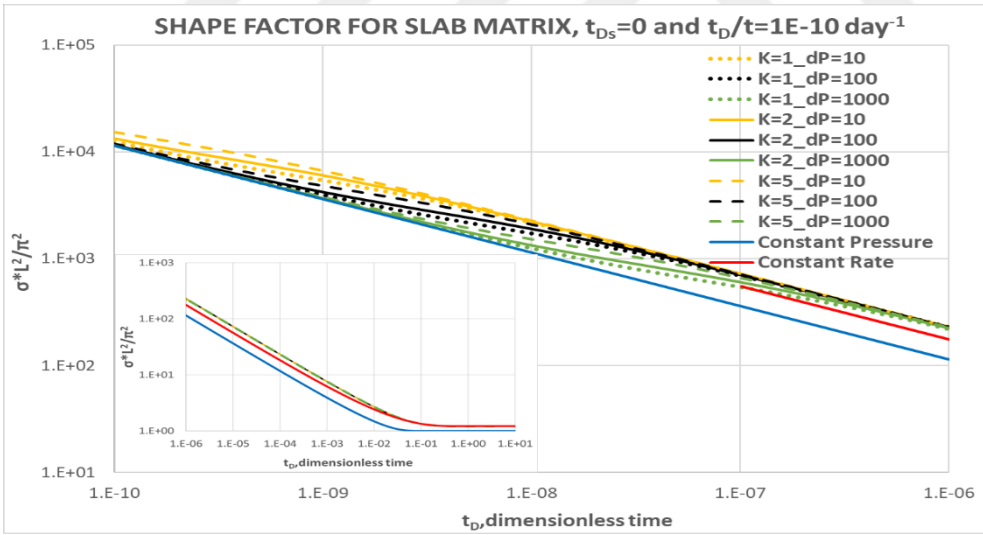

Figure 4.21: Effect of K and dP parameters on time-dependent shape factor behavior.

As it can be seen in **Fig. 4.21**, increasing initial drawdown pressure (dP) results in longer duration of constant pressure trend in shape factor profile (blue line) irrespective of K (yellow, black and green colors, respectively). As decline in

fracture pressure accelerates, deviation in shape factor profile from constant pressure solution begins earlier (dotted, solid and dashed lines, respectively). Shape factors for considered cases are unified at t_D of 1×10^{-6} and they keep decreasing according to their distinctive trend until reaching to value of $12/L^2$. This terminal value is exactly same for constant rate solution (red line). In other words, shape factor behaves same at late time for both boundary conditions.

4.5.1 Validation

In validation of provided solution, aforementioned numerical model for constant rate boundary condition is used. To adopt it, switching time is started from the beginning (t_{Ds}=0) while initial drawdown pressure is assumed as 2,000 psi (P_{f0}= 5,000 psi). Decline coefficient of K is selected as 1 psi/day such that 1 psi reduction occurs in bottom-hole pressure at each day. The t_D/t value can be calculated as $3.95\text{x}10^{-5}$ from data provided in **Table 4.7**. After constructing single-porosity model, three different dual-porosity models are built for comparison. First dual-porosity model has constant shape factor of π^2/L^2, which corresponds to late time approximation of constant fracture pressure solution. Its constant rate version is represented by 2nd dual-porosity model where shape factor is $12/L^2$. On the other hand, 3rd model uses time-dependent shape factors calculated from Eq. C-37, instead of constant value.

Their behaviors in terms of mean matrix pressure and cumulative water production are depicted in **Fig. 4.22** by solid lines and dashed lines with same colors, respectively. Both 1st (blue color) and 2nd (red color) dual-porosity models are not able to replicate neither mean matrix pressure nor cumulative water production of single-porosity model (green color). Since 1st model has lower shape factor value than 2nd one (π^2/L^2 vs. $12/L^2$), underestimation in fluid transfer from matrix to fracture is bigger. Associated errors in cumulative water production are %19.6 and %8 while they become %7.7 and %3.2 in final mean matrix pressure, respectively. On the contrary, 3rd dual-porosity model with time-dependent shape factor (yellow color) exhibits same behaviors in both parameters, which validates our derivation.

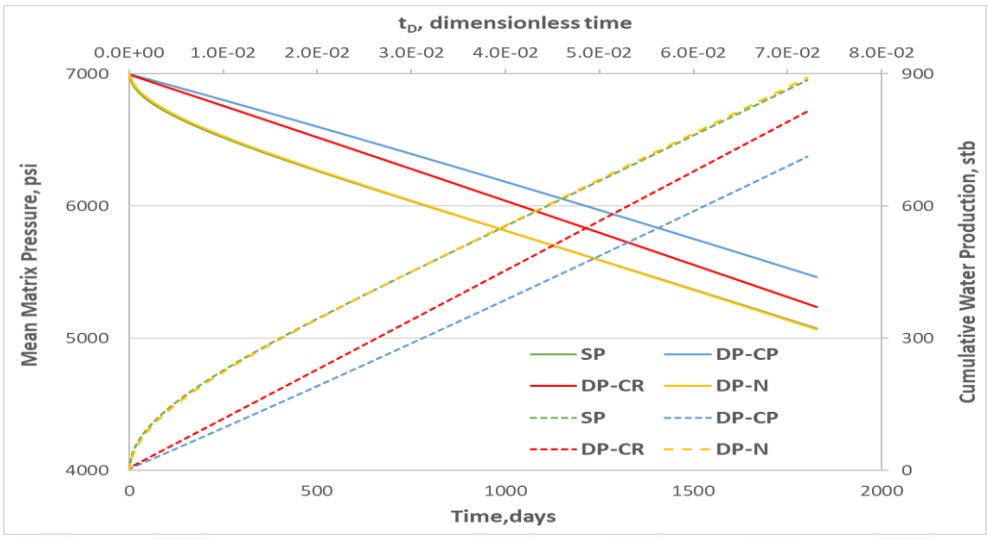

Figure 4.22: Comparison of dual-porosity models with single-porosity solution in mean matrix pressure.

CHAPTER 5

DECLINE CURVE ANALYSIS

As mentioned in literature review section, decline curve analysis is another commonly used technique for performance prediction of wells. This chapter analyzes effect of long transient flow period in fractured shale reservoirs on decline curve analysis, specifically with Arps hyperbolic decline model. In this respect, behavior of hyperbolic decline parameter (***b*** exponent) is assessed by transient dual-porosity model for accuracy. The ***b*** exponent obtained from exact solution is compared with those obtained from new empirical function discussed in previous section. Sensitivity analyses are conducted using different set of reservoir models to show the uses and the accuracy of the proposed method.

5.1 Methodology

Initial step of the study is setting up a benchmark model, which must be capable of modeling transient flow accurately. Another concern is simplicity with respect to run time and sensitivity analysis. In this respect, semi-analytical transient dual-porosity model is chosen as a mechanistic model. In order to assure its accuracy, it is validated by fine-scale single porosity numerical reservoir model.

Well production from this model is used to calculate ***b*** exponent in Arps hyperbolic decline model according to formula (initially defined as derivative of loss-ratio by Johnson and Bollens (1927)) given below:

$$\boldsymbol{b}\text{ exponent} = b(t) = \frac{d}{dt}\left[\frac{1}{D(t)}\right] = \frac{d}{dt}\left[\frac{-q(t)}{dq(t)/dt}\right] \tag{73}$$

Two other alternative ***b*** exponent calculations are obtained from inter-porosity flow term. The first one uses exact analytical pressure solution while second one is calculated from empirical function proposed in previous chapter. In order to test their

performance in predicting of ***b*** exponent behavior, sensitivity analysis is conducted on both matrix and fracture properties. Finally, results are compared for three different ***b*** exponent calculations. **Fig 5.1** summarizes workflow followed in this chapter.

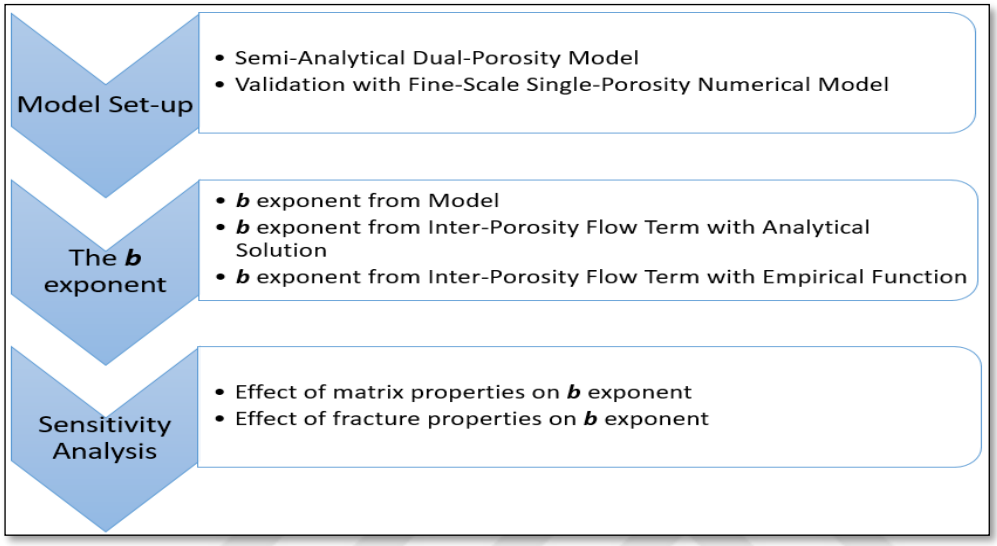

Figure 5.1: Workflow followed in ***b*** exponent analysis

5.2 Mechanistic Model

The planar form of hydraulic fractures perpendicular to minimum horizontal stress was confirmed by Distributed Acoustic Sensor for Strain Fronts (DAS-SF) measurements in the Groundbirch Montney in Canada (Ugueto et al. (2019)). It has been shown that planar fracture propagates within a relatively narrow corridor called "Frac-Zone-Domain", which questions development of enhanced permeability region nearby planar fracture. From pressure monitoring outside of the offset well in Eagle Ford, Raterman et al. (2019) concluded that not all hydraulic fracture strands contribute flow but only few major fracture strands are associated with depletion, resulting a patchy type rock drained volume. Along with other observations, planar fracture modeling approach was suggested by McClure et al. (2020). It has been also

claimed that natural fractures can be treated as a bulk property in continuum modeling, because of their small sizes and abundances.

For the sake of simplicity, mechanistic model is selected as transient dual-porosity model presented by El-Banbi (1998) and Bello (2009) consisting of hydraulic fracture and tight rock matrix. Reservoir has a rectangular geometry, where planar fracture extends to reservoir boundary. This slab matrix geometry with homogeneous reservoir properties assures long term linear flow, commonly seen in unconventional wells. Since the derived solutions are in Laplace domain, numerical inversion is carried out by using well known Stefhest algorithm.

Validation of the semi-analytical model is conducted using a commercial black-oil simulator for single porosity model mentioned in Chapter 4.1, where well is controlled by constant bottom-hole pressure to reflect high drawdown operating strategy in unconventional wells. As illustrated in **Fig. 5.2**, production rate from semi-analytical solution (dashed red line) is in accord with the one from single-porosity model (dashed green line) except for very early times at which early fracture depletion occurs. The mismatch might arise from the use of small real time corresponding to large $\boldsymbol{s}$ value in Laplace domain such that numerical inversion might have some errors. Since early time period is too short and generally not seen in these wells, semi-analytical model can be confidently used in sensitivity analysis. As a supporting fact, log-log plot clearly shows matrix linear flow. One interesting observation is that $\boldsymbol{b}$ exponent calculated from numerical simulation exhibits some oscillatory behavior similar to those reported by Tugan and Weijermars (2020). On the other hand, dense logarithmic time stepping in Laplace solution results in much narrowed $\boldsymbol{b}$ exponent behavior. This is another advantage of the proposed model during sensitivity analysis in terms of identifying $\boldsymbol{b}$ exponent response to corresponding reservoir parameter.

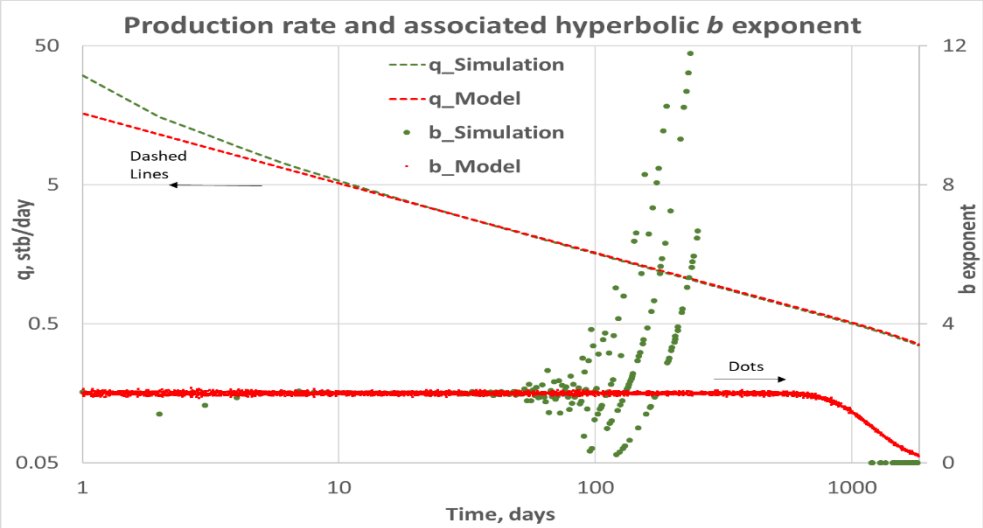

Figure 5.2: Comparison of semi-analytical transient dual-porosity model with fine-scale reservoir simulation.

5.3 New Empirical Function

In shale reservoirs, hydraulic fracturing is used as a stimulation technique to reach economical flow rates. As opposed to conventional fractured reservoirs, produced oil and gas comes only from the rock matrix. Artificially created fractures only deliver what it gets from matrix to the wellbore. Therefore, matrix-fracture transfer rate can be representative in understanding actual production behavior of the well. In this respect, inter-porosity flow term can be calculated by using Eq. 74 with known reservoir properties, drawdown pressure and dimensionless mean matrix pressure. Both exact analytical solution of mean matrix pressure (Eq. 75) and proposed empirical function (Eq. 76) are used to estimate inter-porosity flow. Then, hyperbolic ***b*** exponent from inter-porosity flow term is calculated for both approaches and then compared to those obtained from actual well flow rates.

$$\hat{q} = -(\phi c_t)_m \frac{\partial \overline{P_m}}{\partial t} = -(\phi c_t)_m \frac{\partial (P_i - \Delta P_w \overline{P_D})}{\partial t} = (\phi c_t)_m \Delta P_w \frac{\partial \overline{P_D}}{\partial t} \qquad (74)$$

$$\bar{P}_D = \frac{\overline{P_m} - P_i}{P_f - P_i} = 1 - \frac{8}{\pi^2} \sum_{n=0}^{\infty} \frac{exp[-\pi^2 t_D (2n+1)^2]}{(2n+1)^2} \qquad (75)$$

$$\bar{P}_D = \frac{\overline{P_m} - P_i}{P_f - P_i} = \sqrt{tanh(\pi^2 t_D/2)} \quad (76)$$

$$t_D = \frac{c_u k_m t}{(\phi c_t)_m \mu} \frac{1}{L^2} \quad (77)$$

where $\hat{q}$ is the volumetric flux per unit time per unit total rock volume ($L^3/L^3 \times T$) and ΔP_w is the drawdown pressure of well intersecting with highly conductive fracture.

5.4 Sensitivity Analysis

Commonly used experimental setups and corresponding procedures to measure reservoir rock properties are developed for conventional rocks. In addition, accuracy limits of equipment used to obtain reservoir rock properties are not aligned with tight rock properties. Accurate measurement of key reservoir parameters like permeability and rock compressibility is extremely difficult in such formations. As a consequence, widely changing values are reported in the literature for the same reservoir property in the same formation. In addition to those, most of the completion parameters are uncertain. Even though measurement tools such as micro-seismic and distributed acoustic sensors provide some useful information, fracture geometry is usually not available. Several studies used simple 2D crack models developed at early 60's while others preferred to use sophisticated 3D models with advanced functionalities like coupling rock mechanics with fluid and heat flow. In addition to fracture geometry, production contribution of each created fracture is not known. Furthermore, as highlighted by Weijers et al. (2019) fracking technology and its application has changed over the years. For example, early drilled wells are shorter in lateral length with small number of frac stages while newer wells are laterally longer with higher frac stage counts aiming denser fractures. Last but not least, amount of injected water and proppant per stage have increased. Due to these reasons, base model construction with representative parameters is challenging. In this respect, model parameters reported in the literature are averaged to a certain extent while others are assumed. Sensitivity analysis is conducted on parameters, which have higher uncertainties.

Selected parameters are fracture half-length, fracture spacing, fracture conductivity, matrix permeability, matrix porosity, matrix rock compressibility and fracture rock compressibility. A range with reasonable limits is assigned to test modeling capabilities of the proposed models. Economic well life is assumed as 25 years. **Table 5.1** summarizes model properties used in sensitivity analysis and associated references.

Table 5.1: Semi-analytical model parameters

Parameter	Lowest	Lower	Base Case	Higher	Highest	References
Fracture half-length, ft	100	200	300	400	500	Mayerhofer et al. (2017) Raterman et al. (2019)
Fracture spacing, ft	80	160	200	300	400	Weijers et al. (2019) Ugueto et al. (2019)
Fracture conductivity, md-ft	0.5	5	50	100	500	Shahvali et al. (2016) Mayerhofer et al. (2017)
Fracture Aperture, ft	0.01					Rubin (2010) Ciezobka and Reeves (2020)
Matrix Permeability, md	1.E-05	1.E-04	2.E-04	5.E-04	1.E-03	Bhandari et al. (2018) McClure et al. (2020)
Matrix Porosity, fraction	0.04	0.06	0.08	0.1	0.12	Weijermars et al. (2017) Bhandari et al. (2018)
Matrix Rock Compressibility, psi^{-1}	1E-07	1E-06	1E-05	1E-04	5E-04	Kurtuoglu (2013) Davudov et al. (2018)
Fracture Rock Compressibility, psi^{-1}	1E-06	1E-05	1E-04	1E-03	5E-03	
Fluid Compressibility, psi^{-1}	1.35E-5					Assumed
Fluid FVF, rbbl/stb	1					Assumed
Fluid Viscosity, cp	0.7					Assumed
Formation Thickness, ft	150					Kennedy et al. (2016)
Initial Pressure, psi	7500					Weijermars et al. (2017) Gherabati (2018)
Bottom-hole Pressure, psi	1000					Assumed

By using semi-analytical model, five different scenarios for each individual parameter are studied. Model outputs are used to compute instantaneous hyperbolic ***b*** exponent. In order to observe model responses, flow rate and associated ***b*** exponent are plotted against dimensionless time (t_D) which can be obtained from Eq. 77. Since start value of t_D is different for each case, 1×10^{-4} is selected as a starting point in plotting. After that, Eq. 74 is used to estimate inter-porosity flow term where dimensionless pressure is taken from Eq. 75 for analytical solution and Eq. 76 for proposed empirical function, respectively. Finally, ***b*** exponents from inter-porosity flow terms are calculated. Legends on the plots are arranged such that red color shows low value while purple one refers to high value for the corresponding parameter. Dots with same color code are used to plot ***b*** exponent for semi-analytical solution. Also, analytically obtained ***b*** exponent is represented by solid line while dashed line shows empirical one.

5.4.1 Matrix Permeability

As illustrated in **Fig. 5.3**, tighter matrix leads to longer duration of formation linear flow characterized by negative half slope in log-log flow rate versus time plot. The ***b*** exponent is equal to 2 during this period, which was mathematically shown by Spivey et al. (2001) based on flow rate-time$^{-1/2}$ (q vs. t$^{-1/2}$) relation.

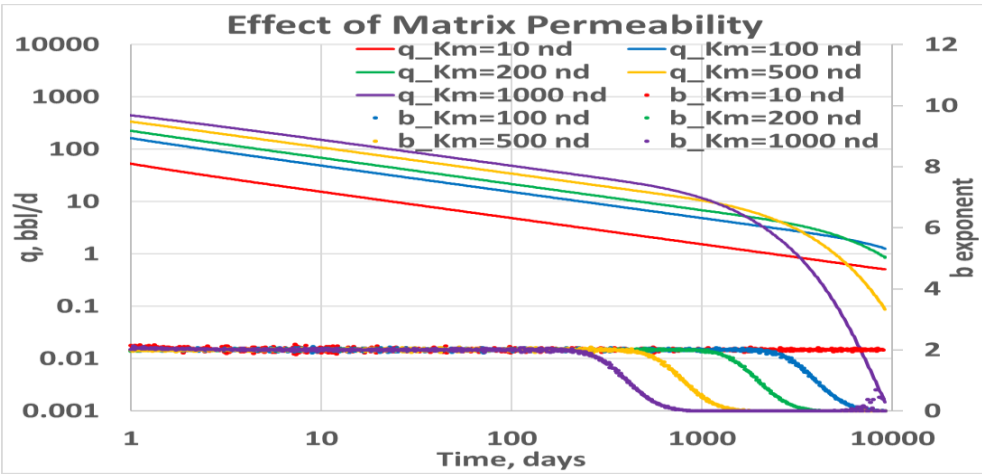

Figure 5.3: Sensitivity analysis for matrix permeability.

Plotting flow rate versus dimensionless time (**Fig. 5.4**) reveals that ***b*** exponent starts to deviate from 2 for t_D values larger than 0.02. At a t_D of 0.1, ***b*** exponent becomes zero indicating boundary-dominated flow. In between 0.02 and 0.1, transition from matrix linear flow to boundary-dominated flow is observed as a sigmoidal curve. These values are different than those presented by Fulford and Blasingame (2013) such that in their study, 0.1 and 0.7 were found as end of linear flow and beginning of boundary-dominated flow, respectively. When two studies are compared, it can be observed that flow regimes are established at later times. This observation is related to gas phase such that its compressibility leads to extension of flow regimes.

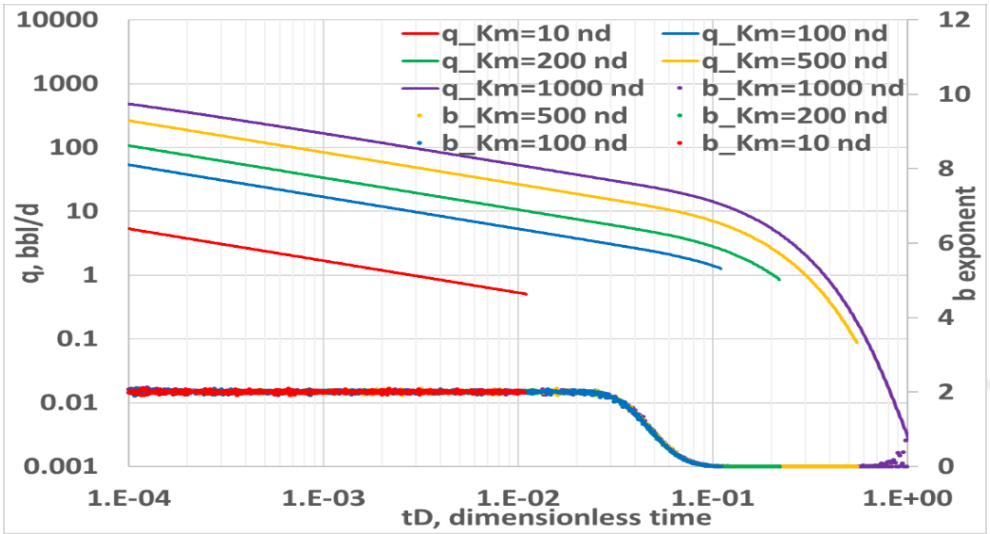

Figure 5.4: The q vs. ***b*** exponent behavior in dimensionless time for matrix permeability.

In **Fig. 5.5**, ***b*** exponent obtained from inter-porosity flow term is compared with model result. The ***b*** exponent from analytical solution has same trend with model ones for all cases, which can be considered as another verification of the semi-analytical model. On the other hand, note that the empirical function yields a wider sigmoidal curve for the ***b*** exponent. Deviation from ***b***=2 starts earlier than other solutions while time to reach terminal decline (***b***=0) is deferred. As seen in **Fig. 4.4**, empirical function has less than 3% of error in predicting mean matrix pressure compared to analytical solution. However, this error is magnified at middle time

period due to formulation of ***b*** exponent. It is worth to mention that, analysis of the flow regimes is carried out on the basis of ***b*** exponent rather than classical log-log rate versus time plot.

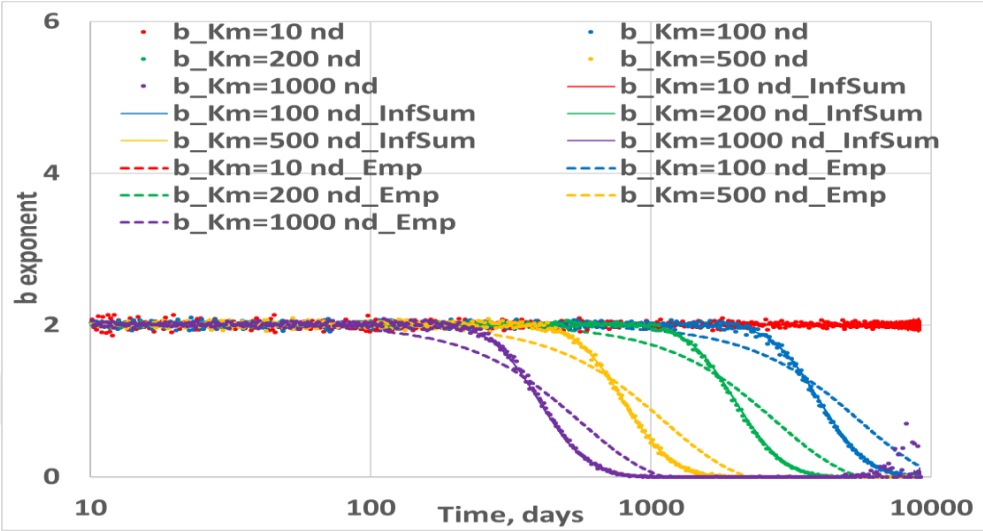

Figure 5.5: The ***b*** exponent behavior of empirical function for matrix permeability.

5.4.2 Matrix Porosity

The smaller matrix porosity means smaller volume to deplete such that elapsed time to reach boundary-dominated flow becomes shorter as shown in **Fig. 5.6**. As in the case of matrix permeability, ***b*** exponent starts to decline from value of 2 at t_D = 0.02 and reaches to zero at t_D = 0.1 (**Fig. 5.7**). One interesting observation is presence of single flow rate behavior on dimensionless time plot after some production period (t_D starts at 1×10^{-4}) even though original rate profiles of the cases are somewhat different. From time perspective, higher matrix porosity delays time to reach same flow rate compared to cases with smaller porosity. However, time increment is compensated by porosity increment and it ends with same value because of its formulation. Again, ***b*** exponent from empirical function is not able to reflect narrower S-shape profile at transition period (**Fig. 5.8**).

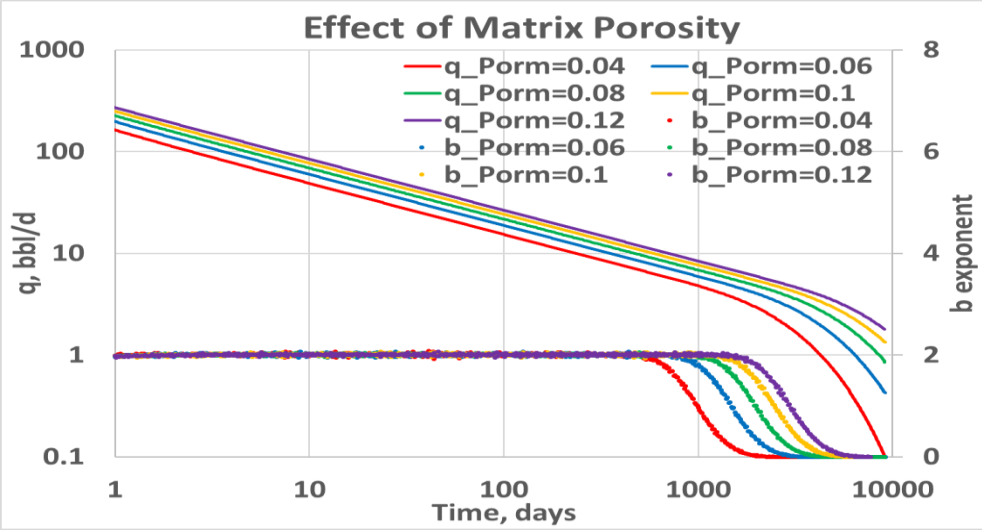

Figure 5.6: Sensitivity analysis for matrix porosity.

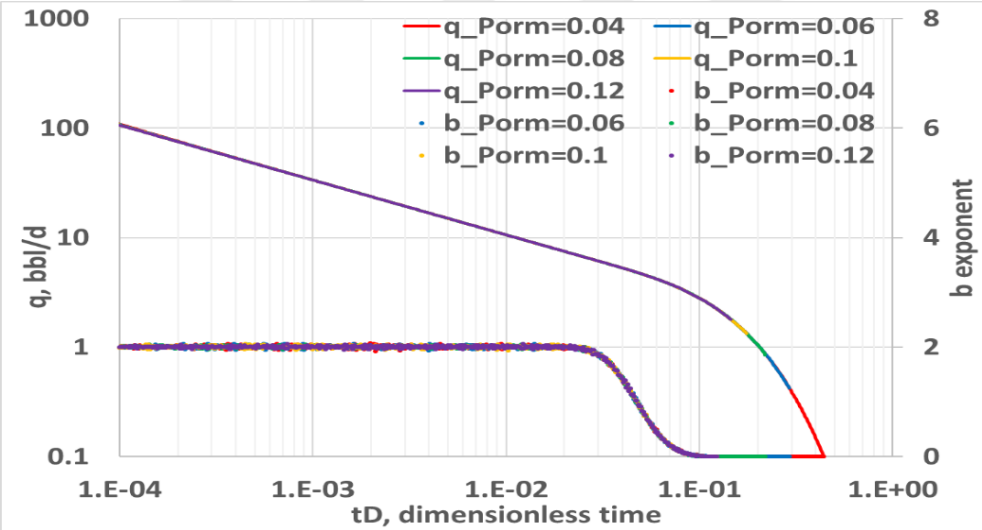

Figure 5.7: The q vs. ***b*** exponent behavior in dimensionless time for matrix porosity.

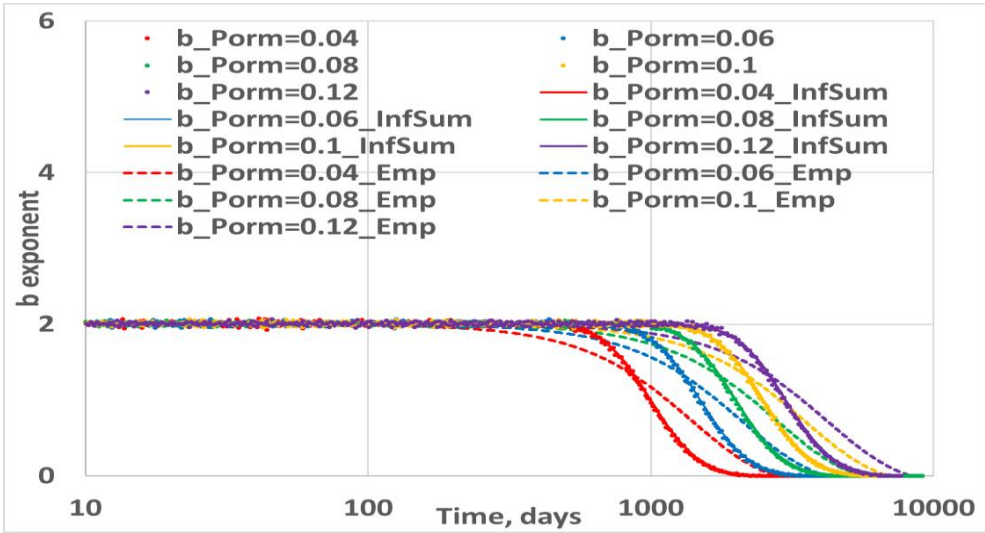

Figure 5.8: The ***b*** exponent behavior of empirical function for matrix porosity.

5.4.3 Matrix Rock Compressibility

Assigning matrix rock compressibility from experiments for shale is difficult. On the contrary, limited uncertainty exists in produced fluid. Therefore, wide range of compressibility values are preferred to estimate its effect on production profile as well as on ***b*** exponent. Higher compressibility enhances reservoir energy resulting in a prolonged linear flow period as demonstrated in **Fig. 5.9**. First two cases are very close to each other since total compressibility is dominated by the fluid compressibility (1.35×10^{-5} psi^{-1}). As in the case of matrix porosity, single profile is seen in both flow rate and ***b*** exponent for the cases (**Fig. 5.10**). The effect of larger time associated with longer period of linear flow in the numerator is cancelled out by higher compressibility in the denominator. The ***b*** exponent is again aligned with analytical solution but sharpness of the curve at transition period is not observed in the case of empirical function (**Fig. 5.11**).

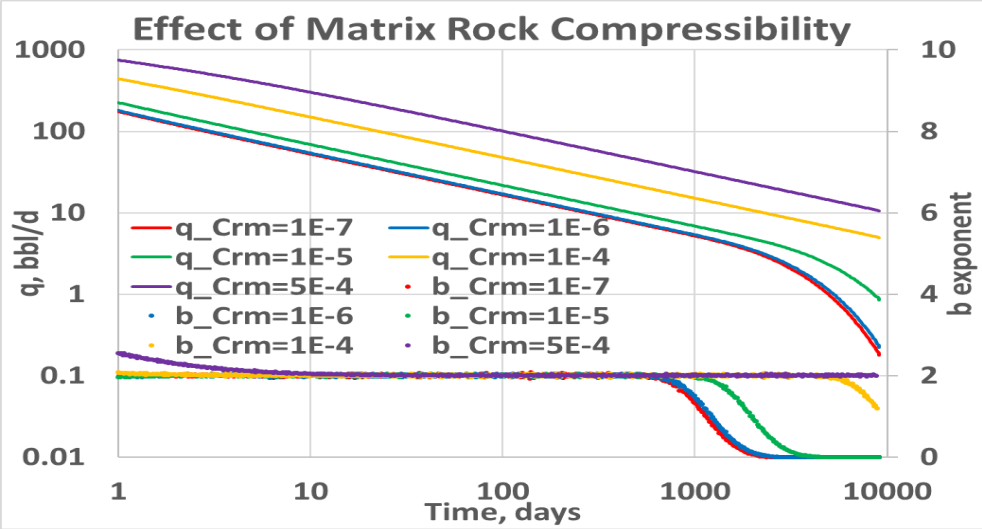

Figure 5.9: Sensitivity analysis for matrix rock compressibility.

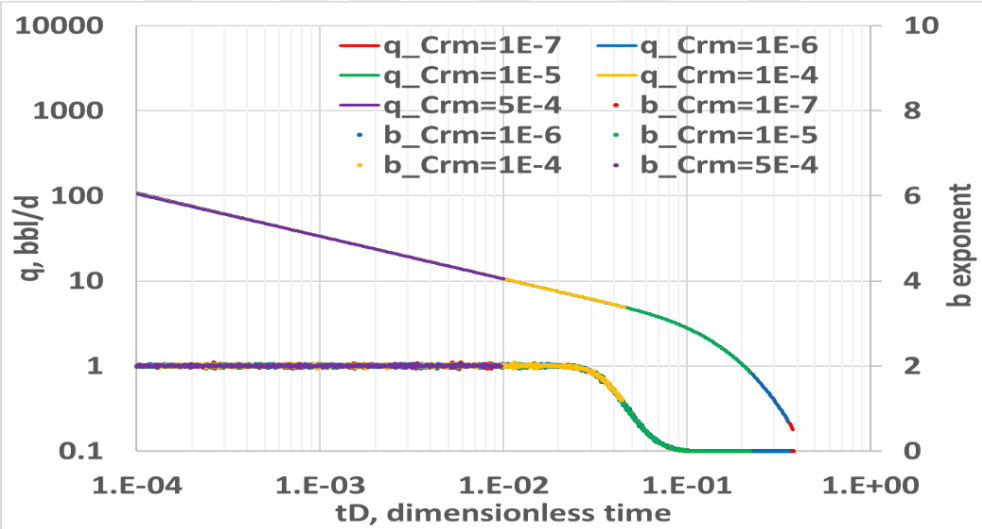

Figure 5.10: The q vs. ***b*** exponent behavior in dimensionless time for matrix rock compressibility.

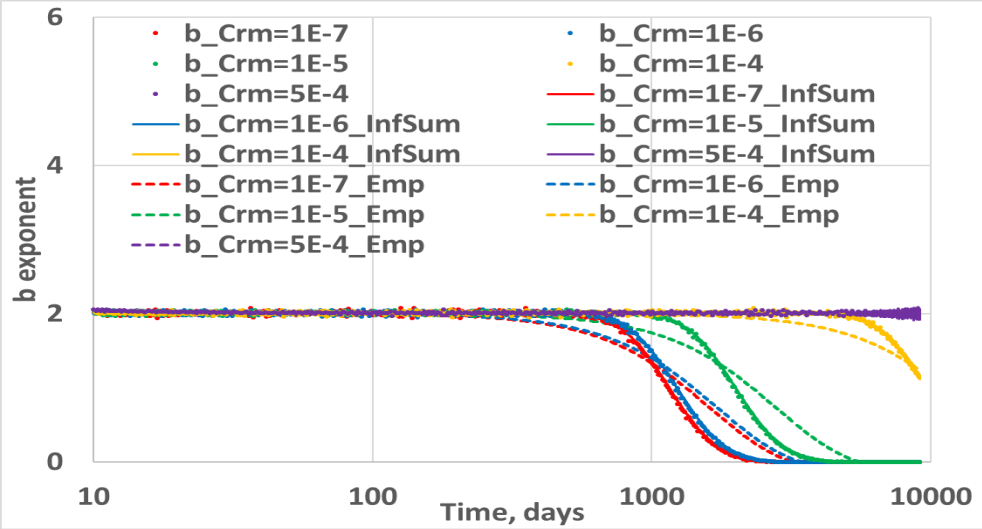

Figure 5.11: The ***b*** exponent behavior of empirical function for matrix rock compressibility.

5.4.4 Fracture Spacing

Fracture spacing is another controversial topic being discussed by the industry. The current trend of denser spacing does not guarantee forming a large planar fracture at each cluster. Coarser spacing means laterally bigger matrix slab. As demonstrated in **Fig. 5.12**, smaller matrix reaches to boundary-dominated flow earlier.

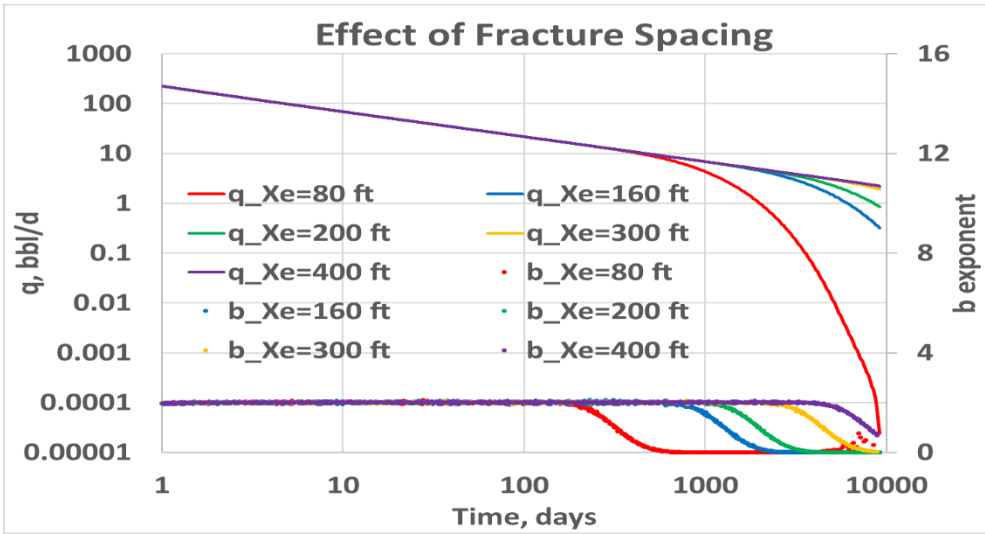

Figure 5.12: Sensitivity analysis for fracture spacing.

In t_D plot (**Fig. 5.13**), the order of rates seems reversed even though they are same during matrix linear flow. However, it is totally related to formulation of t_D such that same t_D value corresponds to early time for small matrix block while it becomes late time for bigger matrix. Once again, end of linear flow is seen at t_D of 0.02 and boundary-dominated flow starts at t_D of 0.1. The mismatch in ***b*** exponent between empirical function and model is persistent at transition period (**Fig. 5.14**).

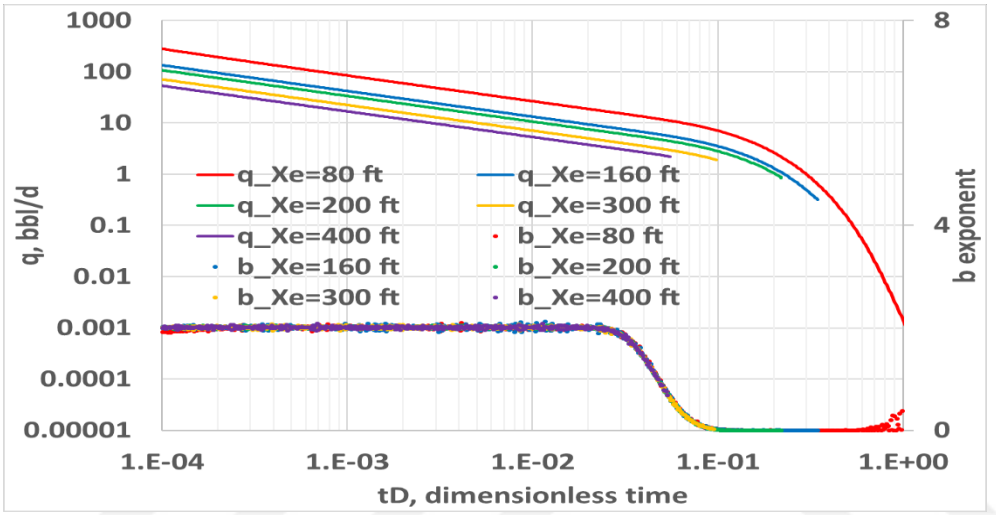

Figure 5.13: The q vs. ***b*** exponent behavior in dimensionless time for matrix fracture spacing.

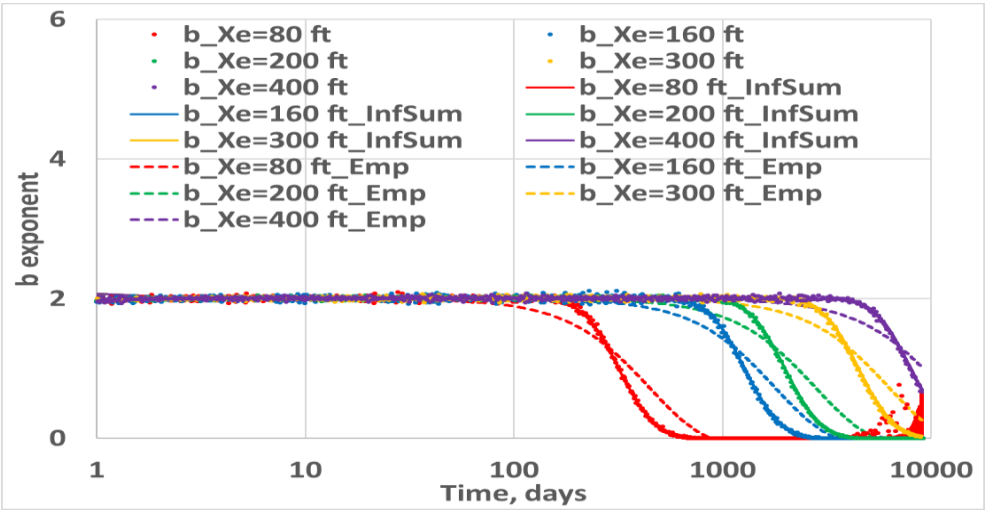

Figure 5.14: The ***b*** exponent behavior of empirical function for fracture spacing.

5.4.5 Fracture Half-Length

Fracture half-length is one of the key parameters in achieving high flow rates. It can be easily seen in **Fig. 5.15** that the longer the fracture is, the higher production will be because of larger surface area open to flow. On the other hand, ***b*** exponent profiles are quite similar. The underlying reason is that all models have same ratio of model flow area to model volume, even fracture half-lengths are changing. Thus, fracture half-length does not have any effect on ***b*** exponent for this reservoir configuration.

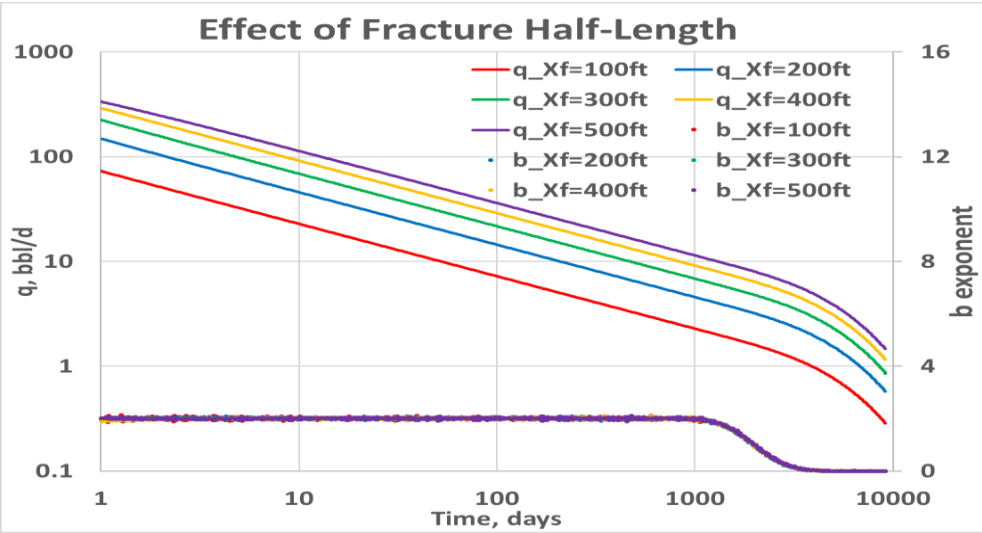

Figure 5.15: Sensitivity analysis for fracture half-length.

5.4.6 Fracture Conductivity

Fracture conductivity is important for operating companies in evaluation of frac design, specifically selection of proppant mesh size and its concentration. Fracture conductivity of 0.5 md-ft exhibits bilinear flow with a quarter slope in log-log rate versus time plot for almost 30 days as seen in **Fig. 5.16**. The ***b*** exponent is equal to 4, which was mentioned previously by Kupchenko et al. (2008) obtained from flow rate-time$^{-1/4}$ relation during this period. In this case, pure matrix linear flow is not observed clearly, rather transition from bilinear to boundary-dominated flow covers almost half of the production period. From sensitivity cases, it can also be concluded

that creating a fracture larger than 5 md-ft conductivity matters only in first month of the production. Since fracture conductivity, fracture half-length and fracture rock compressibility are not inputs to inter-porosity flow term, plotting decline profile in t_D and comparing ***b*** exponent mentioned approaches are meaningless. That's why, they are not presented.

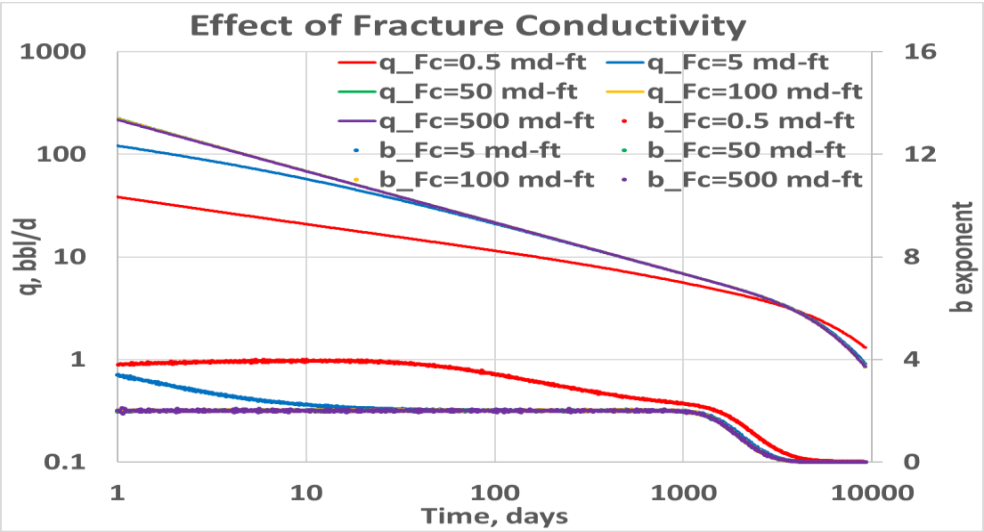

Figure 5.16: Sensitivity to fracture conductivity.

5.4.7 Fracture Rock Compressibility

As shown in **Fig. 5.17**, fracture rock compressibility is only effective at early production time. Higher values of rock compressibility cause fracture linear flow for a very small time, practically not seen in real data. Two distinct linear flow creates two different sigmoidal signatures, where ***b*** exponent in fracture linear flow does not approach to zero due to matrix contribution. Also, ***b*** exponent is bigger than value of 2 at end of transition period. Similar multi-sigmoidal behavior associated with flow regimes and ***b*** exponent bigger than 2 were reported by Varma et al. (2018), shown in **Fig. 2.6**. As a result of fluid compressibility domination in total compressibility, small fracture rock compressibility does not change production behavior. Matrix linear flow is observed for all cases, as expected.

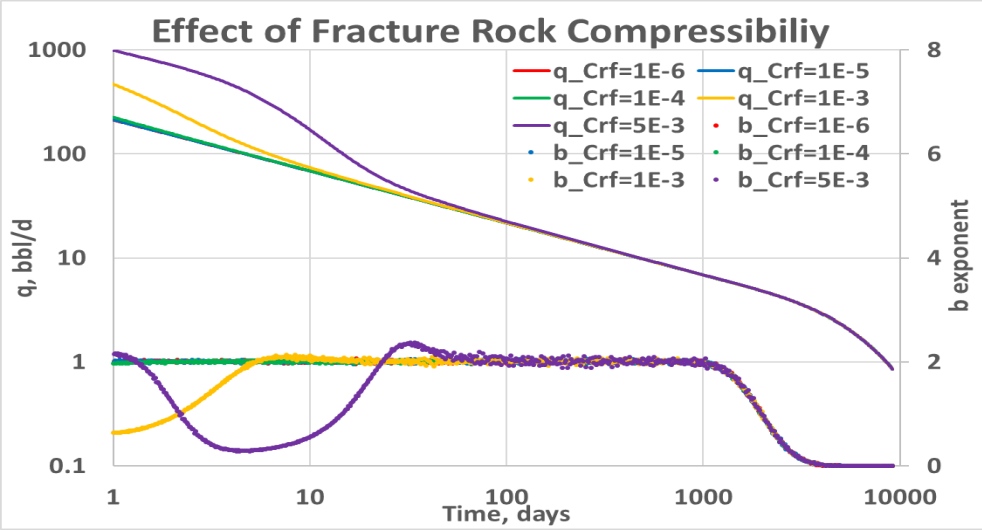

Figure 5.17: Sensitivity analysis for fracture rock compressibility.

5.4.8 Empirical Function

Another interesting observation is deviation of ***b*** exponent calculated from empirical function at transition flow period. In **Fig. 5.18**, mean matrix pressure of base case calculated from empirical function defined in Eq. 76 (dashed green line) is almost same with exact analytical solution defined in Eq. 75 (dashed red line). However, same level of accuracy is not seen in ***b*** exponent estimation at transition flow period (solid lines) in spite of using same inter-porosity flow term (Eq. 74). The fundamental reason of this mismatch is total number of differentiation. In other words, ***b*** exponent is actually a result of three consecutive differentiation of mean matrix pressure. Therefore, small differences in mean matrix pressure are magnified at each derivative operation until arriving final ***b*** exponent at that time. Based on these findings, it can be concluded that ***b*** exponent is very sensitive to minor changes and its sensitivity increases during transition flow period.

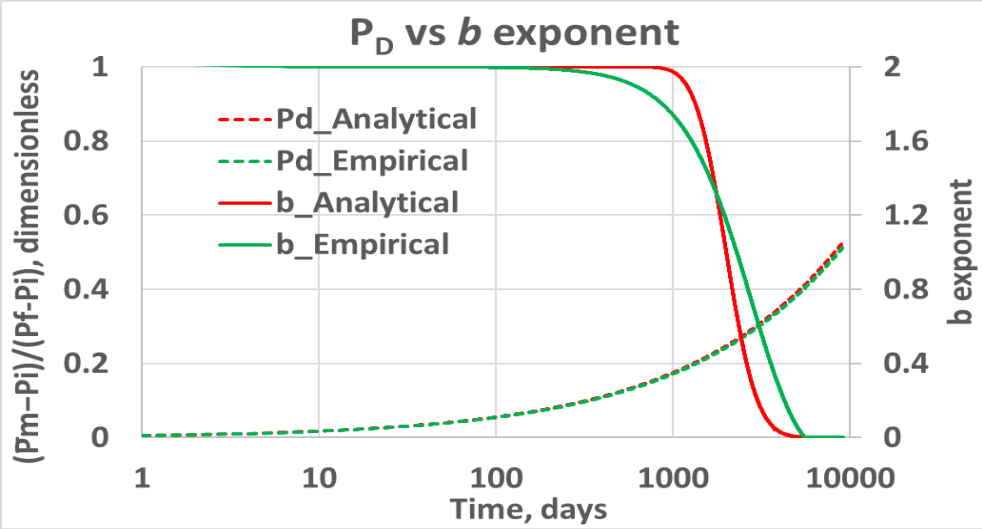

Figure 5.18: Mean matrix pressure and ***b*** exponent comparison for base case.

CHAPTER 6

CONCLUSIONS AND RECOMMENDATIONS

In this study, accuracy of existing dual-porosity reservoir simulation with constant shape factors is analyzed for fractured shale reservoirs. In this respect, different types of boundary conditions are considered for 3D rectangular anisotropic matrix to eliminate any misinterpretation associated to boundary condition type. Analytical solutions of pressure diffusion and time-dependent shape factors are obtained for all boundary conditions. Also, reduced forms of shape factors in terms of dimension and homogeneity are presented. Furthermore, new empirical functions are proposed to mimic real behavior of mean matrix pressure and shape factor. For validation of derived time-dependent shape factors and their proposed simplifications, fine scale single-porosity numerical models are employed. Apart from these, effects of key reservoir and completion parameters on production and hyperbolic decline exponent (***b*** exponent) are assessed by using semi-analytical transient dual-porosity models. Possibility of generating ***b*** exponent from inter-porosity flow term with two different approaches is tested. The following conclusions are drawn:

- Modeling unsteady-state flow period is crucial as it covers most of economic production life of well in shale formations.
- Assumption of linear pressure profile between matrix and fracture is not valid in fractured shale reservoirs.
- Non-linearity observed in unsteady-state period lasts for a long time and this period cannot be accurately modeled by constant shape factors.
- The tighter the matrix is, the larger the error will be in classical dual-porosity formulation.
- Implementation of time-dependent shape factor eliminates this deficiency without demanding further discretization.

- Empirical functions are robust in modeling of not only transient period, but also late time behavior as opposed to constant shape factor.
- New empirical functions can be easily implemented in dual-porosity simulation without adding computational complexity.
- Not only simplicity of function itself but also its derivative form is crucial to obtain stable solution.
- Switching between time dependent and independent shape factor can be implemented for functions, which perform very well at reflecting early time behavior but become incorrect at pseudo-steady state period.
- 1st term approximation for constant rate boundary condition provides reliable forecasts in transient flow period.
- Having better permeability or denser fractures and higher initial drawdown extends constant pressure behavior in shape factor profile for linearly declining fracture pressure.
- Earlier switching time or steeper decline in fracture pressure displays deviation from constant pressure behavior forward in shape factor profile for linearly declining fracture pressure.
- Matrix linear flow yields a $\boldsymbol{b}$ exponent of 2.
- End of linear flow based on $\boldsymbol{b}$ exponent occurs at a t_D of 0.02 whereas boundary-dominated flow starts at a t_D of 0.1.
- Proposed empirical function is accurate at both early and late times in predicting $\boldsymbol{b}$ exponent from inter-porosity flow term but it fails at transition flow period.
- Duration of matrix linear flow decreases with increase in matrix permeability as well as reduction in matrix porosity, total matrix compressibility and fracture spacing.
- The $\boldsymbol{b}$ exponent is insensitive to variation of fracture half-length because of constant flow area per unit volume for the studied reservoir configuration.

- Effect of fracture conductivity on ***b*** exponent behavior is limited except for too small values, where bilinear flow is seen and long transition period can mask matrix linear flow.
- Variation of fracture rock compressibility only dominates early time behavior in a certain extent but this period is rarely seen in real production data.

As stated in derivations, fluid is assumed as slightly compressible such that its properties are constant. Similarly, rock properties are also not function of pressure. For future studies, following cases should be considered to extend this work:

- Compressible fluid with pseudo-pressure implementation
- Compressible fluid with pseudo-pressure and pseudo-time implementation
- Stress-dependent rock properties with pseudo-pressure implementation
- The ***b*** exponent behavior for compressible fluid (dry gas)

REFERENCES

Agarwal, R.G., 1979. “Real Gas Pseudo-Time” - A New Function For Pressure Buildup Analysis Of MHF Gas Wells, in: SPE Annual Technical Conference and Exhibition. Society of Petroleum Engineers, Las Vegas, Nevada, p. 12. https://doi.org/10.2118/8279-MS

Aguilera, R., 1987. An Approximate Solution Of Linear Flow In Naturally Fractured Reservoirs.

Ahmed, U., Meehan, D.N., 2016. Characteristics of Unconventional Oil and Gas Resources In Unconventional Oil and Gas Resources : Exploitation and Development. CRC Press,Taylor & Francis Group,2016, Boca Raton, Florida, US.

Al-Ahmadi, H.A.H., 2010. A Triple-Porosity Model for Fractured Horizontal Wells. PhD Dissertation. Texas A&M University, College Station, Texas.

Al-Hussainy, R., Ramey Jr., H.J., 1966. Application of Real Gas Flow Theory to Well Testing and Deliverability Forecasting. J. Pet. Technol. 18, 637–642. https://doi.org/10.2118/1243-B-PA

Anderson, D.M., Mattar, L., 2007. An Improved Pseudo-Time for Gas Reservoirs With Significant Transient Flow. J. Can. Pet. Technol. 46, 6. https://doi.org/10.2118/07-07-05

Arnold, R., Anderson, R., 1908. Preliminary Report on the Coalinga Oil District, Fresno and Kings Counties, California, Bulletin. https://doi.org/10.3133/b357

Arps, J.J., 1945. Analysis of Decline Curves. Trans. AIME 160, 228–247. https://doi.org/10.2118/945228-G

Barenblatt, G.I., Zheltov, I.P., Kochina, I.N., 1960. Basic concepts in the theory of seepage of homogeneous liquids in fissured rocks [strata]. J. Appl. Math. Mech. 24, 1286–1303. https://doi.org/10.1016/0021-8928(60)90107-6

Barree, R.D., Cox, S.A., Miskimins, J.L., Gilbert, J. V, Conway, M.W., 2015. Economic Optimization of Horizontal-Well Completions in Unconventional Reservoirs. SPE Prod. Oper. 30, 293–311. https://doi.org/10.2118/168612-PA

Bello, R.O., 2009. Rate Transient Analysis in Shale Gas Reservoirs with Transient Linear Behavior. PhD Dissertation. Texas A&M University, College Station, Texas.

Bhandari, A.R., Flemings, P.B., Hofmann, R., Polito, P.J., 2018. Stress-Dependent In Situ Gas Permeability in the Eagle Ford Shale. Transp. Porous Media 123, 1–20. https://doi.org/10.1007/s11242-018-1021-6

Bratovich, M.W., Walles, F., 2016. Formation Evaluation and Reservoir Characterization of Source Rock Reservoirs, in: Ahmed, U., Meehan, D.N. (Eds.), Unconventional Oil and Gas Resources Exploitation and Development. CRC Press,Taylor & Francis Group,2016, Boca Raton, Florida, US, pp. 8–3.

Brown, M.L., Ozkan, E., Raghavan, R.S., Kazemi, H., 2009. Practical Solutions for Pressure Transient Responses of Fractured Horizontal Wells in Unconventional Reservoirs, in: SPE Annual Technical Conference and Exhibition. Society of Petroleum Engineers, New Orleans, Louisiana, p. 18. https://doi.org/10.2118/125043-MS

Carslaw, H.S., Jaeger, J.C., 1959. Conduction of heat in solids, 2nd Edition. Oxford University Press, Oxford, England.

Chang, M.-M., 1993. Deriving the shape factor of a fractured rock matrix. United States. https://doi.org/10.2172/10192737

Chen, Z., Liao, X., Zhao, X., Dou, X., Zhu, L., 2016. Development of a Trilinear-Flow Model for Carbon Sequestration in Depleted Shale. SPE J. 21, 1386–1399. https://doi.org/10.2118/176153-PA

Cho, Y., Ozkan, E., Apaydin, O.G., 2013. Pressure-Dependent Natural-Fracture Permeability in Shale and Its Effect on Shale-Gas Well Production. SPE Reserv.

Eval. Eng. 16, 216–228. https://doi.org/10.2118/159801-PA

Choquette, P.W., Pray, L.C., 1970. Geologic Nomenclature and Classification of Porosity in Sedimentary Carbonates. Am. Assoc. Pet. Geol. Bull. 54, 207–250. https://doi.org/10.1306/5D25C98B-16C1-11D7-8645000102C1865D

Cinco-Ley, H., Samaniego-V., F., 1981. Transient Pressure Analysis for Fractured Wells. J. Pet. Technol. 33, 1749–1766. https://doi.org/10.2118/7490-PA

Clark, A.J., Lake, L.W., Patzek, T.W., 2011. Production Forecasting with Logistic Growth Models, in: SPE Annual Technical Conference and Exhibition. Society of Petroleum Engineers, Denver, Colorado, USA. https://doi.org/10.2118/144790-MS

Coats, K.H., 1989. Implicit Compositional Simulation of Single-Porosity and Dual-Porosity Reservoirs. SPE Symp. Reserv. Simul. https://doi.org/10.2118/18427-MS

Crank, J., 1975. The mathematics of diffusion, 2nd Edition. Clarendon Press, Oxford, England.

Cutler, W.W., 1924. Estimation of Underground Oil Reserves by Oil-Well Production Curves. U.S. Burea Mines Bull. 228.

Davudov, D., Moghanloo, R.G., Lan, Y., 2018. Pore Volume Compressibility in Shale - Revisited, in: SPE Annual Technical Conference and Exhibition. Society of Petroleum Engineers, Dallas, Texas, USA. https://doi.org/10.2118/191700-MS

De Swaan, A., 1990. Influence of Shape and Skin of Matrix-Rock Blocks on Pressure Transients in Fractured Reservoirs. SPE Form. Eval. 5, 344–352. https://doi.org/10.2118/15637-PA

De Swaan, A., 1976. Analytic Solutions for Determining Naturally Fractured Reservoir Properties by Well Testing. Soc. Pet. Eng. J. 16, 117–122. https://doi.org/10.2118/5346-PA

Duguid, J.O., Lee, P.C.Y., 1977. Flow in fractured porous media. Water Resour. Res. 13, 558–566. https://doi.org/10.1029/WR013i003p00558

Duong, A.N., 2011. Rate-Decline Analysis for Fracture-Dominated Shale Reservoirs. SPE Reserv. Eval. Eng. 14, 377–387. https://doi.org/10.2118/137748-PA

Dykhuizen, R.C., 1990. A new coupling term for dual-porosity models. Water Resour. Res. 26, 351–356. https://doi.org/10.1029/WR026i002p00351

Eclipse, 2019. E100 Black-Oil Simulator, version 2019. Eclipse® Schlumberger, Houston, Texas, USA

EIA, 2021a. Major Tight Oil and Shale Gas Plays in Lower 48 States. Retrieved on July 2021 from https://www.eia.gov/special/shaleplays/

EIA, 2021b. Crude Oil Production. Retrieved on July 2021 from https://www.eia.gov/dnav/pet/pet_crd_crpdn_adc_mbbl_m.htm

EIA, 2021c. Natural Gas Gross Withdrawals and Production. Retrieved on July 2021 from https://www.eia.gov/dnav/ng/NG_PROD_SUM_DC_NUS_MMCF_M.htm

El-Banbi, A.H., 1998. Analysis of Tight Gas Well Performance. PhD Dissertation. Texas A&M University, College Station, Texas.

Ezulike, D.O., Dehghanpour, H., 2014. A model for simultaneous matrix depletion into natural and hydraulic fracture networks. J. Nat. Gas Sci. Eng. 16, 57–69. https://doi.org/10.1016/J.JNGSE.2013.11.004

Fulford, D.S., Blasingame, T.A., 2013. Evaluation of Time-Rate Performance of Shale Wells using the Transient Hyperbolic Relation, in: SPE Unconventional Resources Conference Canada. Society of Petroleum Engineers, Calgary, Alberta, Canada. https://doi.org/10.2118/167242-MS

Gandossi, L., Andrei, B.-D., Spisto, A., 2017. International Developments in the Field of Unconventional Gas and Oil Extraction: Update 2017. https://doi.org/10.2760/372964

Gray, J.K., 1977. Future Gas Reserve Potential Western Canadian Sedimentary Basin:3d Natl. Tech. Conf. Canadian Gas Assoc.

Gringarten, A.C., Ramey Jr., H.J., Raghavan, R., 1974. Unsteady-State Pressure Distributions Created by a Well With a Single Infinite-Conductivity Vertical Fracture. Soc. Pet. Eng. J. 14, 347–360. https://doi.org/10.2118/4051-PA

Hahn, D.W., Ozisik, M.N., 2012. Use of Duhamel's Theorem, in: Heat Conduction, Wiley Online Books. pp. 273–299. https://doi.org/https://doi.org/10.1002/9781118411285.ch7

Holditch, S.A., 2006. Tight Gas Sands. J. Pet. Technol. 58, 86–93. https://doi.org/10.2118/103356-JPT

Huang, S., Yao, Y., Ma, R., Wang, J., 2019. Analytical model for pressure and rate analysis of multi-fractured horizontal wells in tight gas reservoirs. J. Pet. Explor. Prod. Technol. 9,383–396. https://doi.org/10.1007/s13202-018-0462-3

Ilk, D., Blasingame, T., Houzé, O., 2016. Practical Considerations for Well Performance Analysis and Forecasting in Shale Plays. Open Pet. Eng. J. 9, 107–136. https://doi.org/10.2174/1874834101609010107

Ilk, D., Rushing, J.A., Perego, A.D., Blasingame, T.A., 2008. Exponential vs. Hyperbolic Decline in Tight Gas Sands: Understanding the Origin and Implications for Reserve Estimates Using Arps' Decline Curves, in: SPE Annual Technical Conference and Exhibition. Society of Petroleum Engineers, Denver, Colorado, USA. https://doi.org/10.2118/116731-MS

Javadpour, F., Fisher, D., Unsworth, M., 2007. Nanoscale Gas Flow in Shale Gas Sediments. J. Can. Pet. Technol. 46, 7. https://doi.org/10.2118/07-10-06

Ji, J., Yao, Y., Huang, S., Ma, X., Zhang, S., Zhang, F., 2017. Analytical model for

production performance analysis of multi-fractured horizontal well in tight oil reservoirs. J. Pet. Sci. Eng. 158, 380–397. https://doi.org/10.1016/J.PETROL.2017.08.037

Jiang, J., Younis, R.M., 2016. Hybrid Coupled Discrete-Fracture/Matrix and Multicontinuum Models for Unconventional-Reservoir Simulation. SPE J. 21, 1009–1027. https://doi.org/10.2118/178430-PA

Jiang, Z., Zhang, W., Liang, C., Wang, Y., Liu, H., Chen, X., 2016. Basic Characteristics and Evaluation of Shale Oil Reservoirs. Pet. Res. 1, 149–163. https://doi.org/https://doi.org/10.1016/S2096-2495(17)30039-X

Johnson, R.H., Bollens, A.L., 1927. The Loss Ratio Method of Extrapolating Oil Well Decline Curves. Trans. AIME 77, 771–778. https://doi.org/10.2118/927771-G

Joshi, K., Lee, W.J., 2013. Comparison of Various Deterministic Forecasting Techniques in Shale Gas Reservoirs, in: SPE Hydraulic Fracturing Technology Conference. Society of Petroleum Engineers, The Woodlands, Texas, USA, p. 12. https://doi.org/10.2118/163870-MS

Kazemi, H., 1969. Pressure Transient Analysis of Naturally Fractured Reservoirs with Uniform Fracture Distribution. Soc. Pet. Eng. J. 9, 451–462. https://doi.org/10.2118/2156-A

Kazemi, H., Merrill Jr., L.S., Porterfield, K.L., Zeman, P.R., 1976. Numerical Simulation of Water-Oil Flow in Naturally Fractured Reservoirs. Soc. Pet. Eng. J. 16, 317–326. https://doi.org/10.2118/5719-PA

Kennedy, R.L., Knecht, W.N., Georgi, D.T., 2012. Comparisons and contrasts of Shale Gas and Tight Gas developments, North American experience and trends, in: Society of Petroleum Engineers - SPE Saudi Arabia Section Technical Symposium and Exhibition 2012. Society of Petroleum Engineers, pp. 159–185.

King, G.E., 2012. Hydraulic Fracturing 101: What Every Representative, Environmentalist, Regulator, Reporter, Investor, University Researcher, Neighbor, and Engineer Should Know About Hydraulic Fracturing Risk. J. Pet. Technol. 64, 34–42. https://doi.org/10.2118/0412-0034-JPT

Kupchenko, C.L., Gault, B.W., Mattar, L., 2008. Tight Gas Production Performance Using Decline Curves, in: CIPC/SPE Gas Technology Symposium 2008 Joint Conference. Society of Petroleum Engineers, Calgary, Alberta, Canada. https://doi.org/10.2118/114991-MS

Kurtoglu, B., 2013. Integrated Reservoir Characterization and Modeling in Support of Enhanced Oil Recovery for Bakken. PhD Dissertation. Colorado School of Mines, Golden, Colorado.

Lewis, J.O., Beal, C.H., 1918. Some New Methods for Estimating the Future Production of Oil Wells. Trans. AIME 59, 492–525. https://doi.org/10.2118/918492-G

Li, L., Lee, S.H., 2008. Efficient Field-Scale Simulation of Black Oil in a Naturally Fractured Reservoir Through Discrete Fracture Networks and Homogenized Media. SPE Reserv. Eval. Eng. 11, 750–758. https://doi.org/10.2118/103901-PA

Lim, K.T., Aziz, K., 1995. Matrix-fracture transfer shape factors for dual-porosity simulators. J. Pet. Sci. Eng. 13, 169–178. https://doi.org/https://doi.org/10.1016/0920-4105(95)00010-F

Loucks, R.G., Reed, R.M., Ruppel, S.C., Hammes, U., 2012. Spectrum of Pore Types and Networks in Mudrocks and a Descriptive Classification for Matrix-Related Mudrock Pores. Am. Assoc. Pet. Geol. Bull. 96, 1071–1098. https://doi.org/10.1306/08171111061

Maley, S., 1985. The Use of Conventional Decline Curve Analysis in Tight Gas Well Applications, in: SPE/DOE Low Permeability Gas Reservoirs Symposium. Society of Petroleum Engineers, Denver, Colorado.

https://doi.org/10.2118/13898-MS

Martin, S.O., Holditch, S., Ayers, W.B., McVay, D., 2010. PRISE Validates Resource Triangle Concept. SPE Econ. Manag. 2, 51–60. https://doi.org/10.2118/117703-PA

Masters, J.A., 1979. Deep Basin Gas Trap, Western Canada. Am. Assoc. Pet. Geol. Bull. 63, 152–181. https://doi.org/10.1306/C1EA55CB-16C9-11D7-8645000102C1865D

Matthews, C.S., Russell, D.G., 1967. Pressure Buildup and Flow Tests in Wells., SPE Monogr. ed. Society of Petroleum Engineers, Dallas.

Mayerhofer, M., Oduba, O., Agarwal, K., Melcher, H., Lolon, E., Bartell, J., Weijers, L., 2017. A Cost/Benefit Review of Completion Choices in the Williston Basin Using a Hybrid Physics-Based Modeling/Multi-Variate Analysis Approach, in: SPE Annual Technical Conference and Exhibition. Society of Petroleum Engineers, San Antonio, Texas, USA. https://doi.org/10.2118/187254-MS

McClure, M., Picone, M., Fowler, G., Ratcliff, D., Kang, C., Medam, S., Frantz, J., 2020. Nuances and Frequently Asked Questions in Field-Scale Hydraulic Fracture Modeling, in: SPE Hydraulic Fracturing Technology Conference and Exhibition. Society of Petroleum Engineers, The Woodlands, Texas, USA. https://doi.org/10.2118/199726-MS

Meyet Me Ndong, M.P., Dutta, R., Burns, C., 2013. Comparison of Decline Curve Analysis Methods with Analytical Models in Unconventional Plays, in: SPE Annual Technical Conference and Exhibition. Society of Petroleum Engineers, New Orleans, Louisiana, USA, p. 32. https://doi.org/10.2118/166365-MS

Molina, O.M., 2019. Application of Pressure and Rate Transient Analyses to Stress-Sensitive Multi-Fractured Composite Systems and Compartmentalized Reservoirs. Louisiana State University and Agricultural and Mechanical College.

Nelson, P.H., 2009. Pore-throat sizes in sandstones, tight sandstones, and shales. Am. Assoc. Pet. Geol. Bull. 93, 329–340. https://doi.org/10.1306/10240808059

Ozkan, E., Raghavan, R.S., Apaydin, O.G., 2010. Modeling of Fluid Transfer From Shale Matrix to Fracture Network, in: SPE Annual Technical Conference and Exhibition. Society of Petroleum Engineers, Florence, Italy, p. 18. https://doi.org/10.2118/134830-MS

Passey, Q.R., Bohacs, K., Esch, W.L., Klimentidis, R., Sinha, S., 2010. From Oil-Prone Source Rock to Gas-Producing Shale Reservoir - Geologic and Petrophysical Characterization of Unconventional Shale Gas Reservoirs. Int. Oil Gas Conf. Exhib. China. https://doi.org/10.2118/131350-MS

Pedrosa Jr., O.A., 1986. Pressure Transient Response in Stress-Sensitive Formations, in: SPE California Regional Meeting. Society of Petroleum Engineers, Oakland, California, p. 12. https://doi.org/10.2118/15115-MS

Prats, M., Hazebroek, P., Strickler, W.R., 1962. Effect of Vertical Fractures on Reservoir Behavior--Compressible-Fluid Case. Soc. Pet. Eng. J. 2, 87–94. https://doi.org/10.2118/98-PA

Pruess, K., Wu, Y.-S., 1993. A New Semi-Analytical Method for Numerical Simulation of Fluid and Heat Flow in Fractured Reservoirs. SPE Adv. Technol. Ser. 1, 63–72. https://doi.org/10.2118/18426-PA

Qanbari, F., Clarkson, C.R., 2013. Analysis of Transient Linear Flow in Tight Oil and Gas Reservoirs with Stress-Sensitive Permeability and Multi-Phase Flow, in: SPE Unconventional Resources Conference Canada. Society of Petroleum Engineers, Calgary, Alberta, Canada, p. 13. https://doi.org/10.2118/167176-MS

Raghavan, R., 1972. A Review of the Consolidation and Rebound Processes in One-Dimensional Porous Columns, in: Fall Meeting of the Society of Petroleum Engineers of AIME. Society of Petroleum Engineers, San Antonio, Texas, p. 20. https://doi.org/10.2118/4078-MS

Rangel-German, E.R., Kovscek, A.R., Akin, S., 2010. Time-Dependent Shape Factors for Uniform and Non-Uniform Pressure Boundary Conditions. Transp. Porous Media 83, 591–601. https://doi.org/10.1007/s11242-009-9461-7

Raterman, K., Liu, Y., Warren, L., 2019. Analysis of a Drained Rock Volume: An Eagle Ford Example, in: SPE/AAPG/SEG Unconventional Resources Technology Conference. Society of Petroleum Engineers, Denver, Colorado, USA. https://doi.org/10.15530/urtec-2019-263

Ren, G., Jiang, J., Younis, R.M., 2017. Fully-Coupled XFEM-EDFM Hybrid Model for Geomechanics and Flow in Fractured Reservoirs. SPE Reserv. Simul. Conf. https://doi.org/10.2118/182726-MS

Ren, J., Guo, P., 2015. A novel semi-analytical model for finite-conductivity multiple fractured horizontal wells in shale gas reservoirs. J. Nat. Gas Sci. Eng. 24, 35–51. https://doi.org/10.1016/J.JNGSE.2015.03.015

Rezaee, R., Rothwell, M., 2015. Gas shale: Global Significance, Distribution, And Challenges. Fundam. Gas Shale Reserv., Wiley Online Books. https://doi.org/10.1002/9781119039228.ch1

Roadifer, R.D., Kalaei, M.H., 2015. Pseudo-Pressure and Pseudo-Time Analysis for Unconventional Oil Reservoirs With New Expressions for Average Reservoir Pressure During Transient Radial and Linear Flow, in: Unconventional Resources Technology Conference. Unconventional Resources Technology Conference, San Antonio, Texas, USA, p. 26. https://doi.org/10.15530/URTEC-2015-2172344

Robertson, S., 1988. Generalized Hyperbolic Equation. Society of Petroleum Engineers, Richardson, TX, USA.

Rouquerol, J., Avnir, D., Fairbridge, C.W., Everett, D.H., Haynes, J.H., Pernicone, N., Ramsay, J.D.F., Sing, K.S.W., Unger, K.K., 1994. Recommendations for the Characterization of Porous Solids (Technical Report). Pure Appl. Chem. https://doi.org/10.1351/pac199466081739

Rubin, B., 2010. Accurate Simulation of Non Darcy Flow in Stimulated Fractured Shale Reservoirs, in: SPE Western Regional Meeting. Society of Petroleum Engineers, Anaheim, California, USA. https://doi.org/10.2118/132093-MS

Rushing, J.A., Perego, A.D., Sullivan, R., Blasingame, T.A., 2007. Estimating Reserves in Tight Gas Sands at HP/HT Reservoir Conditions: Use and Misuse of an Arps Decline Curve Methodology, in: SPE Annual Technical Conference and Exhibition. Society of Petroleum Engineers, Anaheim, California, U.S.A. https://doi.org/10.2118/109625-MS

Serra, K., Reynolds, A.C., Raghavan, R., 1983. New Pressure Transient Analysis Methods for Naturally Fractured Reservoirs(includes associated papers 12940 and 13014). J. Pet. Technol. 35, 2271–2283. https://doi.org/10.2118/10780-PA

Shahvali, M., Gilman, J.R., Angola, O., Uland, M., Meng, H., Esler, K., Mukundakrishnan, K., Ghasemi, M., Natoli, V., 2016. Unconventional Reservoir Model Predictions Using Massively-Parallel Flow-Simulation: Bakken/Three Forks Reservoir Development Cases and SRV Testing, in: SPE Low Perm Symposium. Society of Petroleum Engineers, Denver, Colorado, USA. https://doi.org/10.2118/180204-MS

Spivey, J.P., Frantz Jr., J.H., Williamson, J.R., Sawyer, W.K., 2001. Applications of the Transient Hyperbolic Exponent, in: SPE Rocky Mountain Petroleum Technology Conference. Society of Petroleum Engineers, Keystone, Colorado, USA. https://doi.org/10.2118/71038-MS

Stalgorova, E., Mattar, L., 2016. Analytical Methods for Single-Phase Oil Flow: Accounting for Changing Liquid and Rock Properties, in: SPE Europec Featured at 78th EAGE Conference and Exhibition. Society of Petroleum Engineers, Vienna, Austria, p. 24. https://doi.org/10.2118/180139-MS

Stalgorova, K., Mattar, L., 2013. Analytical Model for Unconventional Multifractured Composite Systems. SPE Reserv. Eval. Eng. 16, 246–256.

https://doi.org/10.2118/162516-PA

Sun, H., Chawathe, A., Hoteit, H., Shi, X., Li, L., 2015. Understanding Shale Gas Flow Behavior Using Numerical Simulation. SPE J. 20, 142–154. https://doi.org/10.2118/167753-PA

Tabatabaie, S.H., Pooladi-Darvish, M., Mattar, L., Tavallali, M., 2017. Analytical Modeling of Linear Flow in Pressure-Sensitive Formations. SPE Reserv. Eval. Eng. 20, 215–227. https://doi.org/10.2118/181755-PA

Taler, J., 2014. Superposition Method for Multidimensional Heat Conduction Problems, in: Hetnarski, R.B. (Ed.), Encyclopedia of Thermal Stresses. Springer Netherlands, Dordrecht, pp. 4708–4718. https://doi.org/10.1007/978-94-007-2739-7_410

Tan, L., Zuo, L., Wang, B., 2018. Methods of Decline Curve Analysis for Shale Gas Reservoirs. Energies 11. https://doi.org/10.3390/en11030552

Tao, H., Zhang, L., Liu, Q., Deng, Q., Luo, M., Zhao, Y., 2018. An Analytical Flow Model for Heterogeneous Multi-Fractured Systems in Shale Gas Reservoirs. Energies 11, 3422. https://doi.org/10.3390/en11123422

Tugan, M.F., Weijermars, R., 2020. Variation in b-sigmoids with flow regime transitions in support of a new 3-segment DCA method: Improved production forecasting for tight oil and gas wells. J. Pet. Sci. Eng. 192, 107243. https://doi.org/https://doi.org/10.1016/j.petrol.2020.107243

Ueda, Y., Murata, S., Watanabe, Y., Funatsu, K., 1989. Investigation of the Shape Factor Used in the Dual-Porosity Reservoir Simulator. SPE Asia-Pacific Conf. https://doi.org/10.2118/SPE-19469-MS

Ugueto, G.A., Todea, F., Daredia, T., Wojtaszek, M., Huckabee, P.T., Reynolds, A., Laing, C., Chavarria, J.A., 2019. Can You Feel the Strain? DAS Strain Fronts for Fracture Geometry in the BC Montney, Groundbirch, in: SPE Annual Technical Conference and Exhibition. Society of Petroleum Engineers,

Calgary, Alberta, Canada. https://doi.org/10.2118/195943-MS

Valko, P.P., 2009. Assigning value to stimulation in the Barnett Shale: a simultaneous analysis of 7000 plus production hystories and well completion records, in: SPE Hydraulic Fracturing Technology Conference. Society of Petroleum Engineers, Woodlands, Texas. https://doi.org/10.2118/119369-MS

Valko, P.P., Lee, W.J., 2010. A Better Way To Forecast Production From Unconventional Gas Wells, in: SPE Annual Technical Conference and Exhibition. Society of Petroleum Engineers, Florence, Italy, p. 16. https://doi.org/10.2118/134231-MS

Varma, S., Tabatabaie, S.H., Ewert, J., Mattar, L., 2018. Variation of Hyperbolic-B-Parameter for Unconventional Reservoirs, and 3-Segment Hyperbolic Decline, in: SPE/AAPG/SEG Unconventional Resources Technology Conference. Society of Petroleum Engineers, Houston, Texas, USA. https://doi.org/10.15530/URTEC-2018-2892966

Vassilellis, G., Cipolla, C.L., Erdle, J.C., Ahmed, U., 2016. Production Evaluation and Forecasting, in: Ahmed, U., Meehan, D.N. (Eds.), Unconventional Oil and Gas Resources Exploitation and Development. CRC Press,Taylor & Francis Group,2016, Boca Raton, Florida, US, pp. 14–21.

Vermeulen, T., 1953. Theory for Irreversible and Constant-Pattern Solid Diffusion. Ind. Eng. Chem. 45, 1664–1670. https://doi.org/10.1021/ie50524a025

Vinsome, P.K.W., Westerveld, J., 1980. A Simple Method For Predicting Cap And Base Rock Heat Losses In' Thermal Reservoir Simulators. J. Can. Pet. Technol. 19, 5. https://doi.org/10.2118/80-03-04

Wang, L., Wang, X., 2016. Modelling of pressure transient behaviour for fractured gas wells under stress-sensitive and slippage effects. Int. J. Oil, Gas Coal Technol. 11, pp.18-38. https://doi.org/10.1504/IJOGCT.2016.073767

Wang, S., Ma, M., Ding, W., Lin, M., Chen, S., 2015. Approximate Analytical-

Pressure Studies on Dual-Porosity Reservoirs With Stress-Sensitive Permeability. SPE Reserv. Eval. Eng. 18, 523–533. https://doi.org/10.2118/174299-PA

Warren, J.E., Root, P.J., 1963. The Behavior of Naturally Fractured Reservoirs. Soc. Pet. Eng. J. 3, 245–255. https://doi.org/10.2118/426-PA

Wattenbarger, R.A., El-Banbi, A.H., Villegas, M.E., Maggard, J.B., 1998. Production Analysis of Linear Flow Into Fractured Tight Gas Wells. https://doi.org/10.2118/39931-MS

Weijermars, R., Paradis, K., Belostrino, E., Feng, F., Lal, T., Xie, A., Villareal, C., 2017. Re-appraisal of the Bakken Shale play: Accounting for historic and future oil prices and applying fiscal rates of North Dakota, Montana and Saskatchewan. Energy Strateg. Rev. 16, 68–95. https://doi.org/https://doi.org/10.1016/j.esr.2017.02.005

Weijers, L., Wright, C., Mayerhofer, M., Pearson, M., Griffin, L., Weddle, P., 2019. Trends in the North American Frac Industry: Invention through the Shale Revolution, in: SPE Hydraulic Fracturing Technology Conference and Exhibition. Society of Petroleum Engineers, The Woodlands, Texas, USA. https://doi.org/10.2118/194345-MS

Xiong, H., Gao, S., Li, H., 2017. Generate Type Well Performance Curves by Combining Multi-Segment Decline Models and Calibrated Numerical Simulation Models for UR Wells in Permian Basin, in: SPE/AAPG/SEG Unconventional Resources Technology Conference. Society of Petroleum Engineers, Austin, Texas, USA. https://doi.org/10.15530/URTEC-2017-2668394

Xue, X., Yang, C., Onishi, T., King, M.J., Datta-Gupta, A., 2019. Modeling Hydraulically Fractured Shale Wells Using the Fast-Marching Method With Local Grid Refinements and an Embedded Discrete Fracture Model. SPE J. Preprint, 19. https://doi.org/10.2118/193822-PA

Yang, D., Xue, X., Chen, J., 2018. High Resolution Hydraulic Fracture Network Modeling Using Flexible Dual Porosity Dual Permeability Framework, in: SPE Western Regional Meeting. Society of Petroleum Engineers, Garden Grove, California, USA, p. 14. https://doi.org/10.2118/190096-MS

Yu, W., Wu, K., Sepehrnoori, K., Xu, W., 2017. A Comprehensive Model for Simulation of Gas Transport in Shale Formation With Complex Hydraulic-Fracture Geometry. SPE Reserv. Eval. Eng. 20, 547–561. https://doi.org/10.2118/178747-PA

Zeng, J., Li, W., Liu, J., Leong, Y.-K., Elsworth, D., Tian, J., Guo, J., 2019. A 3-D Analytical Model for Multi-Stage Fractured Shale Gas Reservoirs with Damaged Fractures, in: SPE Europec Featured at 81st EAGE Conference and Exhibition. Society of Petroleum Engineers, London, England, UK, p. 31. https://doi.org/10.2118/195473-MS

Zeng, J., Wang, X., Guo, J., Zeng, F., 2016. Analytical Model for Multi-Fractured Horizontal Wells in Tight Sand Reservoir with Threshold Pressure Gradient, in: SPE Asia Pacific Hydraulic Fracturing Conference. Society of Petroleum Engineers, Beijing, China, p. 39. https://doi.org/10.2118/181819-MS

Zimmerman, R.W., Chen, G., Hadgu, T., Bodvarsson, G.S., 1993. A numerical dual-porosity model with semianalytical treatment of fracture/matrix flow. Water Resour. Res. 29, 2127–2137. https://doi.org/10.1029/93WR00749

Zuo, L., Yu, W., Wu, K., 2016. A fractional decline curve analysis model for shale gas reservoirs. Int. J. Coal Geol. 163, 140–148. https://doi.org/10.1016/J.COAL.2016.07.006

APPENDICES

A. Constant Fracture Pressure Solution

For constant pressure at the boundary of anisotropic matrix having a single-phase slightly compressible fluid, PDE, IC and BCs are defined as:

$$c_u k_x \frac{\partial^2 P}{\partial x^2} + c_u k_y \frac{\partial^2 P}{\partial y^2} + c_u k_z \frac{\partial^2 P}{\partial z^2} = (\phi \mu c_t) \frac{\partial P}{\partial t} \qquad \begin{matrix} 0 \le x \le L_x \\ 0 \le y \le L_y \\ 0 \le z \le L_z \end{matrix} \tag{A-1}$$

$$P(x, y, z, t = 0) = P_i \tag{A-2}$$

$$P \begin{bmatrix} x = 0 \ \& \ x = L_x \\ y = 0 \ \& \ y = L_y \\ z = 0 \ \& \ z = L_z \end{bmatrix} = P_f \qquad t > 0 \tag{A-3}$$

where P_i is initial pressure (M/L×T^2) and P_f is fracture pressure (M/L×T^2). To simplify original PDE given in Eq. A-1, following dimensionless parameters are used:

$$P_D = \frac{P - P_i}{P_f - P_i}, \quad x_D = \frac{x}{L_x}, \quad y_D = \frac{y}{L_y}, \quad z_D = \frac{z}{L_z}, \quad t_D = \frac{c_u k_x t}{(\phi \mu c_t) L_x^2} = \frac{\eta_x}{L_x^2} t \tag{A-4}$$

where P_D is dimensionless pressure, P_f is fracture pressure (M/L×T^2), x_D, y_D and z_D are dimensionless length in x, y and z-direction, t_D is dimensionless time, η_x is diffusivity coefficient in x-direction (L^2/T). Finally, PDE in dimensionless form becomes:

$$C_x \frac{\partial^2 P_D}{\partial {x_D}^2} + C_y \frac{\partial^2 P_D}{\partial {y_D}^2} + C_z \frac{\partial^2 P_D}{\partial {z_D}^2} = \frac{\partial P_D}{\partial t_D} \tag{A-5}$$

with coefficients of :

$$C_x = 1, \quad C_y = \frac{k_y L_x^2}{k_x L_y^2}, \quad C_z = \frac{k_z L_x^2}{k_x L_z^2} \tag{A-6}$$

IC and BCs in all directions are also written in dimensionless form, such that:

$$P_D(x_D, y_{D,} z_D, t_D) = 0 \quad @\, t_D = 0 \tag{A-7}$$

$$P_D \begin{bmatrix} x_D = 0 \ \& \ x_D = 1, t_D \\ y_D = 0 \ \& \ y_D = 1, t_D \\ z_D = 0 \ \& \ z_D = 1, t_D \end{bmatrix} = 1 \tag{A-8}$$

As seen in Eq. A-8, boundary conditions are not homogeneous. To apply separation of variable techniques, problem is converted to homogenous one by defining new dimensionless pressure as:

$$P_{DH} = \frac{P_f - P}{P_f - P_i} = 1 - P_D \tag{A-9}$$

$$PDE: \quad C_x \frac{\partial^2 P_{DH}}{\partial x_D{}^2} + C_y \frac{\partial^2 P_{DH}}{\partial y_D{}^2} + C_z \frac{\partial^2 P_{DH}}{\partial z_D{}^2} = \frac{\partial P_{DH}}{\partial t_D} \tag{A-10}$$

$$IC: \quad P_{DH}(x_D, y_D, z_D, 0) = 1 \tag{A-11}$$

$$BCs: \quad P_{DH}(boundaries, t_D) = 0 \tag{A-12}$$

According to new IC and BCs, new dimensionless pressure can be expressed as product of four functions which are function of single variable.

$$P_{DH}(x_D, y_D, z_D, t_D) = X(x_D) Y(y_D) Z(z_D) T(t_D) \tag{A-13}$$

By using Eq. A-10 leads to following equalities:

$$C_x \frac{1}{X} \frac{\partial^2 X}{\partial x_D{}^2} + C_y \frac{1}{Y} \frac{\partial^2 Y}{\partial y_D{}^2} + C_z \frac{1}{Z} \frac{\partial^2 Z}{\partial z_D{}^2} = \frac{1}{T} \frac{\partial T}{\partial t_D} = -\lambda^2 \tag{A-14}$$

$$-\alpha^2-\beta^2-\gamma^2=-\lambda^2 \tag{A-15}$$

Now, each single dependent function can be solved as eigenvalue problem by using Eq. A-14. Applying BCs in Eq. A-12 yields:

$$\frac{d^2X}{dx_D}=\frac{\alpha^2}{C_x}X \quad \Rightarrow X(x_D)=c_2\cos\left[\sqrt{\alpha^2/C_x}\,x_D\right]+c_3\sin\left[\sqrt{\alpha^2/C_x}\,x_D\right]$$
$$X(x_D)=c_3\sin\left[n\pi x_D\right], \qquad n\pi=\sqrt{\alpha^2/C_x}, \qquad n=1,2,3..... \tag{A-16}$$

$$\frac{d^2Y}{dy_D}=\frac{\beta^2}{C_y}Y \quad \Rightarrow Y(y_D)=c_4\cos\left[\sqrt{\beta^2/C_y}\,y_D\right]+c_5\sin\left[\sqrt{\beta^2/C_y}\,y_D\right]$$
$$Y(y_D)=c_5\sin\left[m\pi y_D\right], \qquad m\pi=\sqrt{\beta^2/C_y}, \qquad m=1,2,3..... \tag{A-17}$$

$$\frac{d^2Z}{dz_D}=\frac{\gamma^2}{C_z}Z \quad \Rightarrow Z(z_D)=c_6\cos\left[\sqrt{\gamma^2/C_z}\,z_D\right]+c_7\sin\left[\sqrt{\gamma^2/C_z}\,z_D\right]$$
$$Z(z_D)=c_7\sin\left[k\pi z_D\right], \qquad k\pi=\sqrt{\gamma^2/C_z}, \qquad k=1,2,3.....$$
(A-18)

Using Eq. A-13, general solution for P_{DH} can be expressed as:

$$P_{DH}(x_D,y_D,z_D,t_D)=\sum_{n=1}^{\infty}\sum_{m=1}^{\infty}\sum_{k=1}^{\infty}c_{nmk}\exp(-\lambda^2 t_D)\sin\left[n\pi x_D\right]\sin\left[m\pi x_D\right]\sin\left[k\pi x_D\right] \tag{A-19}$$

To find c_{nmk} term, initial condition and orthogonality of sin*e* function are used, and it is found as:

$$c_{nmk}=\frac{8}{\pi^3}\left(\frac{1-(-1)^n}{n}\right)\left(\frac{1-(-1)^m}{m}\right)\left(\frac{1-(-1)^k}{k}\right) \tag{A-20}$$

For any even values of n, m and k, c_{nmk} becomes zero. Therefore, they are replaced by $2n+1$, $2m+1$ and $2k+1$, respectively. Then, final homogeneous solution for anisotropic matrix is:

$$P_{DH}(x_D, y_D, z_D, t_D) = \frac{64}{\pi^3}\sum_{n=0}^{\infty}\sum_{m=0}^{\infty}\sum_{k=0}^{\infty}\frac{\exp\left\{-\left[(2n+1)^2 C_x + (2m+1)^2 C_y + (2k+1)^2 C_z\right]\pi^2 t_D\right\}}{(2n+1)(2m+1)(2k+1)}\times$$
$$\sin\left[(2n+1)\pi x_D\right]\sin\left[(2m+1)\pi x_D\right]\sin\left[(2k+1)\pi x_D\right]$$

(A-21)

From Eq. A-9,

$$P_D(x_D, y_D, z_D, t_D) = 1-\frac{64}{\pi^3}\sum_{n=0}^{\infty}\sum_{m=0}^{\infty}\sum_{k=0}^{\infty}\frac{\exp\left\{-\left[(2n+1)^2 C_x + (2m+1)^2 C_y + (2k+1)^2 C_z\right]\pi^2 t_D\right\}}{(2n+1)(2m+1)(2k+1)}\times$$
$$\sin\left[(2n+1)\pi x_D\right]\sin\left[(2m+1)\pi x_D\right]\sin\left[(2k+1)\pi x_D\right]$$

(A-22)

Using Eq. 21, time-dependent shape factor takes form of:

$$\sigma(t) = \frac{1}{\eta_m}\frac{1}{1-\overline{P_D}}\frac{\partial \overline{P_D}}{\partial t} \qquad \text{(A-23)}$$

Average dimensionless matrix pressure is calculated as:

$$\overline{P_D}(x_D, y_D, z_D, t_D) = 1-\frac{512}{\pi^6}\sum_{n=0}^{\infty}\sum_{m=0}^{\infty}\sum_{k=0}^{\infty}\frac{\exp\left\{-\left[(2n+1)^2 C_x + (2m+1)^2 C_y + (2k+1)^2 C_z\right]\pi^2 t_D\right\}}{(2n+1)^2(2m+1)^2(2k+1)^2}$$

(A-24)

Finally, time-dependent shape factor for a 3D anisotropic matrix becomes:

$$\sigma_{3D}(t) = \frac{1}{\eta_m}\frac{\eta_x}{L_x^2}\pi^2\frac{\sum_{n=0}^{\infty}\sum_{m=0}^{\infty}\sum_{k=0}^{\infty}\frac{\left[\begin{array}{l}\left[(2n+1)^2 C_x + (2m+1)^2 C_y + (2k+1)^2 C_z\right]\times \\ \exp\left\{-\left[(2n+1)^2 C_x + (2m+1)^2 C_y + (2k+1)^2 C_z\right]\pi^2 t_D\right\}\end{array}\right]}{(2n+1)^2(2m+1)^2(2k+1)^2}}{\sum_{n=0}^{\infty}\sum_{m=0}^{\infty}\sum_{k=0}^{\infty}\frac{\exp\left\{-\left[(2n+1)^2 C_x + (2m+1)^2 C_y + (2k+1)^2 C_z\right]\pi^2 t_D\right\}}{(2n+1)^2(2m+1)^2(2k+1)^2}}$$

(A-25)

For an isotropic case where $k_x = k_y = k_z = k$ and $L_x = L_y = L_z = L$, time-dependent 3D shape factor is:

$$\sigma_{3D}(t) = \frac{\pi^2}{L^2} \frac{\sum_{n=0}^{\infty}\sum_{m=0}^{\infty}\sum_{k=0}^{\infty} \frac{\left[\left[(2n+1)^2+(2m+1)^2+(2k+1)^2\right]\times\exp\left\{-\left[(2n+1)^2+(2m+1)^2+(2k+1)^2\right]\pi^2 t_D\right\}\right]}{(2n+1)^2(2m+1)^2(2k+1)^2}}{\sum_{n=0}^{\infty}\sum_{m=0}^{\infty}\sum_{k=0}^{\infty} \frac{\exp\left\{-\left[(2n+1)^2+(2m+1)^2+(2k+1)^2\right]\pi^2 t_D\right\}}{(2n+1)^2(2m+1)^2(2k+1)^2}}$$

(A-26)

Similar to time-dependent 3D shape factor, 1D and 2D versions are presented in below, respectively:

$$\sigma_{2D}(t) = \frac{\pi^2}{L^2} \frac{\sum_{n=0}^{\infty}\sum_{m=0}^{\infty} \frac{\left[\left[(2n+1)^2+(2m+1)^2\right]\times\exp\left\{-\left[(2n+1)^2+(2m+1)^2\right]\pi^2 t_D\right\}\right]}{(2n+1)^2(2m+1)^2}}{\sum_{n=0}^{\infty}\sum_{m=0}^{\infty} \frac{\exp\left\{-\left[(2n+1)^2+(2m+1)^2\right]\pi^2 t_D\right\}}{(2n+1)^2(2m+1)^2}}$$

(A-27)

$$\sigma_{1D}(t) = \frac{\pi^2}{L^2} \frac{\sum_{n=0}^{\infty}\exp\left\{-(2n+1)^2\pi^2 t_D\right\}}{\sum_{n=0}^{\infty}\frac{\exp\left\{-(2n+1)^2\pi^2 t_D\right\}}{(2n+1)^2}} \quad \text{(A-28)}$$

B. Constant Rate (Flux) Solution

For a single-phase slightly compressible fluid, diffusivity equation (partial differential equation-PDE) in anisotropic matrix medium (Cartesian coordinate system) can be written:

$$c_u k_x \frac{\partial^2 P}{\partial x^2} + c_u k_y \frac{\partial^2 P}{\partial y^2} + c_u k_z \frac{\partial^2 P}{\partial z^2} = (\phi \mu c_t) \frac{\partial P}{\partial t} \qquad \begin{array}{l} 0 \le x \le L_x \\ 0 \le y \le L_y \\ 0 \le z \le L_z \end{array} \qquad \text{(B-1)}$$

where k_x, k_y and k_z are matrix permeability in x, y and z-direction, having fracture spacing of L_x, L_y and L_z, respectively. Initial condition (IC) and constant flux (rate per unit flow area) boundary conditions (BCs) for all directions are given:

$$P(x, y, z, t = 0) = P_i \qquad \text{(B-2)}$$

$$-c_u k_x \frac{\partial P}{\partial x} = q_x \quad @\, x = L_x \qquad \text{and} \qquad -c_u k_x \frac{\partial P}{\partial x} = -q_x \quad @\, x = 0 \qquad \text{(B-3)}$$

$$-c_u k_y \frac{\partial P}{\partial y} = q_y \quad @\, y = L_y \qquad \text{and} \qquad -c_u k_y \frac{\partial P}{\partial y} = -q_y \quad @\, y = 0 \qquad \text{(B-4)}$$

$$-c_u k_z \frac{\partial P}{\partial z} = q_z \quad @\, z = L_z \qquad \text{and} \qquad -c_u k_z \frac{\partial P}{\partial z} = -q_z \quad @\, z = 0 \qquad \text{(B-5)}$$

where P_i is initial pressure (M/L×T^2), q_x, q_y and q_z are fluxes (L/T) in x, y and z-direction, respectively.

To simplify original PDE given in Eq. B-1, following dimensionless parameters are used:

$$P_D = \frac{P - P_i}{P_{f0} - P_i}, \quad x_D = \frac{x}{L_x}, \quad y_D = \frac{y}{L_y}, \quad z_D = \frac{z}{L_z}, \quad t_D = \frac{c_u k_x t}{(\phi \mu c_t) L_x^2} \qquad \text{(B-6)}$$

where P_D is dimensionless pressure, x_D, y_D and z_D are dimensionless length in x, y and z-direction, t_D is dimensionless time, P_{f0} is initial fracture pressure (M/L×T^2). Finally, PDE in dimensionless form becomes:

$$C_x \frac{\partial^2 P_D}{\partial x_D{}^2} + C_y \frac{\partial^2 P_D}{\partial y_D{}^2} + C_z \frac{\partial^2 P_D}{\partial z_D{}^2} = \frac{\partial P_D}{\partial t_D} \tag{B-7}$$

with coefficients of :

$$C_x = 1, \quad C_y = \frac{k_y L_x^2}{k_x L_y^2}, \quad C_z = \frac{k_z L_x^2}{k_x L_z^2} \tag{B-8}$$

Initial condition (IC) and boundary conditions (BCs) in all directions are also written in dimensionless form, such that:

$$P_D(x_D, y_{D,} z_D, t_D) = 0 \quad @\, t_D = 0 \tag{B-9}$$

$$\frac{\partial P_D}{\partial x_D} = f_x \quad @\, x_D = 1 \quad \& \quad \frac{\partial P_D}{\partial x_D} = -f_x \quad @\, x_D = 0, \quad f_x = \frac{q_x \mu L_x}{c_u k_x} \tag{B-10}$$

$$\frac{\partial P_D}{\partial y_D} = f_y \quad @\, y_D = 1 \quad \& \quad \frac{\partial P_D}{\partial y_D} = -f_y \quad @\, y_D = 0, \quad f_y = \frac{q_y \mu L_y}{c_u k_y} \tag{B-11}$$

$$\frac{\partial P_D}{\partial z_D} = f_z \quad @\, z_D = 1 \quad \& \quad \frac{\partial P_D}{\partial z_D} = -f_z \quad @\, z_D = 0, \quad f_z = \frac{q_z \mu L_z}{c_u k_z} \tag{B-12}$$

where f_x, f_y and f_z are associated flux terms (L^3×M/T^2) in x, y and z-direction.

As mentioned previously, 3D problem should be decomposed into six sub problems for pressure solution such that:

$$P_D(x_D, y_D, z_D, t_D) = P_{Dx}^+ + P_{Dx}^- + P_{Dy}^+ + P_{Dy}^- + P_{Dz}^+ + P_{Dz}^- \tag{B-13}$$

Solution steps are shown in below for one sub-problem as an example. Laplace transform is used to convert PDE and boundary conditions from real-time domain to Laplace domain as follows:

$$\mathcal{L}\left\{\frac{\partial^2 P_{Dx}^{+}}{\partial x_D{}^2}-\frac{1}{C_x}\frac{\partial P_{Dx}^{+}}{\partial t_D}\right\}=\frac{\partial^2 \overline{P_{Dx}^{+}}}{\partial x_D{}^2}-\frac{1}{C_x}\left(s\overline{P_{Dx}^{+}}-P_{Dx}^{+}(x_D,t_D=0)\right)=0 \tag{B-14}$$

$$\mathcal{L}\left\{\frac{\partial P_{Dx}^{+}}{\partial x_D}\right\}\Rightarrow\frac{\partial \overline{P_{Dx}^{+}}}{\partial x_D}=\frac{f_x}{s}\quad @\,x_D=1,\quad \frac{\partial \overline{P_{Dx}^{+}}}{\partial x_D}=0\quad @\,x_D=0 \tag{B-15}$$

Based on B-14, pressure solution and its derivative in Laplace domain are in the form of:

$$\overline{P_{Dx}^{+}}(x_D,s)=c_1\exp(x_D\sqrt{s/C_x})+c_2\exp(-x_D\sqrt{s/C_x}) \tag{B-16}$$

$$\frac{\partial \overline{P_{Dx}^{+}}}{\partial x_D}=c_1\sqrt{s/C_x}\exp(x_D\sqrt{s/C_x})-c_2\sqrt{s/C_x}\exp(-x_D\sqrt{s/C_x}) \tag{B-17}$$

Boundary conditions in Eq. B-15 are used to determine constants and pressure solution in Laplace domain is found as:

$$\overline{P_{Dx}^{+}}(x_D,s)=\frac{f_x}{s\sqrt{s/C_x}}\frac{\cosh(x_D\sqrt{s/C_x})}{\sinh(\sqrt{s/C_x})} \tag{B-18}$$

Similarly, mean matrix dimensionless pressure ($\overline{U_{Dx}^{+}}$) in Laplace domain can be obtained by integrating pressure solution over its boundary as shown in below:

$$\overline{U_{Dx}^{+}}(x_D,s)=\frac{\int_{x_D=0}^{x_D=1}\overline{P_{Dx}^{+}}(x_D,s)\,dx_D}{\int_{x_D=0}^{x_D=1}dx_D}=\frac{C_x f_x}{s^2} \tag{B-19}$$

To implement inversion, pressure solution is modified as:

$$\overline{P_{Dx}^{+}}(x_D,s)=\frac{f_x}{s\sqrt{s/C_x}}\frac{\exp\left[-(1-x_D)\sqrt{s/C_x})\right]+\exp\left[-(1+x_D)\sqrt{s/C_x})\right]}{1-\exp\left[-2\sqrt{s/C_x}\right]} \tag{B-20}$$

This modification allows us to use Binomial Theory such that:

$$\frac{1}{1-\exp\left[-2\sqrt{s/C_x}\right]}=\sum_{n=0}^{\infty}\exp\left[-2n\sqrt{s/C_x}\right] \qquad \text{(B-21)}$$

Then, pressure solution in Laplace domain becomes:

$$\overline{P_{Dx}^{+}}(x_D,s)=\frac{f_x}{s\sqrt{s/C_x}}\sum_{n=0}^{\infty}\exp\left[-(2n+1-x_D)\sqrt{s/C_x}\right]+\exp\left[-(2n+1+x_D)\sqrt{s/C_x}\right]$$

(B-22)

Real time solution of pressure is obtained by taking its inversion according to Carslaw and Jeager ((1959), pp.494) as in below:

$$\mathcal{L}^{-1}\left\{\overline{P_{Dx}^{+}}(x_D,s)\right\}=P_{Dx}^{+}(x_D,t_D)=f_x\left\{\begin{array}{l}\sum_{n=0}^{\infty}2\sqrt{\frac{C_x t_D}{\pi}}\left[\begin{array}{l}\exp(\frac{-(2n+1-x_D)^2}{4t_D})\\+\exp(\frac{-(2n+1+x_D)^2}{4t_D})\end{array}\right]\\-(2n+1-x_D)erfc(\frac{(2n+1-x_D)}{2\sqrt{t_D}})\\-(2n+1+x_D)erfc(\frac{(2n+1+x_D)}{2\sqrt{t_D}})\end{array}\right\}$$

(B-23)

Mean matrix dimensionless pressure is also inverted to real time domain as:

$$\mathcal{L}^{-1}\left\{\overline{U_{Dx}^{+}}(x_D,s)\right\}=U_{Dx}^{+}(x_D,t_D)=C_x f_x t_D \qquad \text{(B-24)}$$

Same steps are followed to find P_{Dx}^{-} and U_{Dx}^{-} as presented in below, respectively:

$$P_{Dx}^{-}(x_D,t_D) = f_x \left\{ \begin{array}{l} \sum_{n=0}^{\infty} 2\sqrt{\frac{C_x t_D}{\pi}} \left[\exp(\frac{-(2n+2-x_D)^2}{4t_D}) + \exp(\frac{-(2n+x_D)^2}{4t_D}) \right] \\ -\left[(2n+2-x_D) erfc(\frac{(2n+2-x_D)}{2\sqrt{t_D}}) + (2n+x_D) erfc(\frac{(2n+x_D)}{2\sqrt{t_D}}) \right] \end{array} \right\}$$

(B-25)

$$U_{Dx}^{-}(x_D,t_D) = C_x f_x t_D \qquad \text{(B-26)}$$

As it can be seen from Eq. B-24 and Eq. B-26, mean matrix pressures are same, which is another justification for solution method. Following steps mentioned above for y and z-directions allows to find final 3D pressure solution and mean matrix pressure according to formulas in below:

$$P_D(x_D,y_D,z_D,t_D) = P_{Dx}^{+} + P_{Dx}^{-} + P_{Dy}^{+} + P_{Dy}^{-} + P_{Dz}^{+} + P_{Dz}^{-} \qquad \text{(B-27)}$$

$$U_D(x_D,y_D,z_D,t_D) = U_{Dx}^{+} + U_{Dx}^{-} + U_{Dy}^{+} + U_{Dy}^{-} + U_{Dz}^{+} + U_{Dz}^{-} \qquad \text{(B-28)}$$

The final form of 3D pressure solution and mean matrix pressure for anisotropic matrix are:

$$
\begin{aligned}
P_D(x_D, y_D, z_D, t_D) = {} & f_x \left\{ \sum_{n=0}^{\infty} 2\sqrt{\frac{C_x t_D}{\pi}} \left[\begin{array}{l} \exp\left(\frac{-(2n+1-x_D)^2}{4t_D}\right) + \exp\left(\frac{-(2n+1+x_D)^2}{4t_D}\right) \\ + \exp\left(\frac{-(2n+2-x_D)^2}{4t_D}\right) + \exp\left(\frac{-(2n+x_D)^2}{4t_D}\right) \end{array} \right] \right. \\
& \left. - \left[\begin{array}{l} (2n+1-x_D) erfc\left(\frac{(2n+1-x_D)}{2\sqrt{t_D}}\right) + (2n+1+x_D) erfc\left(\frac{(2n+1+x_D)}{2\sqrt{t_D}}\right) \\ + (2n+2-x_D) erfc\left(\frac{(2n+2-x_D)}{2\sqrt{t_D}}\right) + (2n+x_D) erfc\left(\frac{(2n+x_D)}{2\sqrt{t_D}}\right) \end{array} \right] \right\} \\
& + f_y \left\{ \sum_{n=0}^{\infty} 2\sqrt{\frac{C_y t_D}{\pi}} \left[\begin{array}{l} \exp\left(\frac{-(2n+1-y_D)^2}{4t_D}\right) + \exp\left(\frac{-(2n+1+y_D)^2}{4t_D}\right) \\ + \exp\left(\frac{-(2n+2-y_D)^2}{4t_D}\right) + \exp\left(\frac{-(2n+y_D)^2}{4t_D}\right) \end{array} \right] \right. \\
& \left. - \left[\begin{array}{l} (2n+1-y_D) erfc\left(\frac{(2n+1-y_D)}{2\sqrt{t_D}}\right) + (2n+1+y_D) erfc\left(\frac{(2n+1+y_D)}{2\sqrt{t_D}}\right) \\ + (2n+2-y_D) erfc\left(\frac{(2n+2-y_D)}{2\sqrt{t_D}}\right) + (2n+y_D) erfc\left(\frac{(2n+y_D)}{2\sqrt{t_D}}\right) \end{array} \right] \right\} \\
& + f_z \left\{ \sum_{n=0}^{\infty} 2\sqrt{\frac{C_z t_D}{\pi}} \left[\begin{array}{l} \exp\left(\frac{-(2n+1-z_D)^2}{4t_D}\right) + \exp\left(\frac{-(2n+1+z_D)^2}{4t_D}\right) \\ + \exp\left(\frac{-(2n+2-z_D)^2}{4t_D}\right) + \exp\left(\frac{-(2n+z_D)^2}{4t_D}\right) \end{array} \right] \right. \\
& \left. - \left[\begin{array}{l} (2n+1-z_D) erfc\left(\frac{(2n+1-z_D)}{2\sqrt{t_D}}\right) + (2n+1+z_D) erfc\left(\frac{(2n+1+z_D)}{2\sqrt{t_D}}\right) \\ + (2n+2-z_D) erfc\left(\frac{(2n+2-z_D)}{2\sqrt{t_D}}\right) + (2n+z_D) erfc\left(\frac{(2n+z_D)}{2\sqrt{t_D}}\right) \end{array} \right] \right\}
\end{aligned}
\tag{B-29}
$$

$$
U_D(x_D, y_D, z_D, t_D) = 2(C_x f_x + C_y f_y + C_z f_z) t_D \tag{B-30}
$$

To find time-dependent shape factor, Eq. 21 is used. It can be written for x-direction as:

$$\sigma_x(t) = \frac{1}{\eta_m} \frac{1}{P_{fx} - \overline{P_{mx}}} \frac{\partial \overline{P_{mx}}}{\partial t} \tag{B-31}$$

Following definitions are needed for parameters in Eq. B-31 to calculate time-dependent shape factor:

$$P_{mx} = P_i - \Delta P_0 P_{Dx} \quad \& \quad \Delta P_0 = P_i - P_{f0} \tag{B-32}$$

$$\overline{P_{mx}}(x_D, t_D) = \frac{\int_{x_D=0}^{x_D=1} P_{mx}(x_D, t)\, dx_D}{\int_{x_D=0}^{x_D=1} dx_D} \tag{B-33}$$

$$P_{fx} = P_i - \Delta P_0 P_{Dx}(x_D = 0 \;\; OR \;\; x_D = 1, t_D) \tag{B-34}$$

By using relations above, time-dependent shape factor for x- direction can be found as:

$$\sigma_x(t) = \frac{1}{\eta_m} \frac{2C_x \left(\frac{c_u k_x}{(\phi \mu c_t) L_x^2} \right)}{\left[\left\{ \begin{array}{l} \sum_{n=0}^{\infty} 2\sqrt{\frac{C_x t_D}{\pi}} \left[\exp(\frac{-(2n)^2}{4t_D}) + 2\exp(\frac{-(2n+1)^2}{4t_D}) + \exp(\frac{-(2n+2)^2}{4t_D}) \right] \\ -\left[(2n) erfc(\frac{2n}{2\sqrt{t_D}}) + 2(2n+1) erfc(\frac{2n+1}{2\sqrt{t_D}}) + (2n+2) erfc(\frac{2n+2}{2\sqrt{t_D}}) \right] \end{array} \right\} - 2C_x t_D \right]} \tag{B-35}$$

Remember that same terms for 1D case are not cancelled to emphasize anisotropy for 2D and 3D cases. As in the case of pressure, summation should be done for all directions to calculate 3D shape factor according to:

$$\sigma_{3D}(t) = \sigma_x(t) + \sigma_y(t) + \sigma_z(t) \tag{B-36}$$

For an anisotropic matrix including fracture spacing, time-dependent 3D shape factor becomes:

$$\sigma_{3D}(t)=\frac{2}{\eta_m}\left(\frac{c_u k_x}{(\phi\mu c_t)L_x^2}\right)\left\{\begin{array}{c}\dfrac{C_x}{\left[\left\{\begin{array}{l}\sum_{n=0}^{\infty}2\sqrt{\dfrac{C_x t_D}{\pi}}\left[\exp(\dfrac{-(2n)^2}{4t_D})+2\exp(\dfrac{-(2n+1)^2}{4t_D})+\exp(\dfrac{-(2n+2)^2}{4t_D})\right]\\ -\left[(2n)erfc(\dfrac{2n}{2\sqrt{t_D}})+2(2n+1)erfc(\dfrac{2n+1}{2\sqrt{t_D}})+(2n+2)erfc(\dfrac{2n+2}{2\sqrt{t_D}})\right]\end{array}\right\}-2C_x t_D\right]}\\ +\\ \dfrac{C_y}{\left[\left\{\begin{array}{l}\sum_{n=0}^{\infty}2\sqrt{\dfrac{C_y t_D}{\pi}}\left[\exp(\dfrac{-(2n)^2}{4t_D})+2\exp(\dfrac{-(2n+1)^2}{4t_D})+\exp(\dfrac{-(2n+2)^2}{4t_D})\right]\\ -\left[(2n)erfc(\dfrac{2n}{2\sqrt{t_D}})+2(2n+1)erfc(\dfrac{2n+1}{2\sqrt{t_D}})+(2n+2)erfc(\dfrac{2n+2}{2\sqrt{t_D}})\right]\end{array}\right\}-2C_y t_D\right]}\\ +\\ \dfrac{C_z}{\left[\left\{\begin{array}{l}\sum_{n=0}^{\infty}2\sqrt{\dfrac{C_z t_D}{\pi}}\left[\exp(\dfrac{-(2n)^2}{4t_D})+2\exp(\dfrac{-(2n+1)^2}{4t_D})+\exp(\dfrac{-(2n+2)^2}{4t_D})\right]\\ -\left[(2n)erfc(\dfrac{2n}{2\sqrt{t_D}})+2(2n+1)erfc(\dfrac{2n+1}{2\sqrt{t_D}})+(2n+2)erfc(\dfrac{2n+2}{2\sqrt{t_D}})\right]\end{array}\right\}-2C_z t_D\right]}\end{array}\right\} \tag{B-37}$$

For an isotropic case where $k_x = k_y = k_z = k$, $L_x = L_y = L_z = L$ and $q_x = q_y = q_z = q_f$, time-dependent 3D shape factor becomes:

$$\sigma_{3D}(t)=\frac{6}{L^2}\frac{1}{\left[\left\{\begin{array}{l}\sum_{n=0}^{\infty}2\sqrt{\frac{t_D}{\pi}}\left[\exp(\frac{-(2n)^2}{4t_D})+2\exp(\frac{-(2n+1)^2}{4t_D})+\exp(\frac{-(2n+2)^2}{4t_D})\right]\\-\left[(2n)erfc(\frac{2n}{2\sqrt{t_D}})+2(2n+1)erfc(\frac{2n+1}{2\sqrt{t_D}})+(2n+2)erfc(\frac{2n+2}{2\sqrt{t_D}})\right]\end{array}\right\}-2t_D\right]}$$

(B-38)

Similar to time-dependent 3D shape factor, 1D and 2D versions are presented in below, respectively:

$$\sigma_{1D}(t)=\frac{2}{L^2}\frac{1}{\left[\left\{\begin{array}{l}\sum_{n=0}^{\infty}2\sqrt{\frac{t_D}{\pi}}\left[\exp(\frac{-(2n)^2}{4t_D})+2\exp(\frac{-(2n+1)^2}{4t_D})+\exp(\frac{-(2n+2)^2}{4t_D})\right]\\-\left[(2n)erfc(\frac{2n}{2\sqrt{t_D}})+2(2n+1)erfc(\frac{2n+1}{2\sqrt{t_D}})+(2n+2)erfc(\frac{2n+2}{2\sqrt{t_D}})\right]\end{array}\right\}-2t_D\right]}$$

(B-39)

$$\sigma_{2D}(t)=\frac{4}{L^2}\frac{1}{\left[\left\{\begin{array}{l}\sum_{n=0}^{\infty}2\sqrt{\frac{t_D}{\pi}}\left[\exp(\frac{-(2n)^2}{4t_D})+2\exp(\frac{-(2n+1)^2}{4t_D})+\exp(\frac{-(2n+2)^2}{4t_D})\right]\\-\left[(2n)erfc(\frac{2n}{2\sqrt{t_D}})+2(2n+1)erfc(\frac{2n+1}{2\sqrt{t_D}})+(2n+2)erfc(\frac{2n+2}{2\sqrt{t_D}})\right]\end{array}\right\}-2t_D\right]}$$

(B-40)

C. Constant Fracture Pressure Followed by Linearly Declining Fracture Pressure Solution

For constant pressure followed by linearly declining pressure at the boundary of anisotropic matrix having a single-phase slightly compressible fluid, PDE, IC and BCs are defined as:

$$c_u k_x \frac{\partial^2 P}{\partial x^2} + c_u k_y \frac{\partial^2 P}{\partial y^2} + c_u k_z \frac{\partial^2 P}{\partial z^2} = (\phi \mu c_t) \frac{\partial P}{\partial t} \qquad \begin{matrix} 0 \le x \le L_x \\ 0 \le y \le L_y \\ 0 \le z \le L_z \end{matrix} \qquad \text{(C-1)}$$

$$P(x, y, z, t = 0) = P_i \qquad \text{(C-2)}$$

$$P \begin{bmatrix} x = 0 \ \& \ x = L_x, t \\ y = 0 \ \& \ y = L_y, t \\ z = 0 \ \& \ z = L_z, t \end{bmatrix} = \begin{Bmatrix} P_f & t \le t_s \\ P_f - K(t - t_s) & t > t_s \end{Bmatrix} \qquad \text{(C-3)}$$

where, K is decline coefficient (P/T or M/L×T^3) and t_s is switching time (T) from constant fracture pressure to linear declining fracture pressure. To simplify original PDE given in Eq. C-1, following dimensionless parameters are used:

$$P_D = \frac{P - P_i}{P_f - P_i}, \quad x_D = \frac{x}{L_x}, \quad y_D = \frac{y}{L_y}, \quad z_D = \frac{z}{L_z}, \quad t_D = \frac{c_u k_x t}{(\phi \mu c_t) L_x^2} = \frac{\eta_x}{L_x^2} t \qquad \text{(C-4)}$$

where P_D is dimensionless pressure, $P_f = P_{f0}$ is initial fracture pressure (M/L×T^2), x_D, y_D and z_D are dimensionless length in x, y and z-direction, t_D is dimensionless time, η_x is diffusivity coefficient in x-direction (L^2/T). Finally, PDE in dimensionless form becomes:

$$C_x \frac{\partial^2 P_D}{\partial {x_D}^2} + C_y \frac{\partial^2 P_D}{\partial {y_D}^2} + C_z \frac{\partial^2 P_D}{\partial {z_D}^2} = \frac{\partial P_D}{\partial t_D} \qquad \text{(C-5)}$$

with coefficients of :

$$C_x = 1, \quad C_y = \frac{k_y L_x^2}{k_x L_y^2}, \quad C_z = \frac{k_z L_x^2}{k_x L_z^2} \tag{C-6}$$

IC and BCs in all directions are also written in dimensionless form, such that:

$$P_D(x_D, y_{D,} z_D, t_D) = 0 \quad @\, t_D = 0 \tag{C-7}$$

$$P_D \begin{bmatrix} x_D = 0 \ \& \ x_D = 1, t_D \\ y_D = 0 \ \& \ y_D = 1, t_D \\ z_D = 0 \ \& \ z_D = 1, t_D \end{bmatrix} = \begin{Bmatrix} 1 & t_D \le t_{Ds} \\ 1 + \dfrac{K(t_D - t_{Ds})}{\Delta P_0 \dfrac{\eta_x}{L_x^2}} & t_D > t_{Ds} \end{Bmatrix} \tag{C-8}$$

As seen from BCs above, this problem can be treated as superimposed version of two distinct problems. In this respect, two new PDEs are constructed based on Eq. C-9 in below and Eq. C-5. Also, new dimensionless pressure definition shown in Eq. C-10 is used to find IC and BCs of sub-problems.

$$P_D = 1 - (P_{DH} + P_{DT}) \tag{C-9}$$

$$P_{DH} = P_{DT} = \frac{P_f - P}{P_f - P_i} \tag{C-10}$$

where P_{DH} is dimensionless pressure for homogeneous problem while P_{DT} is dimensionless pressure for time-dependent problem. Their final versions including IC and BCs becomes:

$$PDE: \quad C_x \frac{\partial^2 P_{DH}}{\partial {x_D}^2} + C_y \frac{\partial^2 P_{DH}}{\partial {y_D}^2} + C_z \frac{\partial^2 P_{DH}}{\partial {z_D}^2} = \frac{\partial P_{DH}}{\partial t_D} \tag{C-11}$$

$$IC: \quad P_{DH}(x_D, y_D, z_D, 0) = 1 \tag{C-12}$$

$$BCs: \quad P_{DH}(boundaries, t_D) = 0 \tag{C-13}$$

$$PDE: \quad C_x \frac{\partial^2 P_{DT}}{\partial x_D{}^2} + C_y \frac{\partial^2 P_{DT}}{\partial y_D{}^2} + C_z \frac{\partial^2 P_{DT}}{\partial z_D{}^2} = \frac{\partial P_{DT}}{\partial t_D} \tag{C-14}$$

$$IC: \quad P_{DT}(x_D, y_D, z_D, 0) = 0 \tag{C-15}$$

$$BCs: \quad \left\{ \begin{array}{ll} P_{DT}(boundaries, t_D) = 0 & t_D \le t_{Ds} \\ P_{DT}(boundaries, t_D) = -\dfrac{K(t_D - t_{Ds})}{\Delta P_0 \dfrac{\eta_x}{L_x^2}} & t_D > t_{Ds} \end{array} \right\} \tag{C-16}$$

For homogeneous problem, solution is already obtained for constant fracture pressure case as:

$$P_{DH}(x_D, y_D, z_D, t_D) = \frac{64}{\pi^3} \sum_{n=0}^{\infty} \sum_{m=0}^{\infty} \sum_{k=0}^{\infty} \frac{\exp\left\{-\left[(2n+1)^2 C_x + (2m+1)^2 C_y + (2k+1)^2 C_z\right]\pi^2 t_D\right\}}{(2n+1)(2m+1)(2k+1)} \times$$
$$\sin\left[(2n+1)\pi x_D\right] \sin\left[(2m+1)\pi x_D\right] \sin\left[(2k+1)\pi x_D\right] \tag{C-17}$$

To solve PDE with time-dependent boundary conditions, Duhamel's theorem is implemented. Solution strategy is forming an auxiliary problem where initial condition is zero while boundary conditions are unity. In this respect, auxiliary problem becomes:

$$PDE: \quad C_x \frac{\partial^2 P_{DA}}{\partial x_D{}^2} + C_y \frac{\partial^2 P_{DA}}{\partial y_D{}^2} + C_z \frac{\partial^2 P_{DA}}{\partial z_D{}^2} = \frac{\partial P_{DA}}{\partial t_D} \tag{C-18}$$

$$IC: \quad P_{DA}(x_D, y_D, z_D, 0) = 0 \tag{C-19}$$

$$BCs: \quad P_{DA}(boundaries, t_D) = 1 \tag{C-20}$$

where P_{DA} is dimensionless pressure for auxiliary problem. As seen in Eq. C-11, Eq. C-12 and Eq. C-13, auxiliary problem can be formed from P_{DH} by satisfying all conditions mentioned above such that :

$$P_{DA} = 1 - P_{DH} \tag{C-21}$$

Final form of the P_{DA} is:

$$P_{DA}(x_D, y_D, z_D, t_D) = 1 - \frac{64}{\pi^3} \sum_{n=0}^{\infty} \sum_{m=0}^{\infty} \sum_{k=0}^{\infty} \frac{\exp\left\{-\left[(2n+1)^2 C_x + (2m+1)^2 C_y + (2k+1)^2 C_z\right]\pi^2 t_D\right\}}{(2n+1)(2m+1)(2k+1)} \times$$
$$\sin\left[(2n+1)\pi x_D\right] \sin\left[(2m+1)\pi x_D\right] \sin\left[(2k+1)\pi x_D\right]$$

(C-22)

P_{DT} is calculated by using Duhamel's superposition integral (Hahn and Ozisik (2012)) as:

$$P_{DT}(x_D, y_D, z_D, t_D) = \int_{\tau=0}^{t_D} f(\tau) \frac{\partial P_{DA}(x_D, y_D, z_D, t_D - \tau)}{\partial t_D} d\tau \qquad \text{(C-23)}$$

where $f(\tau)$ is time-dependent boundary condition, which is:

$$\begin{cases} f(\tau) = 0 & \tau \le t_{Ds} \\ f(\tau) = -\dfrac{K(\tau - t_{Ds})}{\Delta P_0 \dfrac{\eta_x}{L_x^2}} & \tau > t_{Ds} \end{cases} \qquad \text{(C-24)}$$

Based on BCs above, P_{DT} becomes:

$$P_{DT}(x_D, y_D, z_D, t_D) = \int_{t_{Ds}}^{t_D} -\frac{K(\tau - t_{Ds})}{\Delta P_0 \dfrac{\eta_x}{L_x^2}} \frac{\partial P_{DA}(x_D, y_D, z_D, t_D - \tau)}{\partial t_D} d\tau \qquad \text{(C-25)}$$

After tedious integration, P_{DT} for anisotropic 3D matrix is:

$$P_{DT}(x_D, y_D, z_D, t_D) = \left\{ \begin{array}{l} -\dfrac{K}{\Delta P_0 \dfrac{\eta_x}{L_x^2}} \dfrac{64}{\pi^3} \sum_{n=0}^{\infty}\sum_{m=0}^{\infty}\sum_{k=0}^{\infty} \dfrac{(t_D - t_{Ds})}{B} \times \\ \sin\left[(2n+1)\pi x_D\right] \sin\left[(2m+1)\pi x_D\right] \sin\left[(2k+1)\pi x_D\right] \end{array} \right\}$$

$$+$$

$$\left\{ \begin{array}{l} -\dfrac{K}{\Delta P_0 \dfrac{\eta_x}{L_x^2}} \dfrac{64}{\pi^3} \sum_{n=0}^{\infty}\sum_{m=0}^{\infty}\sum_{k=0}^{\infty} \dfrac{\exp\{-A(t_D - t_{Ds})\} - 1}{AB} \times \\ \sin\left[(2n+1)\pi x_D\right] \sin\left[(2m+1)\pi x_D\right] \sin\left[(2k+1)\pi x_D\right] \end{array} \right\}$$

(C-26)

where,

$$A = \left[(2n+1)^2 C_x + (2m+1)^2 C_y + (2k+1)^2 C_z\right]\pi^2 \qquad \text{(C-27)}$$

$$B = (2n+1)(2m+1)(2k+1) \qquad \text{(C-28)}$$

Further simplification can be done by using following relation:

$$\sum_{p=0}^{\infty} \frac{\sin\left[(2p+1)\theta\right]}{(2p+1)} = \frac{\pi}{4}, \qquad 0 < \theta < \pi \qquad \text{(C-29)}$$

After simplification, P_{DT} for anisotropic 3D matrix becomes:

$$P_{DT}(x_D, y_D, z_D, t_D) = -\frac{K}{\Delta P_0 \dfrac{\eta_x}{L_x^2}}(t_D - t_{Ds}) - \frac{K}{\Delta P_0 \dfrac{\eta_x}{L_x^2}} \frac{64}{\pi^3} \sum_{n=0}^{\infty}\sum_{m=0}^{\infty}\sum_{k=0}^{\infty} \frac{\exp\{-A(t_D - t_{Ds})\} - 1}{AB} \times$$
$$\sin\left[(2n+1)\pi x_D\right] \sin\left[(2m+1)\pi x_D\right] \sin\left[(2k+1)\pi x_D\right]$$

(C-30)

Final dimensionless pressure solution for the problem based on Eq. C-9 is:

$$P_D(x_D, y_D, z_D, t_D) = 1 - \left(\frac{64}{\pi^3} \sum_{n=0}^{\infty} \sum_{m=0}^{\infty} \sum_{k=0}^{\infty} \frac{\exp\left\{ -\left[(2n+1)^2 C_x + (2m+1)^2 C_y + (2k+1)^2 C_z \right] \pi^2 t_D \right\}}{(2n+1)(2m+1)(2k+1)} \times \sin\left[(2n+1)\pi x_D\right] \sin\left[(2m+1)\pi x_D\right] \sin\left[(2k+1)\pi x_D\right] \right)$$

$$+ \left(\frac{K}{\Delta P_0 \frac{\eta_x}{L_x^2}} (t_D - t_{Ds}) \right)$$

$$+ \left(\frac{K}{\Delta P_0 \frac{\eta_x}{L_x^2}} \frac{64}{\pi^3} \sum_{n=0}^{\infty} \sum_{m=0}^{\infty} \sum_{k=0}^{\infty} \frac{\exp\left\{ -\left[(2n+1)^2 C_x + (2m+1)^2 C_y + (2k+1)^2 C_z \right] \pi^2 (t_D - t_{Ds}) \right\} - 1}{\left[(2n+1)^2 C_x + (2m+1)^2 C_y + (2k+1)^2 C_z \right] \pi^2 (2n+1)(2m+1)(2k+1)} \times \sin\left[(2n+1)\pi x_D\right] \sin\left[(2m+1)\pi x_D\right] \sin\left[(2k+1)\pi x_D\right] \right)$$

(C-31)

Using Eq. 21, time-dependent shape factor takes form of:

$$\sigma(t) = \frac{1}{\eta_m} \frac{1}{1 - \overline{P_D} + \frac{K}{\Delta P_0}(t - t_s)} \frac{\partial \overline{P_D}}{\partial t} \qquad \text{(C-32)}$$

Average dimensionless matrix pressure for considered problem is calculated as:

$$\overline{P_D}(x_D, y_D, z_D, t_D) = 1 - \left(\frac{512}{\pi^6} \sum_{n=0}^{\infty} \sum_{m=0}^{\infty} \sum_{k=0}^{\infty} \frac{\exp\left\{ -\left[(2n+1)^2 C_x + (2m+1)^2 C_y + (2k+1)^2 C_z \right] \pi^2 t_D \right\}}{(2n+1)^2 (2m+1)^2 (2k+1)^2} \right)$$

$$+ \left(\frac{K}{\Delta P_0 \frac{\eta_x}{L_x^2}} (t_D - t_{Ds}) \right)$$

$$+ \left(\frac{K}{\Delta P_0 \frac{\eta_x}{L_x^2}} \frac{512}{\pi^6} \sum_{n=0}^{\infty} \sum_{m=0}^{\infty} \sum_{k=0}^{\infty} \frac{\exp\left\{ -\left[(2n+1)^2 C_x + (2m+1)^2 C_y + (2k+1)^2 C_z \right] \pi^2 (t_D - t_{Ds}) \right\} - 1}{\left[(2n+1)^2 C_x + (2m+1)^2 C_y + (2k+1)^2 C_z \right] \pi^2 (2n+1)^2 (2m+1)^2 (2k+1)^2} \right)$$

(C-33)

Finally, time-dependent shape factor for a 3D anisotropic matrix becomes:

$$\sigma_{3D}(t)=\frac{1}{\eta_m}\frac{\eta_x}{L_x^2}\pi^2\frac{\sum_{n=0}^{\infty}\sum_{m=0}^{\infty}\sum_{k=0}^{\infty}\frac{\left[\begin{array}{l}\left[(2n+1)^2C_x+(2m+1)^2C_y+(2k+1)^2C_z\right]\frac{\eta_x}{L_x^2}\pi^2\times\\ \exp\left\{-\left[(2n+1)^2C_x+(2m+1)^2C_y+(2k+1)^2C_z\right]\pi^2t_D\right\}\\ -\frac{K}{\Delta P_0}(\exp\left\{-\left[(2n+1)^2C_x+(2m+1)^2C_y+(2k+1)^2C_z\right]\pi^2(t_D-t_{Ds})\right\}-1)\end{array}\right]}{(2n+1)^2(2m+1)^2(2k+1)^2}}{\sum_{n=0}^{\infty}\sum_{m=0}^{\infty}\sum_{k=0}^{\infty}\frac{\left[\begin{array}{l}\left[(2n+1)^2C_x+(2m+1)^2C_y+(2k+1)^2C_z\right]\frac{\eta_x}{L_x^2}\pi^2\times\\ \exp\left\{-\left[(2n+1)^2C_x+(2m+1)^2C_y+(2k+1)^2C_z\right]\pi^2t_D\right\}\\ -\frac{K}{\Delta P_0}(\exp\left\{-\left[(2n+1)^2C_x+(2m+1)^2C_y+(2k+1)^2C_z\right]\pi^2(t_D-t_{Ds})\right\}-1)\end{array}\right]}{\left[(2n+1)^2C_x+(2m+1)^2C_y+(2k+1)^2C_z\right](2n+1)^2(2m+1)^2(2k+1)^2}}$$

(C-34)

For an isotropic case where $k_x = k_y = k_z = k$, $L_x = L_y = L_z = L$, time-dependent 3D shape factor is:

$$\sigma_{3D}(t)=\frac{\pi^2}{L^2}\frac{\sum_{n=0}^{\infty}\sum_{m=0}^{\infty}\sum_{k=0}^{\infty}\frac{\left[\begin{array}{l}\left[(2n+1)^2+(2m+1)^2+(2k+1)^2\right]\pi^2\times\exp\left\{-\left[(2n+1)^2+(2m+1)^2+(2k+1)^2\right]\pi^2t_D\right\}\\ -\frac{K}{\Delta P_0}\frac{L^2}{\eta_m}(\exp\left\{-\left[(2n+1)^2+(2m+1)^2+(2k+1)^2\right]\pi^2(t_D-t_{Ds})\right\}-1)\end{array}\right]}{(2n+1)^2(2m+1)^2(2k+1)^2}}{\sum_{n=0}^{\infty}\sum_{m=0}^{\infty}\sum_{k=0}^{\infty}\frac{\left[\begin{array}{l}\left[(2n+1)^2+(2m+1)^2+(2k+1)^2\right]\pi^2\times\exp\left\{-\left[(2n+1)^2+(2m+1)^2+(2k+1)^2\right]\pi^2t_D\right\}\\ -\frac{K}{\Delta P_0}\frac{L^2}{\eta_m}(\exp\left\{-\left[(2n+1)^2+(2m+1)^2+(2k+1)^2\right]\pi^2(t_D-t_{Ds})\right\}-1)\end{array}\right]}{\left[(2n+1)^2+(2m+1)^2+(2k+1)^2\right](2n+1)^2(2m+1)^2(2k+1)^2}}$$

(C-35)

Similar to time-dependent 3D shape factor, 1D and 2D versions are presented in below, respectively:

$$\sigma_{2D}(t)=\frac{\pi^2}{L^2}\frac{\sum_{n=0}^{\infty}\sum_{m=0}^{\infty}\frac{\left[\begin{array}{l}\left[(2n+1)^2+(2m+1)^2\right]\pi^2\times\exp\left\{-\left[(2n+1)^2+(2m+1)^2\right]\pi^2 t_D\right\}\\ -\frac{K}{\Delta P_0}\frac{L^2}{\eta_m}(\exp\left\{-\left[(2n+1)^2+(2m+1)^2\right]\pi^2(t_D-t_{Ds})\right\}-1)\end{array}\right]}{(2n+1)^2(2m+1)^2}}{\sum_{n=0}^{\infty}\sum_{m=0}^{\infty}\frac{\left[\begin{array}{l}\left[(2n+1)^2+(2m+1)^2\right]\pi^2\times\exp\left\{-\left[(2n+1)^2+(2m+1)^2\right]\pi^2 t_D\right\}\\ -\frac{K}{\Delta P_0}\frac{L^2}{\eta_m}(\exp\left\{-\left[(2n+1)^2+(2m+1)^2\right]\pi^2(t_D-t_{Ds})\right\}-1)\end{array}\right]}{\left[(2n+1)^2+(2m+1)^2\right](2n+1)^2(2m+1)^2}} \tag{C-36}$$

$$\sigma_{1D}(t)=\frac{\pi^2}{L^2}\frac{\sum_{n=0}^{\infty}\frac{\left[\begin{array}{l}(2n+1)^2\pi^2\times\exp\left\{-(2n+1)^2\pi^2 t_D\right\}\\ -\frac{K}{\Delta P_0}\frac{L^2}{\eta_m}(\exp\left\{-(2n+1)^2\pi^2(t_D-t_{Ds})\right\}-1)\end{array}\right]}{(2n+1)^2}}{\sum_{n=0}^{\infty}\frac{\left[\begin{array}{l}(2n+1)^2\pi^2\times\exp\left\{-(2n+1)^2\pi^2 t_D\right\}\\ -\frac{K}{\Delta P_0}\frac{L^2}{\eta_m}(\exp\left\{-(2n+1)^2\pi^2(t_D-t_{Ds})\right\}-1)\end{array}\right]}{(2n+1)^4}} \tag{C-37}$$

D. Publication and Award

Journal of Petroleum Science and Engineering 200 (2021) 108261

Contents lists available at ScienceDirect

Journal of Petroleum Science and Engineering

journal homepage: http://www.elsevier.com/locate/petrol

Transient shape factors for dual-porosity simulation of tight rocks

Ufuk Kilicaslan *, Serhat Akin

Department of Petroleum & Natural Gas Engineering, Middle East Technical University, Ankara, Turkey

ARTICLE INFO

Keywords:
Matrix-fracture transfer function
Tight reservoir
Unsteady-state flow

ABSTRACT

The shape-factor concept provides an elegant and powerful upscaling method for fractured reservoir simulation. Many different shape-factors, among which the well-known Warren and Root, and Kazemi shape-factors have been proposed in the past. Since different shape-factors can lead to totally different reservoir behavior, selection of the appropriate shape-factor value is critical for accurate fractured reservoir modeling. Constant shape factor is commonly used for simulation of fractured reservoirs by assuming that pressure transient reaches to center of the matrix block within very small time. On the contrary, tight rocks exhibit longer duration of unsteady-state flow such that matrix – fracture transfer is not constant, but rather varies with time until reaching to a constant value. In this regard, dual-porosity simulation of tight rocks using constant shape factor does not capture actual physics of matrix to fracture flow and yields inaccurate performance prediction. In this study, analytical solutions of pressure diffusion and corresponding shape factors are presented for various matrix shapes. The results are compared to those obtained with simple empirical functions. Proposed functions significantly improve accuracy over existing approaches in the prediction of both mean matrix pressure and transfer function. Results of fine grid single-porosity model are compared with two different dual porosity models, one with constant shape factor and one with time dependent shape factor, to verify proposed approach.

Certificate of Participation

The Society of Petroleum Engineers (SPE) awards to

Ufuk Kilicaslan

Middle East Technical University Ankara

presented as a contestant in the PhD Division of the
2021 SPE Europe
Regional Student Paper Contest
Virtual ▪ ZOOM
11 May 2021

Tom Blasingame
SPE President

Mark Rubin
SPE CEO & Executive VP

Society of Petroleum Engineers

CURRICULUM VITAE

PERSONAL INFORMATION

Surname, Name: Kılıçaslan, Ufuk
Nationality: Turkish (TC)
Date and Place of Birth:

EDUCATION

Degree	Institution	Year of Graduation
MS	Texas A&M University Petroleum Engineering	2013
BS	METU Petroleum and Natural Gas Engineering	2010
High School	Hasanoğlan Fatih High School, Ankara	2005

WORK EXPERIENCE

Year	Place	Enrollment
2020-Present	Turkish Petroleum Corporation (TPAO)	Senior Reservoir Engineer
2014-2020	Turkish Petroleum Corporation (TPAO)	Reservoir Engineer
2010-2011	Turkish Petroleum International Company (TPIC)	Field Engineer

FOREIGN LANGUAGES

Advanced English, Basic Italian

PUBLICATIONS

1. Kilicaslan U., Akin S. "Transient shape factors for dual-porosity simulation of tight rocks", Journal of Petroleum Science and Engineering, Volume 200, 108261 (May 2021)